INVESTIGATION OF LAYERED-SPACED AND OBLIQUE MILD STEEL
TARGETS AGAINST 7.62 mm AP PROJECTILE

A THESIS SUBMITTED TO
THE GRADUATE SCHOOL OF NATURAL AND APPLIED SCIENCES
OF
MIDDLE EAST TECHNICAL UNIVERSITY

BY

MUHAMMED ÇAKIR

IN PARTIAL FULFILLMENT OF THE REQUIREMENTS
FOR
THE DEGREE OF MASTER OF SCIENCE
IN
MECHANICAL ENGINEERING

SEPTEMBER 2017

Approval of the thesis:

INVESTIGATION OF LAYERED-SPACED AND OBLIQUE MILD STEEL TARGETS AGAINST 7.62 mm AP PROJECTILE

submitted by **MUHAMMED ÇAKIR** in partial fulfillment of the requirements for the degree of **Master of Science in Mechanical Engineering Department, Middle East Technical University** by,

Prof. Dr. Gülbin Dural Ünver   _____
Dean, Graduate School of **Natural and Applied Sciences**

Prof. Dr. Tuna Balkan   _____
Head of Department, **Mechanical Engineering**

Prof. Dr. Raif Orhan Yıldırım   _____
Supervisor, **Mechanical Engineering Dept., METU**

Examining Committee Members:

Prof. Dr. Metin Akkök
Mechanical Engineering Dept., METU   _____

Prof. Dr. R. Orhan Yıldırım
Mechanical Engineering Dept., METU   _____

Prof. Dr. Mustafa İlhan Gökler
Mechanical Engineering Dept., METU   _____

Assoc. Prof. Dr. Ergin Tönük
Mechanical Engineering Dept., METU   _____

Prof. Dr. Ömer Anlağan
Mechanical Engineering Dept., Bilkent University   _____

Date: 15.09.2017

I hereby declare that all information in this document has been obtained and presented in accordance with academic rules and ethical conduct. I also declare that, as required by these rules and conduct, I have fully cited and referenced all material and results that are not original to this work.

Name, Last name   : Muhammed Çakır

Signature   :

ABSTRACT

INVESTIGATION OF LAYERED-SPACED AND OBLIQUE MILD STEEL TARGETS AGAINST 7.62 mm AP PROJECTILE

Çakır, Muhammed

M.Sc., Department of Mechanical Engineering

Supervisor: Prof. Dr. R. Orhan Yıldırım

September 2017, 164 pages

Ballistic resistance of steel targets is important due to its common application to the safety of personnel, shelters for arms and military vehicles. Protective systems should provide a safer condition against possible threats by reducing the weight and the volume they occupy. This causes the total weight of the armor to decrease and increases the mobility of armored vehicle. This study concerns behavior of metallic plates that are spaced and obliquely arranged in order to increase ballistic resistance against projectile penetration. Investigations are made for target configurations having various areal densities. The scope of the work also includes different orientation of single and multiple layered mild steel plates. The main effort is to seek for a better alternative layered-armor structure which provides higher protection by reducing the total weight of armor structure. The impact tests are simulated using ABAQUS/Explicit finite element software. Numerical and experimental studies revealed that it is possible to reduce the armor weight by 48% to defeat 7.62 mm AP projectile utilizing the proper layering.

Keywords: Spaced Armor Plates, 7.62mm AP, Bullet Impact, Mild Steel

ÖZ

KATMANLI-ARALIKLI VE EĞİK DÜŞÜK KARBONLU ÇELİK HEDEFLERİN 7.62 mm AP MERMİYE KARŞI İNCELENMESİ

Çakır, Muhammed

Yüksek Lisans, Makina Mühendisliği Bölümü

Tez Yöneticisi: Prof. Dr. R. Orhan Yıldırım

Eylül 2017, 164 sayfa

Çelik hedeflerin balistik dirençleri personel, mühimmat sığınakları ve askeri araçlardaki yaygın uygulamalarından dolayı önemlidir. Koruyucu sistemler ağırlıklarını ve kapladıkları hacimlerini düşürerek muhtemel tehditlere karşı daha güvenli bir durum sağlamalıdır. Bu durum zırhın toplam ağırlığını azaltması nedeniyle zırhlı yapının hareket kabiliyetinde artışa neden olacaktır. Bu çalışma, atılan cisimlerin delmesine karşı balistik direnci artırmak için aralıklı ve açılı yerleştirilmiş metal plakaların balistik davranışını incelemektedir. Araştırmalar farklı alan yoğunluklarına sahip hedef düzenlemeleri için yapılmıştır. Çalışmanın kapsamı ayrıca tek ve çok katmanlı düşük karbonlu çelik plakaların farklı yönlendirmelerini içermektedir. Temel amaç, zırh yapısının ağırlığını düşürerek daha yüksek koruma sağlayan, daha iyi bir alternatif katmanlı zırh yapısı araştırmaktır. Çarpışma testleri ABAQUS/Explicit sonlu elemanlar yazılımı ile benzetimleri yapılmıştır. Sayısal ve deneysel sonuçlar 7.62 mm AP mermiyi yenebilmek için gerekli zırh ağırlığının uygun katmanlama ile %48 azaltılabildiğini göstermiştir.

Anahtar Kelimeler: Aralıklı Zırh Plakaları, 7.62 mm AP, Mermi Çarpışması, Düşük Karbonlu Çelik Zırh Plakası

To my family…

ACKNOWLEDGMENT

TABLE OF CONTENTS

LIST OF FIGURES

LIST OF TABLES

LIST OF SYMBOLS

$\bar{\varepsilon}_f$	Equivalent fracture strain
$\bar{\varepsilon}_{pl}$	Equivalent plastic strain
$\dot{\varepsilon}^*$	Dimensionless plastic strain rate
A_1	Cross-sectional area of the hole
A_2	Cavity diameter
B_0	Dimensionless constant
$C_{0,1\ldots5}$	Material constants
C_e	Elastic stress wave speed
C_p	Plastic wave speed
$D_{1,2\ldots5}$	Damage parameters
D_2	Cylindrical cavity diameter
E_{fn}	Loss of projectile kinetic energy
F_p	Membrane stretching force
F_s	Shear force
L_1	Deformed length
L_f	Final length
M_{p0}	Plastic hinge moment around projectile
M_{pz}	Travelling plastic hinge moment
T^*	Homologous temperature
T_m	Melting temperature
T_r	Room temperature
V_2	Velocity in the second stage
V_{50}	50% Ballistic limit velocity
V_{bl}	Ballistic limit velocity
V_f	Projectile exit velocity

V_p	Common velocity
V_r	Residual velocity
V_x	Critical projectile velocity for plug ejection
W_b	Bending work
W_d	Dynamic work
W_n	Total work spent to n number of layers
W_p	Work spent to plastic deformation
k_1	Nose geometry factor
m_e	Ejected plug mass
m_p	Projectile mass
$\dot{\gamma}$	Shear strain rate
$\dot{\varepsilon}$	Strain rate
σ_h	Hydrostatic stress
$\sigma_{I,II,III}$	Principal Stresses
σ_c	Ultimate compressive stress
σ_{eq}	Equivalent stress
σ_r	Radial stress
σ_s	Pressure required to open a hole
σ_u	Ultimate tensile strength
σ_y	Yield strength
σ_θ	Tangential stress
τ_q	Dynamic peripheral shear stress
d_p	Projectile diameter
E_c	Minimum energy required for perforation of a target
h	Reduced section thickness
h_0	Initial target thickness
$\emptyset$	Nose angle
A	Johnson-Cook material parameter
B	Johnson-Cook material parameter

C	Johnson-Cook material parameter
D	Cylindrical cavity diameter
E	Modulus of elasticity (Young's Modulus)
F	Resultant force acting on the projectile
I	Moment of Inertia
N	Nose geometry function of the projectile
R	Projectile radius
S	Change in length
T	Temperature
V	Projectile Initial Velocity
V	Projectile Velocity
X	Undeformed length
a	Shattering ratio
$f(\frac{\sigma_h}{\bar{\sigma}})$	Stress triaxiality ratio
l	Target span (Lateral dimension of the plate)
m	Projectile mass
m	Termal softening exponent
m'	Mass of ejected plug material
n	Hardening exponent
n	Strain hardening parameter
p	Projectile mass ratio
q	Ratio of plug mass to projectile mass
t	Target thickness
x	Distance projectile travelled
z	Plastic hinge distance
α	Projectile nose apex angle
β	Angle of target obliquity (NATO Angle)
γ	Engineering shear strain
δ	Change in the angle of obliquity

ε	Engineering strain
θ	Plate bent angle
κ	Material parameter
μ	Coefficient of friction
τ	Shear stress
φ	Projectile nose type parameter
χ	Plate thickness to projectile diameter ratio

Subscripts

t	Target
p	Projectile
0	Initial, reference
n	Number of layer
eq	Equivalent
cr	Critical

Superscript

f	Fracture

LIST OF ABBREVIATIONS

AEP	Allied Engineering Publication
AISI	American Iron and Steel Institute
ALE	Arbitrary Lagrangian Eulerian
AP	Armor Piercing
APFSDS-T	Armor Piercing Fin Stabilized Discarding Sabot Tracer
API	Armor Piercing Incendiary
AP-T	Armor Piercing Tracer
ASTM	American Society for Testing Materials
BCC	Body Centered Cubic
BLV	Ballistic Limit Velocity
BRL	Ballistic Research Laboratory
BW	Bao-Wierzbicki
CE	Chemical energy
CL	Cockcroft-Latham
CRH	Caliber Radius Head
DIN	German Institute for Standardization
EFP	Explosively Formed Projectile
EOS	Equation of State
FCC	Face Centered Cubic
FSP	Fragment Simulating Penetrators
HCP	Hexagonal Closed Package
HRC	Hardness Rockwell C Scale
IED	Improvised Explosive Device
JC	Johnson-Cook
KE	Kinetic Energy
KEP	Kinetic Energy Projectile

NATO	North Atlantic Treaty Organization
NSA	NATO Standardizations Agency
RHA	Rolled Homogeneous Armor
SC	Shaped Charges
SFAE	Solid Fuel-Air Explosives
SHPB	Split Hopkinson Pressure Bar
SPH	Smoothed Particle Hydrodynamics
STANAG	Standardization Agreement
TBX	Thermobaric Explosives
V_{50}	50% Ballistic Limit Velocity
V_{BL}	Ballistic Limit Velocity
VoD	Velocity of Detonation
WC	Tungsten Carbide
WWII	World War Two
ZA	Zerilli-Armstrong

CHAPTER 1

INTRODUCTION

Defeating armor systems with various threat types launched by an auxiliary mechanism has been an interest by researchers for a long time. As weapon systems evolve, defense systems have been developed against these threats, as well. The main goal of defense systems is to protect personnel, structures, vehicles etc. against upcoming threats while not limiting the operational and functional abilities of protected stuff.

Mobility of military vehicles is very crucial for combat effectiveness at battles. Maneuvering capability is reduced by increasing the weight of protected structure. It effects fuel consumption, distance of navigation and ability to escape from threat factors. For this motivation, some researchers focus on weight optimization of ballistic targets [1]. Improvements on target systems have become an area of interest to succeed this aim. Light-weight protective armor system is needed for efficient operation of combat vehicles. Other properties expected from an armor system are ease of manufacturing, recycling, assembling on site and ease of maintenance when needed. Thus, metallic armors, favorably made of steel have become the most widely produced armor systems [2]. Steel has good machinability and weldability properties as well as its cheaper production cost comparing to other common metals. That makes steels to be the most widely used armor material. However, high areal density of steel makes it still questionable, and also directs researchers to develop novel armor types. The idea of using other metals as armor material brings out another field of study. Commonly used armor materials other

than steel are aluminum and titanium. Having low areal densities make them ideal materials for construction of protective structures.

Defeating a target by a threat can be possible thermally or mechanically, or a combination of these two. Defeating a target structure by means mechanical forcing can be classified into two categories; firstly, penetrating a projectile into the target until full perforation occurs, secondly using destructive effect of air or underwater blast loading.

One of the most common threat types is projectile impact of a target. Impact velocities of projectiles are classified by Goldsmith [3]. According to his work, ranges of impact regimes are;

- Sub-ordnance level $V_0 < 500$ m/s
- Ordnance level $500 < V_0 < 1500$ m/s
- Ultra-ordnance level $1500 < V_0 < 3000$ m/s
- Hypervelocity level $V_0 > 3000$ m/s

Stress waves induced by high speed contact cause the material to exceed its elastic limit and generate elastic and plastic deformations in the target. These deformations occur at high strain rates.

Another example of short duration loading can be a blast load. Airblast produced by commercially available explosives create velocities of detonation (VoD) as high as 2000-8200 m/s [4]. This range of velocity is used for producing explosively formed projectiles (EFP) as a threat type which is used as modern warfare weapons.

1.1. Impact Loading of Materials

A continuum body can be either loaded statically or dynamically. If a body is in equilibrium under different loads such as surface traction, body forces and moment loads etc. is said to be under statically loaded. Vector summations of these loadings

are the resultant force and moment acting on the body. Resultant force is constant over time in static loading cases.

Deformations at impact of two bodies occur rather in a very short period. In such cases, loads acting on a body can be described as an impact or dynamic or transient loading. Dynamic loading is time dependent and the rate of change of load is high. Therefore the internal stresses are not transmitted immediately between two distinct points of loaded continua [5]. That causes non-uniform load and stress distribution in the body. If the severity of the applied load is high it can cause stresses higher than the yield strength of the material. In such a case, both elastic and plastic stress waves are generated and these waves propagate at different speeds.

1.2. Ballistic Limit Velocity/Thickness

Ballistic limit velocity (BLV or V_{BL}) is the minimum speed of a given projectile that completely pierces an appropriate target. So, the ballistic limit velocity definition is unique for an appropriate projectile struck against an appropriate thick target having particular material properties. Moreover, there are different ballistic limit definitions in the literature as illustrated in Figure 1. These definitions may vary with respect to the protected medium. However, there is a probability of the piercing of targets especially near ballistic limit velocities. Thus, experimental ballistic researchers offer another concept for required speed to defeat a target. V_{50} ballistic limit is defined as the speed of a projectile against a target which at least 50 percent of projectiles that completely pierces the target [6]. This means V_{50} represents an experimental outcome of a target-projectile match. Namely, V_{50} stands for an approximation of target resistance against a threat type rather than an analytical determination. Actual procedure to determine the V_{50} is as follows. A target is hit at least six times by an impactor type at six different speed levels which are close to estimated ballistic limit velocity. The arithmetic mean of the lowest

three velocity levels causing full penetration and the highest three velocity levels resulting in partial penetration yields the V_{50} limit [7].
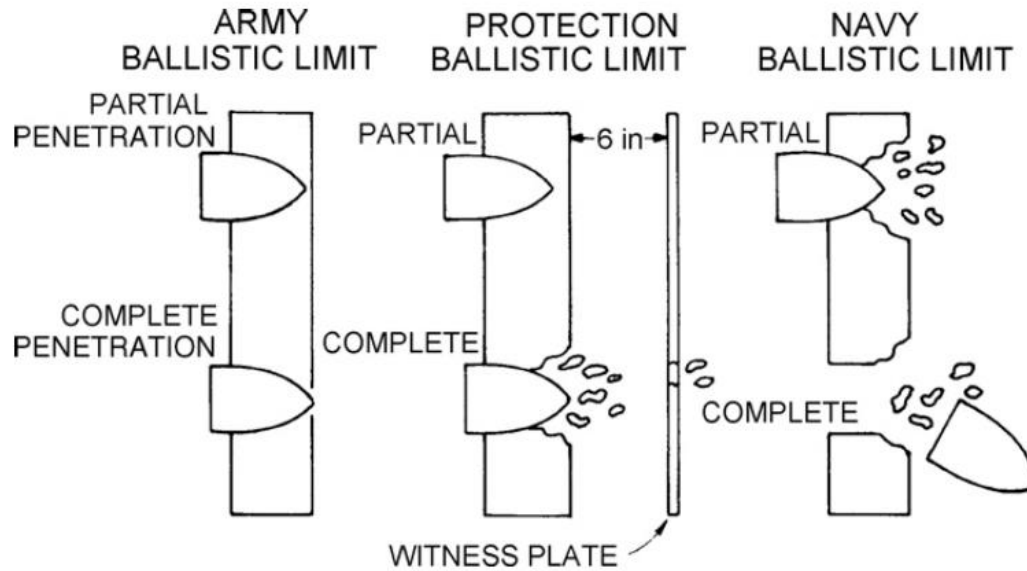
Figure 1 Ballistic Limit Definitions [8]

1.3. Classification of Threat Types

The delicate structures should be protected against high energy threats. The types of threat can be categorized in terms of their destructive effects. In order to gain a wide perspective, one should distinguish the threat types. There are some efforts to classify threat types with regard to their destruction mechanisms. Basically, there are 3 types of threats; Kinetic energy (KE) projectiles, improvised explosive device (IED) and chemical energy (CE) threats. The most well-known report on classification of threat types is done by NATO (North Atlantic Treaty Organization) Standardization Agency. In the literature, although there are other works to classify threat levels the publications of NATO are the most prominent ones, therefore other

classifications will not be discussed in detail here [9], [10], [11]. NATO Standardization Agency (NSA) has offered a standardization agreement (STANAG) on "Procedures for evaluating the protection level of armored vehicles" [12] which describes protection levels for KE and artillery threats. (Vol.1), mine threats (Vol.2), improvised explosive device (IED) threats (Vol.3) and chemical energy (CE) threats. Since this work covers only 7.62 mm armor piercing type bullet with hardened steel core against mild steel targets, the threat level is level 3 among the other levels of threats mentioned in Table 1.

Table 1 NATO Protection Levels AEP-5 Annex A [12]

KE Threat Level	Ammunitions	V_{proof} (m/s)
6	30 mmx173 APFSDS-T	-
	30 mmx165 AP-T	810
5	25 mmx137 APFSDS-T	1336-1258
4	14.5 mmx114 API	911
3	**7.62 mmx54 AP (WC core)**	**930**
	7.62 mmx54R B32 API	**854**
2	7.62 mmx39 API	695
1	7.62 mmx51 NATO Ball	833
	5.56 mmx45 NATO SS109	900
	5.56 mmx45 M193	937

1.3.1. Kinetic Energy Projectiles

According to NATO STANAG 4569 Kinetic energy projectiles (KEP) are classified into two classes:

- Small and medium caliber kinetic energy (KE) ballistic projectiles
- Fragment simulating penetrators (FSP) which represent artillery shell fragments (Figure 2)[13].
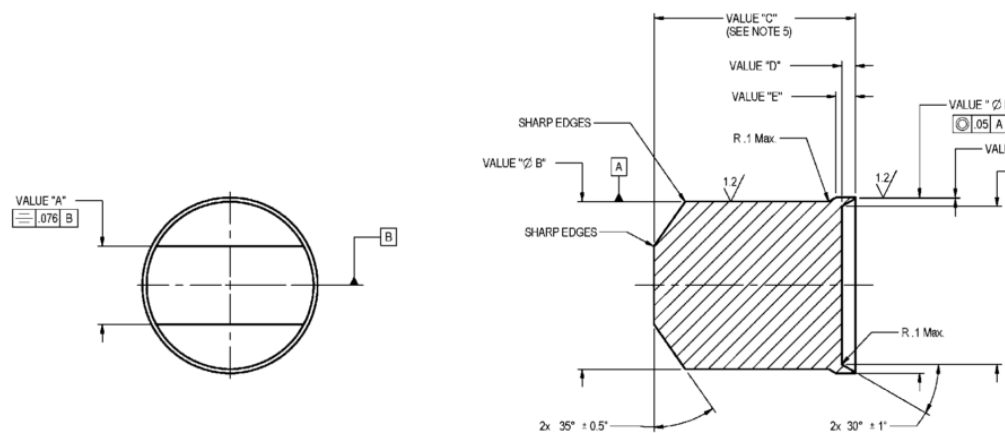
Figure 2 Standard Dimensions of a Fragment Simulating Projectile [13]

There are other KEPs used in investigations as well. The most common projectile types used for investigations are

- Long rod penetrators
- Blunt projectiles
- Conical nose projectiles
- Ogive or spherical nose projectiles
- Explosively formed projectiles.

Some researchers [14], [15], [16] used conical, blunt or hemispherical projectiles in their investigations and some others used long rod kinetic energy penetrators for

evaluating the effect of aspect ratio of the penetrator [17]–[20]. Long rod penetrators have a specific aspect ratio. Goldsmith defined the geometrical requirement for long rod penetrators. A long rod penetrator should have length to diameter ratio (L/D) exceeding 10 [3].

There are many types of bullets. Ballistic investigations are mostly focused on ball point type soft core projectiles and armor piercing type hard core projectiles. A cut view of a hardened steel core armor piercing (AP) bullet is presented in Figure 3 and the structure and the dismantled components of a AP bullet is shown in Figure 4.

Figure 3 7.62 mm AP Bullet Cut View [21]
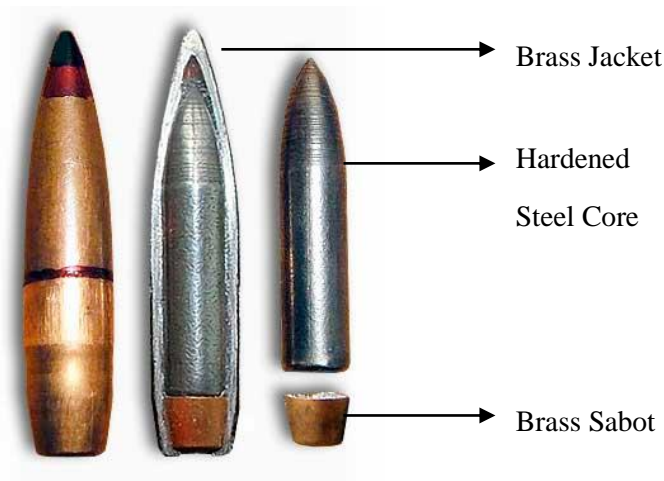
Figure 4 A Dismantled 7.62 mm AP Bullet [21]

Explosively formed projectiles (EFP) use the power of shock wave generated by detonation of highly explosive medium, a liner disk made of a ductile material is deformed and accelerated towards to the target. They are a special form of shaped charges (SC) and first used in WWII era [22]. Today they have a very broad area of use. They are used in novel applications such as anti-vehicle land mines and improvised explosive devices (IEDs). The structure and the working principle of EFPs are schematically explained in Figure 5.
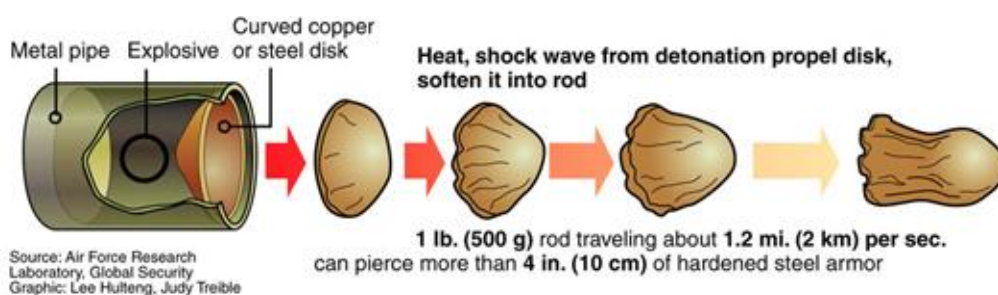
Figure 5 Illustration of the Principle of EFP [23]

1.3.2. Chemical Energy Threats

Thermobaric explosives (TBX) also called as solid fuel-air explosives (SFAE) have a great destructive effect in enclosed spaces like underground bunkers, tunnels, and battlefield fortifications. Thermobaric weapons generate highly intense heat and pressure to defeat targets instead of armor piercing shells or fragmentation [24].

1.3.3. Blast Loads

Detonation power of explosives generates blast loads. The explosion generates a pressure wave caused by expanding of hot gases moving outward at high velocity from its detonation point [25]. In open air explosions, this pressure wave is transmitted through surrounding air. However, in submerged explosions, pressure waves are transmitted through surrounding water. Because of the difference of compressibility properties of water and air, the transmission mechanism of pressure waves differs by surrounding medium.

1.4. Classification of Target Types

Various techniques have been employed for defeating the threat factor to reduce destructive effect, such as changing armor type and using the helping structures. Armor systems are classified by Rosenberg et al. [20] as active, passive and reactive armor systems.

Passive armors use high strength and ductile materials with unique designs to absorb kinetic energy of upcoming threat by not losing full functionality. In other words, target should decelerate or dissipate kinetic energy of the projectile until it completely perforates, breaks into pieces or loses functional form.

Passive armor systems against blast loads are broadly classified into four categories by Langdon et al. [26]. They are impedance mismatching, protective cladding, geometrical arrangements and using blast wave disrupters. These methods are used for eliminating the power of the blast.

While passive armors are designed to absorb kinetic energy of upcoming threat factor, active armor systems require a triggering mechanism in order to cancel approaching momentum by deploying an internal system [27]. Armors having active systems should have some parts to be activated and propelled against the threat upon impact on the target are called as active armors. Reactive armors are activated some distance away while approaching of the threat to the target [20]. Reactive systems require much more complex structures to sense upcoming threat to take action until the impact. Armor systems can be in the form of metal, ceramic, polymer composite or any combinations of these.

1.5. Armor Materials

Various types of steels are used as armor materials. However, areal density of steel is rather high. For this reason, researchers look an alternative way of using other lightweight materials to reduce weight and cost. However, changing the material could be costly. This motivation directed some researchers to do extensive research in reducing armor weight [28]. Novel aluminum alloys provide high strength properties that makes aluminum alloys area of ballistic interest. Advanced ceramics and polymer composite structures are other advanced materials providing less weight and giving promising results. In some advanced applications, these materials replace aluminum and steel. Their manufacturing cost is comparatively high.

The idea of building an armor structure from composition of multiple materials instead of a single material is becoming more popular. Researchers try to find best target type and configuration that provides maximum ballistic limit. Different

combinations of materials are used in investigations, such as metal+metal, ceramic+metal, polymer composite+ceramic, etc... Even changing the material at impact side can influence velocity drop of the projectile. For example, putting a high ductility or high hardness material to impact side can influence the ballistic limit appreciably.

1.6. Scope of the Thesis

Existing reports in the literature focus on single plate penetration or multiple plate penetration with parallel arrangement. However, the effect of obliquity of each plate has not been fully investigated. After oblique perforation of a target the bullet starts yawing motion and tumbling as well. Its impact to the next layer would be yawing impact and its perforation behavior has not been fully investigated. Kinetic energy loss of projectile at succeeding layers depends on the configuration and the thickness of preceding layers. This work focuses on kinetic energy loss of a 7.62 mm AP bullet by piercing spaced targets of different thicknesses different degrees of obliquity. The main goal of this thesis is to find a good target configuration to decrease penetration ability of a 7.62 mm AP bullet by exploiting the tumbling effect of bullet at oblique impact while considering the spacing of targets as well. The bullet should impact to the target as much as far away from its sharp nose. The bullet is preferred to impact with its secant radius zone or with bearing surface to decrease its penetration ability (Figure 6).
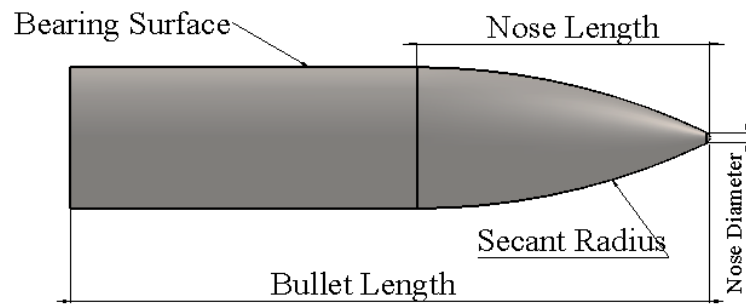
Figure 6 Names of The Major Parts of The Bullet Core

CHAPTER 2

LITERATURE SURVEY

High speed penetration mechanism has been a branch of interest for a long time to the researchers conducting a research on weapon and armor development. Early studies have been made on quasi-static penetration of hard indenters [29]. However, the nature of impact problems requires a much wider approach in order to develop an analytical model to describe high speed penetration mechanism.

Recht & Ipson [30] proposed analytical models of perforation dynamics for monolithic plate target. They have found some crucial relations on V_{BL} and residual velocity of a projectile considering normal and oblique impact cases provided that pre-impact velocity of the projectile is known [31]. Their predictions on residual (post-impact) velocity of the projectile after perforation of the target are based on the conservation of momentum, energy balance and momentum-impulse law principles [32]. Their model has been found consistent with later experimental studies. However, Recht & Ipson did not take the dynamic material properties into consideration in their model. Furthermore, they did not consider the nose shape of the projectile.

Besides, there is a need for a description of the material behavior in order to have a more precise solution and the stress-strain distribution in the target.

Johnson & Cook [33] proposed a constitutive equation for material behavior at high strain rate deformations. This attempt to describe material behavior was later modified by some authors. Modified Johnson-Cook (JC) Model for the von Mises yield stress includes non-linear isotropic hardening mechanism, strain-rate

hardening, temperature softening due to adiabatic heating caused by impact energy of the material [33],[34]. There are other efforts to model material behavior caused by impact loading such as Zerilli-Armstrong model which took the atomic lattice structure into account [35],[36]. Since JC model is purely empirical and is easy to apply on computational scheme, it has become the most widely used constitutive model among other proposed models.

There are numerous reports of impact cases on metallic targets. Much more recent works are published in open literature dealing with other type of target materials, however, they are out of the scope of this work.

Ballistic penetration studies focused mainly on rigid or deformable projectile assumptions Investigations are made concerning the effect of nose shape, obliquity, layering and spacing between targets. Ballistic penetration properties of projectile-target match are also investigated to find the effect of projectile mass as well as the target thickness and target material properties such as hardness and ductility. More recent studies consider the target inertia as well [37].

2.1. Normal Impact

Goldsmith [3] defined the normal impact as a projectile moving with purely translating motion along its geometrical centerline hits a target making a 90 degree angle with the target surface. In other words, the projectile trajectory (or velocity vector) and its geometrical centerline should coincide with the surface normal as depicted in Figure 7.
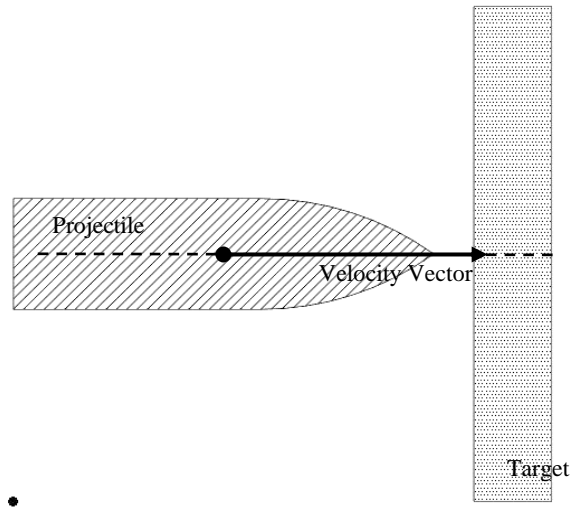
Figure 7 Illustration of Normal Impact

The angle of incidence is the angle between the surface normal vector and the velocity vector of the projectile [38]. Hence, zero angle of incidence defines the normal impact case.

Since the ballistic behavior of the materials could not fully be understood, a vast majority of the analyses on the ballistic studies have been conducted on normal impact cases.

2.2. Oblique Impact

If the relative angle spanned by target surface normal and projectile velocity vector has a value other than zero, the projectile will hit the target with an oblique angle. This angle also called as NATO angle [39]. Oblique impact, sometimes also called the target obliquity, refers to such impact conditions. Physically speaking, due to the gravity, flight of a projectile is affected by the gravitational load, and its trajectory deviates from the normal direction. The more the time of the flight

increases, the more the velocity of the projectile increases in the direction of gravitation vector. Therefore, the duration of flight of the projectile increases the yawing motion of the projectile.

Furthermore, obliquity of a target increases the line of sight of the projectile as can be seen in Figure 8. It is reported that when the increased line of sight is combined with the effect of obliquity, the ballistic resistance of a target also increases [19].
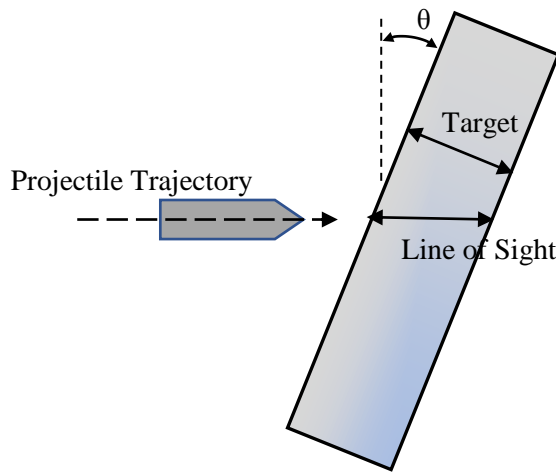
Figure 8 Line of Sight Thickness and Target Thickness

2.3. Yawing Impact

Yawing impact is a more complex phenomenon. The direction of flight and the geometrical centerline of the projectile both makes an angle with the surface normal of the target as shown in Figure 9 and Figure 10.

The yawing motion should not be confused by the terms used in aircraft principal axes (Yaw-Pitch-Roll). The yawing impact of a cylindrical projectile is almost a standard definition for non-ideal impact cases [3]. The yaw is defined as the angle between the projectile velocity vector and the centerline of the projectile. Considering the flight of the bullet in 3D space there are two components of the yaw in orthogonal axes. The total yaw is composed of horizontal and vertical yaws

[40]. The tumbling impact term incorporates one additional motion of the bullet. Besides the translation motion, the bullet rotates with an angular velocity about an arbitrary axis crossing and perpendicular to the bullet centerline [3]. Figure 9 illustrates the difference between obliquity, tumble and yaw.
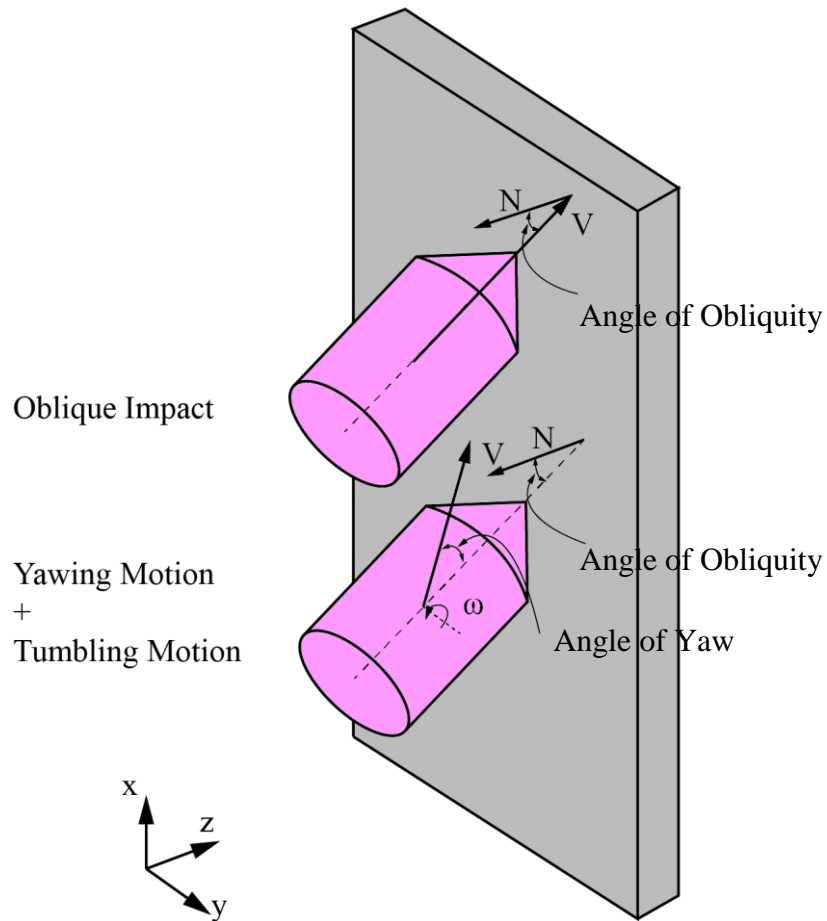
Figure 9 Illustration of Obliquity, Yaw and Tumble

The simplest method to determine the amount of yaw is using simple materials which will not change projectile instability. Yawing cards or witness sheets are used to determine the amount of yaw. Projectile yaw is an important parameter when determining the validity of the impact tests according to NATO AEP-55 [12]. The

yaw cards placed in the flight path, and the perforation signature of the projectile on these cards shows the amount of yaw.
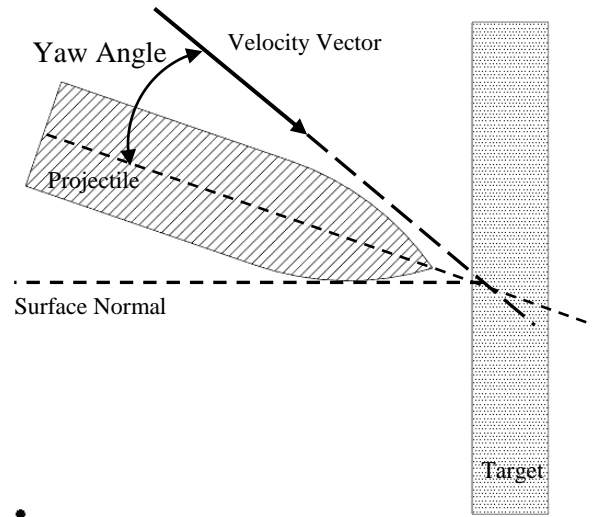
Figure 10 Illustration of Yawing Impact

2.4. The Effect of Impact Variables

In the literature, low strength and high strength projectiles are used in investigations. Therefore, reports on rigid or deformable projectile assumption are available in the literature depending on the nature of the problem. The rigid projectile assumption can reduce the computational cost. However, by making this assumption, some elastic and plastic deformations on the projectile are neglected [41]. In fact, this assumption is not appropriate for hard target-soft projectile matches. Especially, the impact of moderate and thick targets of high strength would not give a reliable data for the rigid projectile assumption.

2.4.1. The Effect of Obliquity

There is a target-projectile-specific angle of obliquity at a speed level for an appropriate projectile. Increasing the angle of obliquity (also called NATO angle) (Figure 11) will eventually cause the projectile to completely bounce back from the target. This event is total ricochet of the projectile.

Iqbal et al. [42] investigated the effect of target obliquity and the nose shape of the projectile numerically for Weldox 460 E steel targets using ABAQUS/Explicit software. They reported that increasing the target obliquity would cause an increase in the ballistic limit. They also evaluated the critical ricochet condition and how the parameters affect ricochet of a projectile. The critical ricochet angle was found as an increasing function of impact velocity. Namely, keeping other variables constant, if the impact velocity is increased for a given nose type, the angle of target obliquity should also be increased for the ricochet of the projectile. They also stated that the nose angle plays a primary role in ricochet. Together with nose type, the impact velocity can influence the critical angle of ricochet.
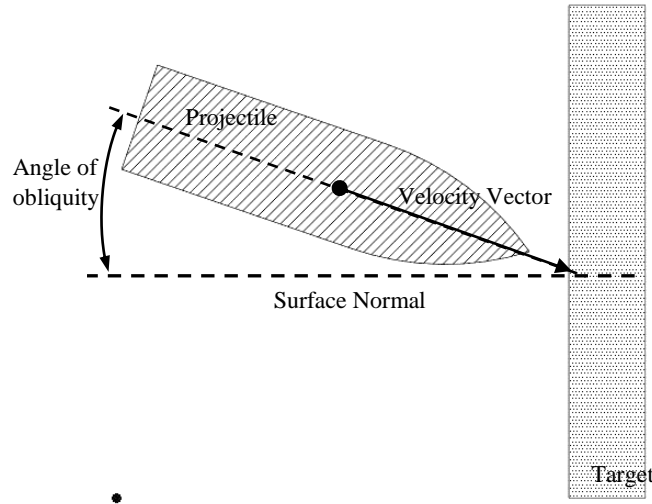
Figure 11 Oblique Target Impact

19

2.4.2. The Effect of Nose Shape

Early efforts on ballistic studies focused on flat nose projectiles. By changing the nose shape of the projectile, it has become possible to see the failure modes of the target shift from plug formation to hole enlargement and to petal formation in some cases.

Børvik et al. [43] have made numerical and experimental studies to understand the behavior of 12-mm-thick Weldox 460 E steel targets against different nose shape projectiles. The projectiles they used had blunt, hemispherical, and conical noses and were 20 mm in diameter. The hardness of the projectiles was 53 HRC to minimize plastic deformations on the tip of the projectile. After numerous experiments, they found that nose shape has a significant role in the ballistic limit velocity of a target. For investigated nose shapes, blunt projectiles had the least ballistic limit velocity when compared to hemispherical and conical nose projectiles. Global deformations at target plates explains the failure modes and energy absorption mechanisms. Figure 12 shows the cross-sectional view of the highly-deformed targets subjected to the three main nose types of projectile impacts. In Figure 12, straining directions of the target section and the failure mechanism can be observed. Conical projectiles spend less energy for perforation at some level of impact velocity. However, at higher velocity regimes blunt projectiles require the least energy for full perforations. More plastic deformations at targets impacted by conical nosed projectiles are observed. The amount of deformation also explains the failure modes of target, and the frictional effects start to play important role during perforation.

20
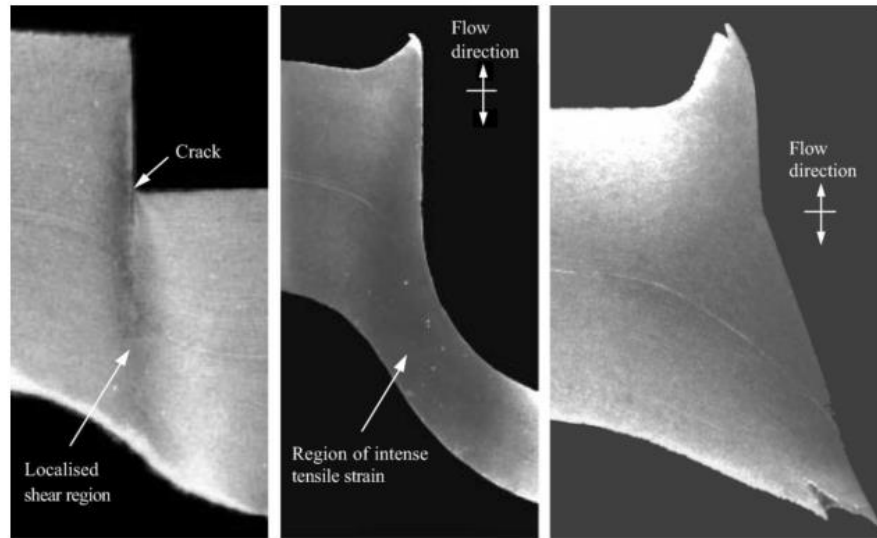
Figure 12 Local Deformations of Targets Against Different Nose Projectiles [43]

Kepnyigba et al. [16] made a similar numerical and experimental investigation using 1-mm-thick mild steel sheets using hemispherical, conical and blunt and projectiles of 13 mm in diameter and impact velocity of 141 m/s. According to their experimental results, the dominant failure mechanisms were plugging and petaling among the mechanisms presented in Figure 13.
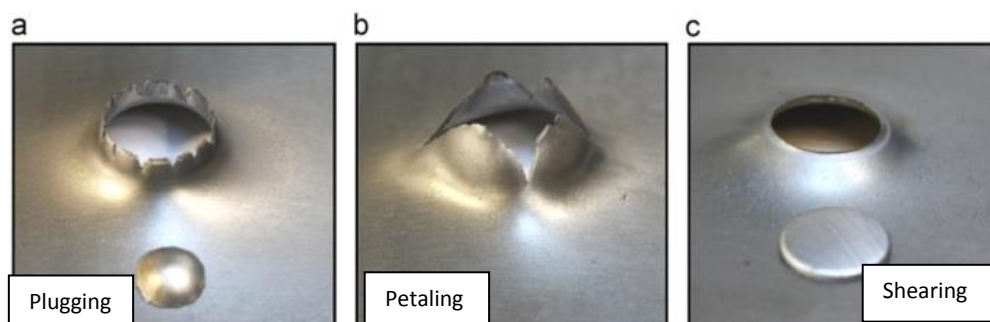
Figure 13 Main failure modes [16]

A detailed numerical investigation was made by Iqbal et al. [44]. In addition to approximation by Børvik et al., Iqbal et al. investigated the effect of conicity of nose and the effect of caliber radius head (CRH). They used 12 mm thick Weldox 460 E steel for conical nosed projectiles and 1 mm thick 1100-H12 aluminum targets impacted by ogival projectiles. Projectiles having same weight but different nose shapes used in numerical investigations are presented in Figure 14.
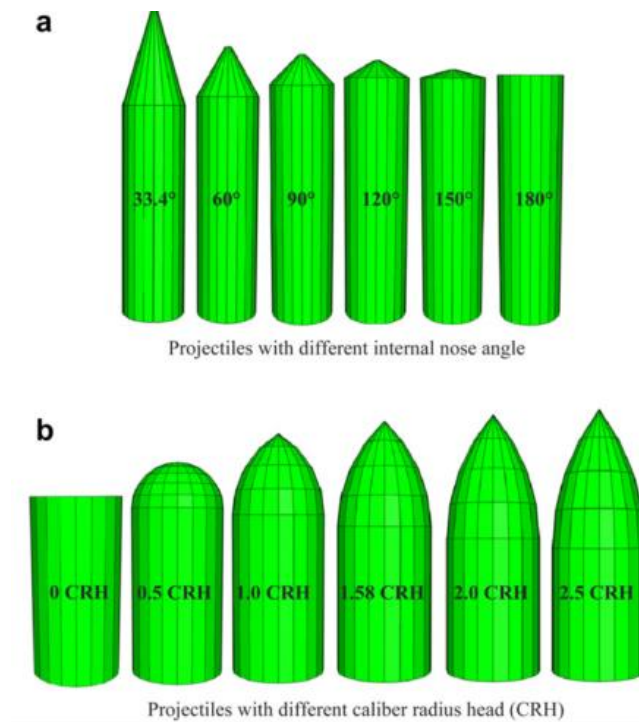
Figure 14 Various Projectile Nose Types Used In Investigations [44]

They reported that the nose type and shape greatly affect the failure mode of the target. The nose shape can influence the global deformation at the target material especially close to ballistic limit velocity. For example, the target is failed through ductile hole formation with sharp projectiles, while the blunt projectiles cause shear plugging at the target plate. However, a combination of two failure modes is observed with the 90^0 nose angle projectile. It was found that if the nose angle

increased, plastic deformation at target plate would decrease. On the other hand, ogival nosed projectiles with 0.5 CRH (hemispherical) cause thinning and tensile stretching of the target plate prior to failure. Furthermore, they found that changing nose shape has more effects on the failure mode. The projectiles having 1.0 CRH to 2.0 CRH cause failure of the target through ductile hole enlargement and petal formation. A solid evidence can be found in their report that an increase in conicity of the projectile nose would increase the ballistic limit as well. Similarly, increasing the amount of CRH would also increase the ballistic limit with one exception: the hemispherical nose (0.5 CRH) offers the lowest ballistic limit.

Gupta et al. [14] used blunt and hemispherical projectiles. They reported some important results coinciding with the results of the previous experimental studies. Projectiles having high velocities present less velocity drop against the same target. At low velocity regimes, hemispherical projectiles present a greater kinetic energy drop. In contrast, in higher than 100 m/s both types of projectiles present almost the same amount of kinetic energy drop. Another point they mentioned is thin plates represent more bending against hemispherical projectiles. However, sharp edges of flat face projectiles cause stress concentration at the edge of the projectile and, they induce rapid failure at this zone. Their experimental results are presented in Table 2.

Table 2 Effect of Projectile Nose Shapes [14]

Projectile Type	Incident Velocity V_i (m/s)	Residual Velocity V_r (m/s)	Velocity Drop (m/s)	Absorbed Kinetic Energy (J)	Projectile Kinetic Energy Loss (%)	Global Deflection (mm)
Blunt	115.6	92.9	22.7	124.2	35	8.9
Hemispherical	114.7	92.3	22.4	109	35.3	12.3
Blunt	92.5	67.5	25	105	46.7	11
Hemispherical	92.3	63.5	28.8	105.4	52.6	15.8

There are novel perspectives on the effect of nose shapes. Iqbal et al. [45] worked on three different double nosed projectiles as presented in Figure 15 and their impact on aluminum plates.
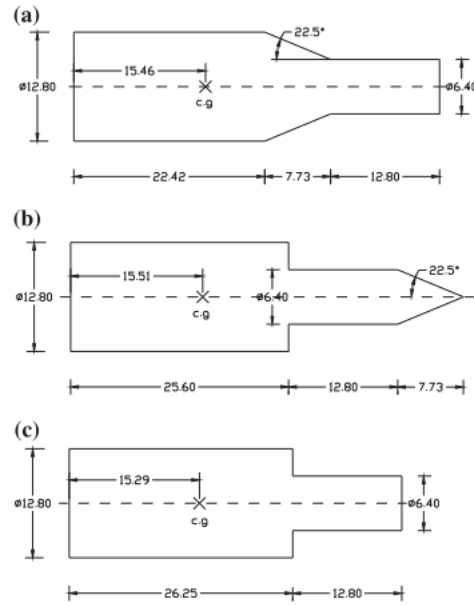
Figure 15 Schematics and Dimensions of Double Nosed Projectiles by Iqbal et. al. [45]

They found that blunt-type projectile requires more perforation energy than the other types of projectiles.

Numerical analysis of plugging formation and failure upon a limit were investigated by Børvik et al. [46]. They made a series of numerical calculations using LS-DYNA software with rigid blunt projectiles simulating different impact cases. As they discussed, stress concentrated around the sharp edge of the tip of the projectile. This stress concentration causes microcracks following the growth of micro voids created in the structure, and results in development of shear bands. As the plastic strain reaches a critical value some amount of material is plugged out of the rear side of the target.

2.4.3. Effect of Target Hardness and Strength

Analytical expressions available in the literature which describe the work required for penetration of a projectile into a target plate always contain the target material strength [47],[48].

Demir et al. [49] studied penetration of 7.62 mm Armor Piercing (AP) projectiles into various alloys of aluminum and steel targets of different areal densities and hardness level ranging from 38 to 60 HRC. Areal density can be defined as the product of target effective thickness and target density. If the target is composed of several layers having different densities and thickness, total areal density can be calculated by multiplication and summation of density and the effective thickness of each layer (Eq.(1)).

$$Areal\ Density(AD) = \sum_{i=1}^{n} \rho_i t_i'$$

(1)

Where t_i' denotes the effective thickness of ith layer.

As mentioned in their study, AP projectile core is made of DIN 100Cr6 high carbon-chromium steel and have hardness of 61 HRC. This makes the bullet core much harder than the target material. Target material as AISI 4140 has a wide range of mechanical properties such as yield strength from 1150-1800 MPa depending on the tempering conditions. Target material as 7075-T651, 5083-H111, 7075-T0 and 7075-T7351 have yield strength ranging from 190-435 MPa. From experimental procedures, it is reported that failure mechanism depends on both areal densities and hardness of the material at the same time. Low hardness steels are perforated via forming a ductile hole enlargement as one can see in the aluminum targets. Target hardness of 53 HRC was found the best among the other steel materials investigated. If the hardness level of the target is increased to 60 HRC, target fractured into several pieces depending on the target thickness. However, 7075-T651 is found as the best target material.

Übeyli et al. [50] investigated effect of heat treatment and the enhanced physical properties of steel targets against 7.62 mm AP bullets. According to the authors, the ballistic performance of the target material significantly depends on the martensite content.

Dikshit et al. [51] investigated the influence of plate hardness on the penetration of thick rolled homogeneous armor (RHA) plates. Armor plates have hardness of HV295, HV440 and HV520 are tested with 20 mm cylindrical ogival nosed projectiles having HV600 hardness. They concluded that the critical velocity for perforation of the target by plugging failure, increases with decreasing the hardness of the plate. In addition to this, the effect of hardness of a plate becomes a dominant factor considering the plane stress or plane strain. When projectile target interactions take place under plane strain condition, high hardness has positive impact on ballistic resistance of the target. On the other hand, under plane stress conditions, increasing the target hardness initially increases the ballistic resistance up to some level of material hardness level, however, further increment in the plate hardness weakens the target against projectile impact under investigated conditions.

Aly et al. [8] reported that energy spent for perforation of steel targets greatly reduces by increasing the projectile hardness. Thus, modelling the projectile as an analytical rigid object will cause some degree of error. They reported that ballistic resistance of a target could be increased by 25% if the bullet hardness to target hardness ratio is decreased from 1.5 to 0.7.

Iqbal et al. [52] made a number of numerical investigations on Weldox 460 E steel and 1100-H12 aluminum materials. They saw that impact velocity close to ballistic limits cause the higher global deformations on targets. According to the numerical results global deformations at the targets were found to decrease and got stabilized above ballistic limit impacts.

Dey et al. [53] investigated the effect of target strength and nose shapes against three different targets being 12-mm-thick. They found that the ballistic resistance of

a target decreases for increasing the yield strength of the target plate (Figure 8), however, an opposite trend was seen when the nose shape is changed to ogival and conical type. Ballistic limit velocity of the projectile and the target strength can be compared for three different nose types in Figure 14.
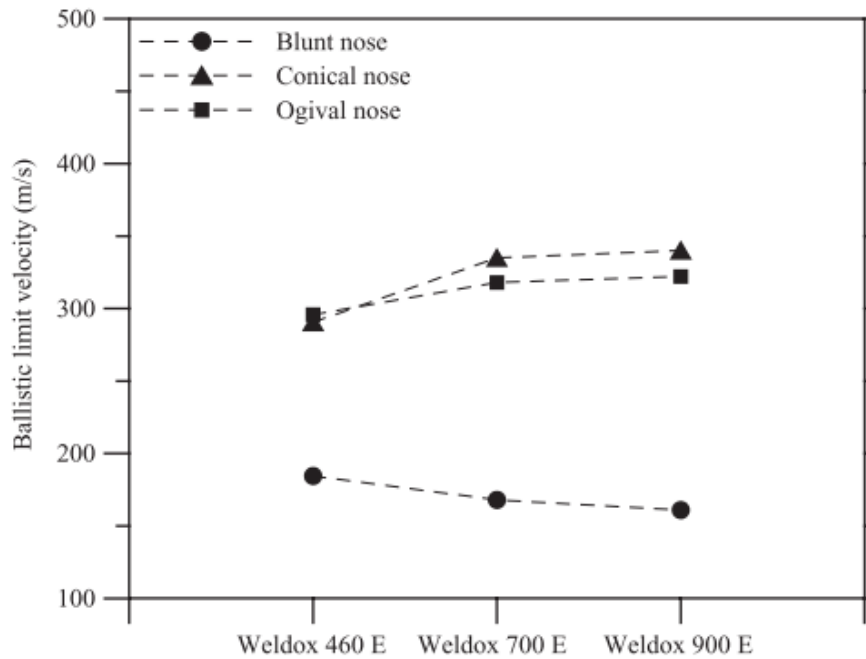
Figure 16 Effect of Target Strength and Nose Shape [53]

2.4.4. Effect of Lamination, Spacing, Layering Sequence and Order of Layers

Teng et al. [54] made some numerical investigations on layering and spacing of the targets. They found that a layered target system composed of a high ductility metal plate as front plate and low ductility but high strength metal as back plate is found as the best sequence of layering at low impact velocity against conical and blunt nose impactors. Contrary to this configuration, if the front layer is chosen as low ductility metal and the back plate is chosen as high ductility material is the worst one.

28

A more comprehensive analysis was made by Teng et al. [41]. They used four types of projectiles having different nose shapes and weights which represent fragmentation threat produced from explosion of improvised explosive devices (IEDs). As they reported double layer configuration against blunt projectiles give as 25% higher ballistic protection comparing to monolithic target. However, for conical nosed projectiles this trend changes. Double layer configuration was found as it weakens the structure. Their work revealed that increasing the spacing between target plates does not contribute to ballistic effectiveness of a target.

Woodward & Cimpoeru [47] stated that laminating of a monolithic target does not cause a significant increase in the ballistic limit. Namely, layering has negative impact on ballistic resistance of a target as long as the total thickness is kept constant.

From experimental and numerical results, Babaei et al. [32] found that if a target composed of two layers of steel-aluminum (st-al) and impacted by deformable blunt nose projectiles having a slenderness ratio L/D=8, it would have a higher ballistic resistance compared to the target of same total thickness but reversed the sequence of the layers (al-st). As one can see in Figure 17 changing the sequence of the layers enhanced ballistic resistance of the target system.
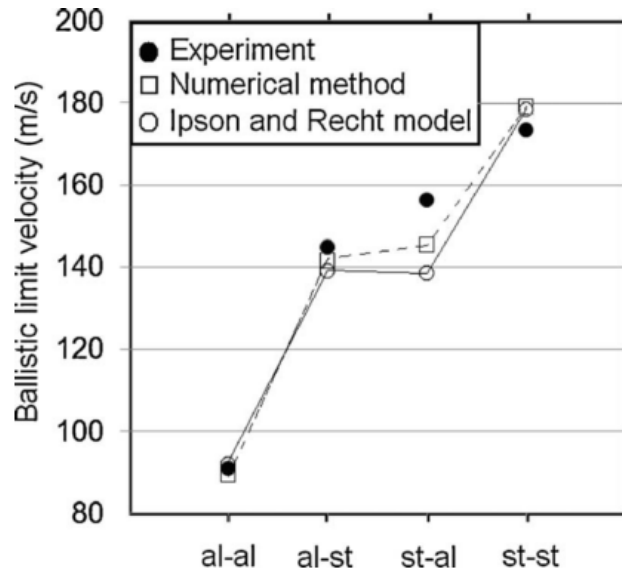
Figure 17 Effect of the Sequence of the target layers [32]

Yunfei et al. [55] discussed the effect of layering in detail. They reported that monolithic targets have higher ballistic limit velocities than layered targets subjected to ogival nosed projectile impact for the same total thickness. However, if the nose shape is changed, ballistic limit of the target is influenced from this change and layering becomes an alternative to monolithic arrangement. Furthermore, ballistic limit of the target and the strength of the projectile have close relation. From their analyses, they noted that a higher ballistic resistance is observed, irrespective of the nose shapes, when a low strength projectile strikes to a multilayered target system compared to a monolithic target.

As reported in the literature, spacing of the layers does not affect the ballistic limit significantly for the normal impact cases [56],[57],[58]. However, spacing of the laminated targets contributes to the ballistic resistance of obliquely layered target.

Zukas et al. [59] investigated the effectiveness of layered targets. They have found that bending stiffness of the plate affects ballistic resistance of a target. The bending stiffness of a plate is given as in Eq.(2).

$$D = \frac{Et^3}{12(1 - v^2)} \tag{2}$$

where t is the plate thickness and E, v are Young's modulus and Poisson's ratio respectively. As they reported, layering a thick target by reducing the thickness will dramatically weaken the total structure. For instance, by reducing the thickness of a plate by half will reduce bending stiffness of the plate 1/8. They noted that for the normal penetration problems spacing of layers weakens the ballistic resistance and therefore should be avoided.

Zhou et al. [60] reports that multi-layered targets have higher ballistic resistance compared to monolithic plates having same equal total thickness. The superiority is due to the global deformations of laminated plates. Therefore, laminated targets deform by bulging and cause more energy to be absorbed. Although for normal impact problems spacing has negative effect on ballistic resistance, choosing an appropriate spacing could improve the target resistance. However, Radin and Goldsmith [61] found that spacing and layering have negative impact on ballistic resistance. This result is because of layering reduces the bending resistance.

Zhou et al.[60] tabulated the previous experimental studies as shown in Table 3.

Table 3 Comparison of Some Investigations [60]

Reference	Type of Study	Projectile	Proj. Nose Shape	Proj. Radius (mm)	Target Thickness (mm)	Number of Layers	Range of Impact Speed (m/s)	Results
Marom [62]	Experimental	Al	Round	2.8	10	3	350-390	$\Delta E^a < \Delta E^b$ $\Delta E^c < \Delta E^b$
Corran [63]	Experimental	Steel	Flat	6.25	6.4	3	40-220	$\Delta E^a < \Delta E^b$
Radin [61]	Experimental	Al	Flat-Conical	6.25	6.4	4	80-240	$V^a_{50} > V^b_{50}$
Gupta [64]	Experimental	Mild Steel-Al	Ogive	3.1	25-40	6	800-870	$\Delta E^a > \Delta E^b$
Almohandes [65]	Experimental	Steel- FRP	Ogive	7.62	8	5	706-826	$\Delta E^c < \Delta E^b$ $\Delta E^a > \Delta E^b$
Zukas [59]	Numerical		Round	6.5	31.8	6	1100	$\Delta E^a > \Delta E^b$
Elek [66]	Analytical	Steel	Flat	2.8	3.45	2	70-830	$\Delta E^a < \Delta E^c$
In this table, ΔE represents the kinetic energy loss of the projectile where ΔE^a denotes monolithic target, ΔE^b is layered in-contact target, ΔE^c is layered with spacing target								

2.4.5. Effect of Target Thickness

Aly et al. [8] and Børvik et al. [40] reported that ballistic resistance of metallic plates depends on their thickness. But as Iqbal et al. [67] and Iqbal et. al. [52] found that the ballistic limit increases with a slower rate with target thickness. As they reported, critical kinetic energy required for full perforation of a target first increases rapidly by the increase in the target thickness then remains almost constant even if the target thickness increases further and then increases again rapidly. The reason of this response of the target is explained as changing the failure mode of the material. By increasing target thickness, the failure mode shifts from thin plate stretching to thick plate shear deformation. As they reported doubling the

target thickness will not eventually double the ballistic limit velocity. Even more, they also report that considering some impact cases, increasing the target thickness will increase ballistic limit only 30%.
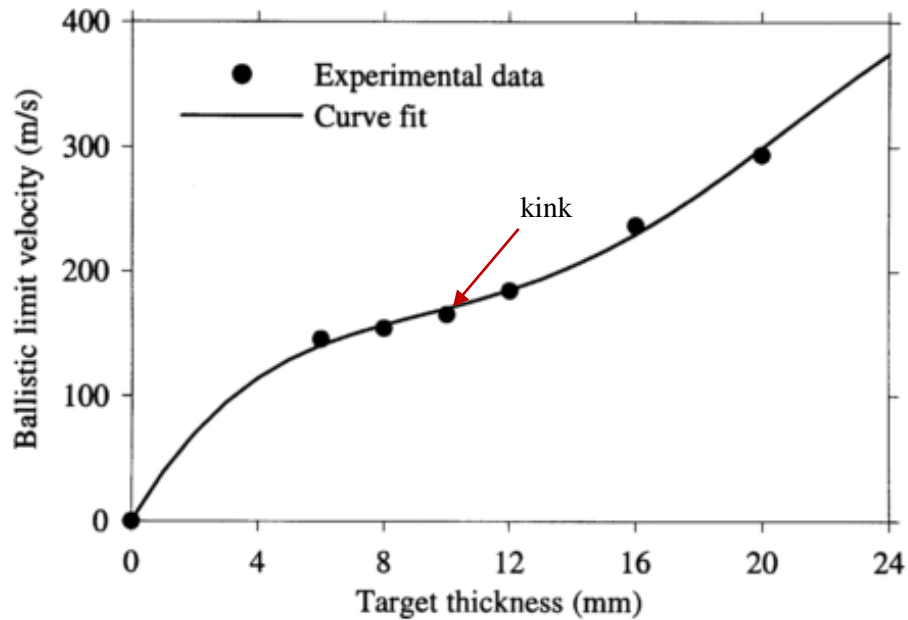
Figure 18 Ballistic Limit vs Target Thickness [40]

As one can see in Figure 18 the trend of increasing ballistic limit changes at "kink" value. The kink value represents the point at which the dominant failure mode of the monolithic target shifts from stretching to shearing [68]. Deng et al. [57] also stated the same phenomenon; using the multilayered targets of the total thickness below a kink value offers no advantage. In order to take the advantage of layering of the structure, the total thickness of the target should be greater than a specific value which can be experimentally obtained.

Durmuş et al. [69] experimentally investigated 2-mm and 1-mm-thick steel plates with 9-mm soft core bullet. They found that 2-mm-thick plate has superior ballistic resistance to 1mm thick steel plate. Experimental results showed that thicker steel plate has almost 3 times stronger than the thinner plate. Layering the 2 mm

monolithic target as two 1 mm adjacent plates (2x1 mm) weakens the whole target by 9%.

2.4.6. Effect of Mass, Incidence Velocity, and Initial Kinetic Energy

Gupta et al. [70] found that if the projectile velocity is increased localized deformation of the target decreases. Same phenomenon was also confirmed by Iqbal et al. [71]. They performed numerous experiments using a pneumatic gas gun and launched an ogive nosed projectile at different incidence velocities. They found that kinetic energy absorbed by the target plate decreased slightly if the incidence velocity is increased. According to their findings at high impact velocities bending effect of the target tends to decrease and has an insignificant importance in kinetic energy drop of the projectile.

Teng et. al. [41] used four types of projectiles with rigid assumption. They are all different nose shapes and weights as shown in Figure 19. They found that using a blunt nose projectile it is possible to increase the ballistic limit velocity by 25% by utilizing two-layer configuration instead of monolithic target with the same total areal density.
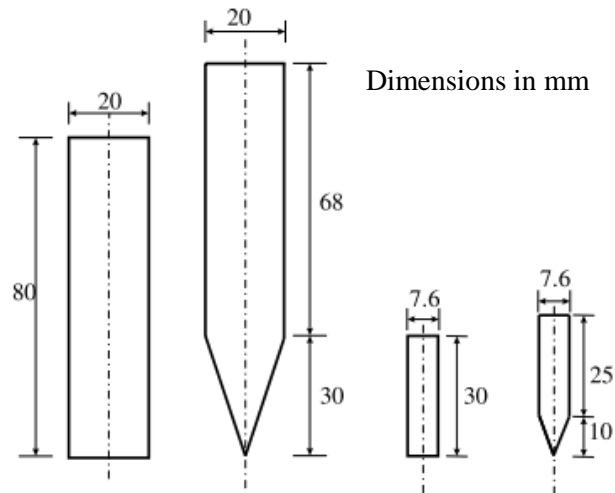
Figure 19 Dimensions of Four Cylindrical Projectiles Considered by Teng et. al.

[41]

The numerical results have indicated a very crucial result. Layering of a target slightly impairs the target resistance against conical nosed rigid projectile. Furthermore, as per their findings, leaving a small gap between the two plates or arranging in-contact type would not enhance the ballistic limit. The effect of nose shape, layering and the projectile kinetic energy are tabulated in Table 4.

Table 4 Ballistic Limit Velocities of Different Projectiles [41] (This table is produced by using the information given in Ref. [41])

Heavy, Blunt Nose Projectile			Heavy, Conical Projectile		
Monolithic Target	In-Contact Target	Spaced Target	Monolithic Target	In-Contact Target	Spaced Target
186.1 m/s	232 m/s	236 m/s	305.9 m/s	282 m/s	280 m/s
Light, Blunt Nose Projectile			Light, Conical Projectile		
Monolithic Target	In-Contact Target	Spaced Target	Monolithic Target	In-Contact Target	Spaced Target
487.4 m/s	520 m/s	523 m/s	525.9 m/s	524.5 m/s	522.5 m/s

A similar study has been conducted by Teng et al. [54]. They investigated both nose shape, impact energy, layering and layer sequence of the target structure. The projectile weights are selected as 200 g and 30 g simulating the fragments caused by IEDs. The target materials are selected as Domex Protect 500 and Weldox 460 E steels. The target thicknesses are selected 6 mm for layered targets and 12 mm for monolithic targets. Velocity drop characteristics are plotted for different layering conditions as shown in Figure 20.
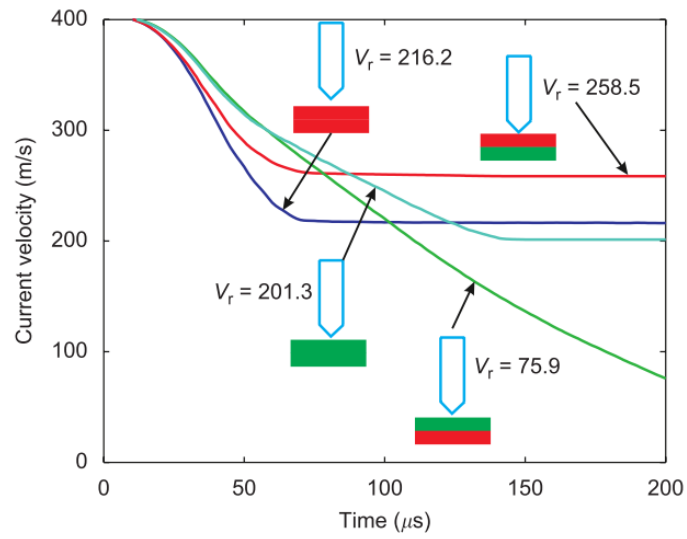
Figure 20 Velocity Drop Curve of a Heavy - Conical Nose Projectile Having 400 m/s Impact Velocity [54]

The velocity drop trend in Figure 20 changes with increased impact velocity. For the cases of using the same projectile and layers but only the projectile striking velocity being doubled, the results of the simulations are plotted in Figure 21 and the experimental results are tabulated in Table 5.
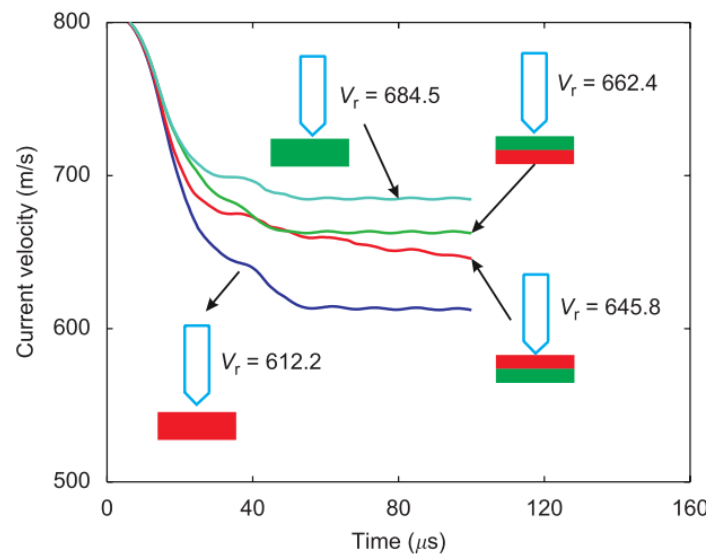
Figure 21 Velocity Drop Curve of a Heavy - Conical Nose Projectile Having 800 m/s Impact Velocity [54]

Table 5 Comparison of Impact Energy and Nose Types [54]

	V_r for Heavy - Conical Nose (m/s)	Projectile Kinetic Energy Loss	V_r for Light - Conical Nose (m/s)	Projectile Kinetic Energy Loss	V_r for Light - Conical Nose (m/s)	Projectile Kinetic Energy Loss
Domex Protect 500 Target	612	58.52 %	461	33.3 %	216	29.17 %
Weldox 460E Target	684	73.1 %	593	55 %	201	25.33 %
Projectile Mass (g)	200		30		30	
Impact Speed (m/s)	800		800		400	

CHAPTER 3

ANALYTICAL APPROACHES TO PENETRATION AND PERFORATION OF PLATES

There are numerous work on modeling of penetration of a projectile into solid targets. Since it is limited to verify the analytical expression by physical simulations, early efforts considered the impact cases below 250 m/s. Those works mainly focused on simple geometries such as blunt nose cylindrical projectiles. However, developments of test methods and precise tools required for measurement of projectile velocity brought researchers to focus on high velocity impact cases with much advanced geometries. Although there are many models proposed for penetration of brittle materials such as glass and ceramic materials [72] or composite structures [60], the scope of this thesis covers only metallic targets. For this reason, penetration models other than metallic targets will not be discussed in this work.

3.1. Analytical Models of High Speed Penetration

3.1.1. De Marre (1886)

Probably the oldest model for perforation energy for steel plates offered by De Marre [73]. This empirical formula is based on experimental observations and data fit. He considered neither of the projectile nor of the target strength in his empirical relation given in Eq.(3).

$$E_c = a d_p^{1.5} h_o^{1.4} \qquad (3)$$

Where E_c is the minimum energy required for perforation of the target, a is a parameter determined from a series of tests should be conducted with a given target-projectile set and d_p denotes the projectile diameter and h_0 denotes the initial target thickness.

3.1.2. Stanford Research Institute Formula (SRI) (1963)

SRI formula is another empirical relation on estimation of critical energy required for perforation of a target with a projectile. It contains target material ultimate tensile stress σ_u, projectile diameter d_p, initial target thickness h_0 and target span l (lateral dimension). However, this model given by Eq.(4) is proposed only for a limited velocity regime $(21 < V_0 < 122 m/s)$ along with some dimensional restrictions of target plate and projectile.

$$E_c = \frac{\sigma_u d_p}{10.29}(42.7h_0^2 + lh_0) \tag{4}$$

SRI model later modified by Neilson (1993) for hemispherical nose projectiles and applicability range is extended to higher velocity ranges (Eq.(5)) [73].

$$E_c = 0.9\sigma_u d_p^3 (\frac{h_0}{d_p})^{1.7}(\frac{l}{d_p})^{0.6} \tag{5}$$

The above model is called as Modified SRI model (m-SRI) and it is valid for a wider impact range of $100 < V < 250$ m/s.

3.1.3. Ballistic Research Laboratory (BRL) Formula (1968)

Ballistic Research Laboratory (later converted to Army Research Lab) proposed an expression (Eq.(6)) which yields energy required for plate perforation studies after a

series of tests conducted. Main difference of this model from its predecessors is the perforation energy does not depend on the target span to thickness ratio if it is greater than 150 [8]. A comparison of perforation energies of different models compared to experiment results is given in Figure 22.

$$E_c = 1.44 \times 10^9 (h_0 d_p)^{1.5} \tag{6}$$
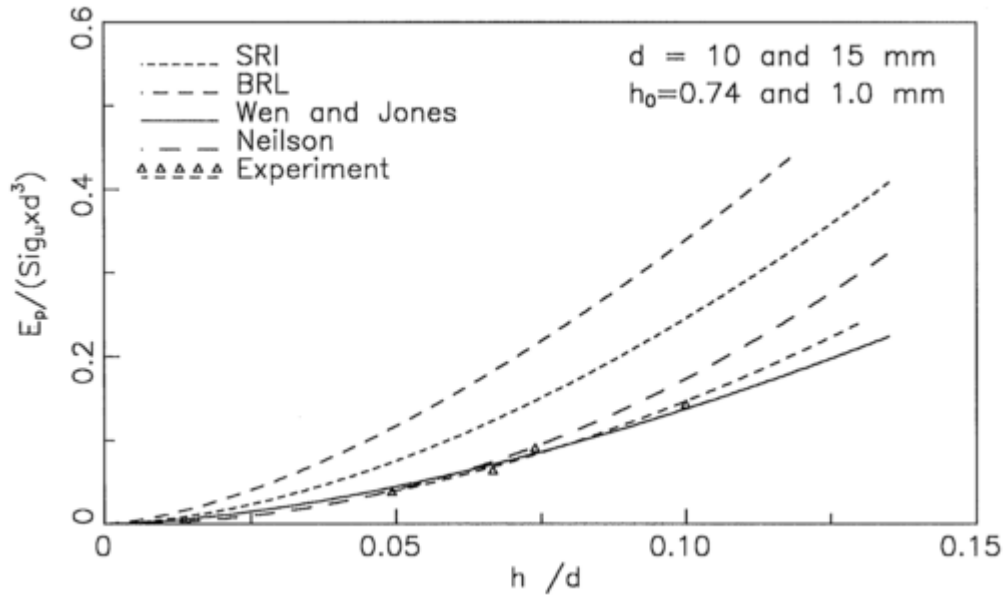
Figure 22 Comparison of Some Empirical Relations with Experimental Results [74]

Where E_p denotes the energy required for perforation of the target, Sig_u is the ultimate tensile stress (σ_u), d is projectile diameter and h is the target thickness.

3.1.4. Recht-Ipson Model (1963)

The well-known empirical model on projectile impact is the Recht-Ipson model. Recht & Ipson first considered normal impact of a cylindrical blunt nosed bar which creates the plug formation at the target zone as seen in Figure 23.

During the penetration process, together with shear resistance of the plate and kinetic energy gain of ejected plug reduce the initial kinetic energy of the projectile. Their assumptions are that friction between interacting surfaces is neglected, no global bending of the target and no deformation of the projectile are taken into account. However, in many cases high speed impact results in considerable plastic deformations on impactor and target bending. Recht & Ipson considered the target material as elastic-plastic material. If both projectile and target are regarded as perfectly plastic, the ultimate velocity of the bullet and ejected plug should be the same when momentum transfer is considered [30]. Considering the main assumption of Recht-Ipson model, it is well applicable for thin targets. Recht-Ipson model estimates projectile exit velocity V_f in terms of the initial velocity V, the projectile mass m_p and the ejected plug mass m_e as given in Eq.(7).

$$V_f = \frac{m_p}{m_p + m_e} V \qquad (7)$$

Eq.(8) expresses the loss of projectile kinetic energy E_{fn} that is spent to deform the target plastically plus the heat generated at the impact zone.

$$E_{fn} = \frac{1}{2}\left[\frac{m_e}{m_p + m_e}\right] m_p V^2 \qquad (8)$$

One can express residual velocity in terms of initially known quantities.

$$V_r = \left[\frac{m_e}{m_p + m_e}\right](V^2 - V_x^2)^{1/2} \qquad (9)$$

Where V_x term denotes the critical velocity of the projectile, below which the plug ejection will not be occur. In other words, V_x is the maximum projectile velocity at which the target stops the projectile without being perforated. As discussed, in different words, previously this critical velocity is called as ballistic velocity limit of the target. Obviously when the residual velocity equals to zero in Eq.(9), the rest of the equation yields to ballistic limit velocity [31]. It can be easily detected that when the impact velocity equals to ballistic limit velocity as seen in Eq.(10).

$$V = V_{bl} = V_{50} = V_x \leftrightarrow V_r = 0 \qquad (10)$$

On the other hand, for much lower or higher velocities we can deduce the following set of relations given in Eq.(11).
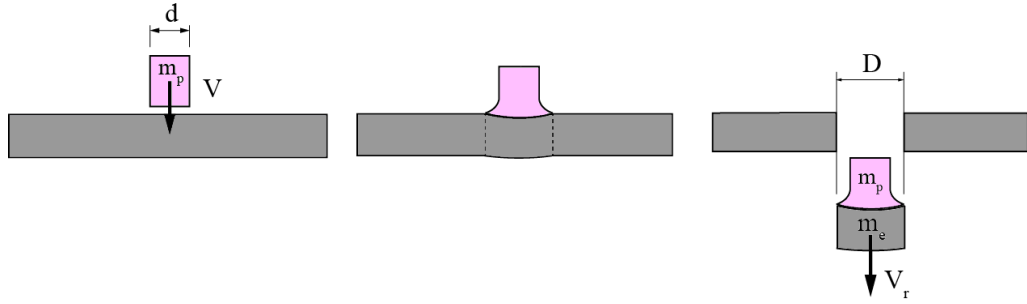
Figure 23 Recht-Ipson Normal Impact Model [30]

$$V < V_{50} \leftrightarrow V_r = 0$$
$$\qquad\qquad\qquad\qquad\qquad (11)$$
$$V > V_{50} \leftrightarrow V_r > 0$$

For oblique impact cases Recht-Ipson model should include the change in the angle of obliquity term β as well (Eq.(12)). An oblique impact case illustrated in Figure 24 by Recht & Ipson.

$$V_r = \frac{cos\beta(V^2 - V_x^2)^{1/2}}{1 + \frac{m_e}{m_p}} \quad (12)$$
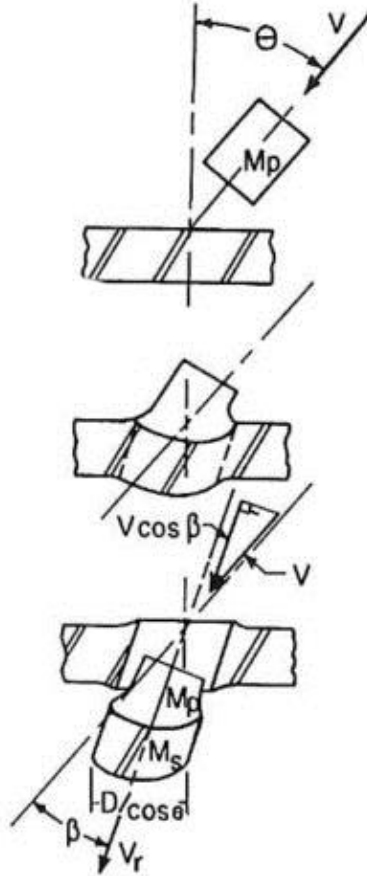
Figure 24 Recht-Ipson Oblique Impact Model [30]

3.1.5. Lambert-Jonas Model (1976)

Recht-Ipson model best suits with rather thin materials. Additionally, projectile deformation, frictional-restitutional losses and the global plastic bending are not included in the model [64]. However, during the high-speed penetration, some

degree of plastic deformation is inevitable for many cases. Residual velocity of the projectile cannot be calculated with adequate consistency especially for impact of thicker plates, multi-layer targets and long rod penetrator cases [75]. Recht and Ipson expressed the relation which estimates the residual velocity of the projectile after completely piecing the target plate. The residual velocity of the projectile can be calculated by the following relationship (Eq.(13)). Where V_{bl} denotes the ballistic limit velocity of the projectile for a target plate.

$$V_r = a\left(V^p - V_{bl}^p\right)^{1/p} \quad , V > V_{bl}$$
$$V_r = 0 \quad , 0 \leq V \leq V_{bl}$$

(13)

where the constants are defined as $0 \leq a \leq 1$ and $p > 1$.

$$a = \frac{m_p}{m_p + m'/3}$$

(14)

In Eq.(14), m' denotes the amount of the target material to be ejected by the projectile.

Recht and Ipson defined the constant p through the Eq.(15).

$$p = 2 + \frac{z}{3} \; ; \; z = \frac{t}{d} sec^{0.75}\beta$$

(15)

where;

- β is the change in the angle of obliquity during perforation, take it as zero for normal impact case
- d is projectile diameter
- t is target thickness.

One can easily see that the Lambert-Jonas Model is almost no different than the Recht-Ipson Model except the value of the parameter p. This parameter is taken as $p = 2$ in Recht-Ipson model with a rough estimation [76].

3.1.6. Three Stage Model of Awerbuch & Bodner (1974)

Awerbuch and Bodner [77] started the analysis of impactor penetration into an intermediate-thick target from writing out the equation of motion of the process. The simplest differential form of the projectile motion is given in Eq.(16).

$$\frac{d}{dt}(mV) = -F \qquad (16)$$

Where F is, the resultant force acting on the projectile, m is the mass of the projectile, V is the velocity of the projectile. F is the resultant of target inertial force, contact force, and force created by shear deformation. Awerbuch et al. did not consider the elastic and plastic stress waves propagated in the both medium along with the bending of the target.
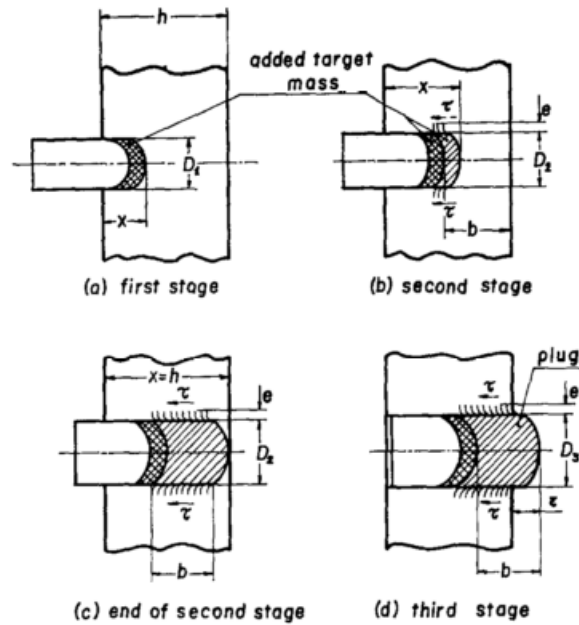
Figure 25 Three Stages of Perforation [77]

In the early stages of the hard object penetration, the target plate applies only compressive and inertial forces to the penetrator since the only deformation is elastic in this stage. In the first stage plastic deformations are neglected as can be seen in Figure 25. Force equilibrium in the early stage of the penetration can be expressed as in Eq.(17).

$$\frac{d}{dt}(mV) = V\frac{dm}{dt} + m\frac{dV}{dt} = F_1 = -\frac{1}{2}\varphi\rho A_1 V^2 - \sigma_c A_1 \qquad (17)$$

Where φ is projectile nose type parameter to be taken as unity for blunt noses, 0.5 for spherical noses and $sin^2\alpha$ for conical noses $(\alpha: nose\ apex\ angle)$ and A_1 is the cross-sectional area of the hole in the target which may equal to mushroomed nose area of the projectile in later stages. However, for the early stages it can be equated to the cross-sectional area of the projectile.
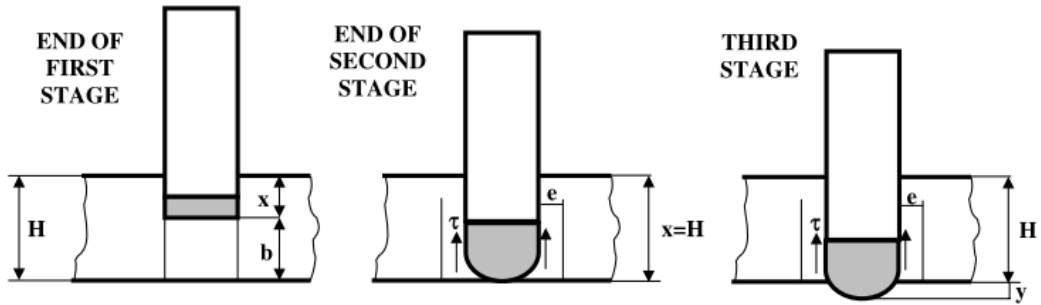
Figure 26 Basic Dimensions of Awerbuch's et al. Three-Stage Penetration Model [66]

During the penetration, softer projectiles erode by the distance travelled in the target plate. So, time change of the mass of the projectile as described in Eq.(18) should be inserted in the equation as well.

$$\frac{dm}{dt} = \rho A_1 \frac{dx}{dt} = \rho A_1 V \tag{18}$$

Inserting to Eq.(17) and solving for the velocity, the projectile velocity $V_1(x)$ can be expressed as Eq.(19).

$$V_1(x) = \left\{ \left[V^2 + \frac{\sigma_c}{\rho(1 + 0.5\varphi)} \right] \left(\frac{m_0/\rho A_1}{m_0/\rho A_1 + x} \right)^{2+\varphi} - \frac{\sigma_c}{\rho(1 + 0.5\varphi)} \right\}^{0.5} \tag{19}$$

The parameters σ_c is ultimate compressive stress of the target, ρ is the target density and x is the distance projectile travelled in the target.

A plugging formation can be observed in the subsequent stage. In this stage target inertial forces still play an active role. Additionally, plastic shearing deformation with frictional effects also starts to take place. The resultant shear stress given in the Eq.(20) can be in the form of summation of shear stress and the frictional contribution of shear strain rate.

$$\tau = \tau_0 + \mu \dot{\gamma} \tag{20}$$

Where μ denotes the coefficient of friction and $\dot{\gamma}$ is the shear strain rate. The projectile velocity at the second stage is expressed in Eq.(21).

$$\frac{dV_2(x)}{dx} = \frac{\left[\begin{array}{c} -(1 + 0.5\varphi)\rho A_2 V^2 - \tau_0 \pi D_2 x - \frac{\mu \pi D_2}{e} V x + \cdots \\ \cdots + \frac{\mu \pi D_2 (h-b)}{e} V + \tau_0 \pi D_2 (h - b) - \sigma_c A_2 \left\{ 1 - \left[\frac{x-h+b}{b} \right]^2 \right\} \end{array} \right]}{(m_0 + \rho A_2 x) V} \tag{21}$$

Where D_2 is the cylindrical cavity diameter, A_2 is the cross-sectional area (perpendicular to the cavity axis) of the cylindrical cavity formed in the material. x, h, b and e are the geometrical quantities as explained in the Figure 25.

Last stage of the penetration is completed by piercing of the target. At this stage, a bulk of material in front of the projectile is accelerated with the projectile. When the maximum shear strain is achieved in the target material, complete failure occurs at

the perimeter area of the plug formation, beyond this time on no resisting force remains (after the stage-3 in Figure 26).

3.1.7. Woodward and de Morton's Energy-Deformation Model (1976)

Woodward and de Morton [78] constructed their model on two basic principles by taking the blunt nose projectile into account. The two principles are deformation propagation of target material and the law of conservation of energy. They also investigated motion of deformed zone and utilized conservation of energy method in an effort to estimate velocity of the projectile [66]. As the projectile hits the target, a compressive stress wave is propagated in the material. Woodward et al. [78] expressed the velocity of the deforming region in terms of strain in the material as given in Eq.(22).

$$V = \frac{\kappa \sigma_y}{\rho C_e} + \frac{2}{n+1} \sqrt{\frac{\kappa \sigma_0 n}{\rho}} \left[\varepsilon^{\frac{n+1}{2}} - \left(\frac{\kappa \sigma_y}{E} \right)^{\frac{n+1}{2}} \right] \qquad (22)$$

Where ε is strain, σ_y is the yield stress, E is Young's modulus, $C_e = \sqrt{\frac{E}{\rho}}$ is the elastic stress wave velocity, $\kappa > 1$ is a parameter of constrained deformation, σ_0 and n are material parameters conforming to strain hardening behavior of the subject material.
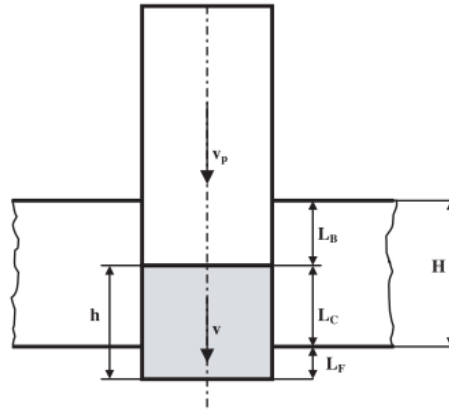
Figure 27 Basic Dimensions of Energy Deformation Model [66]

Energy-deformation model is considered only for flat nose projectiles which cause considerable amount of ejected plug mass as seen in Figure 27. Besides, this model can only be applicable to intermediate or thick targets having low to moderate strength.

3.1.8. Woodward's Structural Model (1987)

Woodward [79] developed a structural model by considering local deformations such as plugging deformation, bending of the plate and stretching during penetration of a blunt nose rigid projectile. If an impactor has sufficiently high kinetic energy, it creates plastic hinges in the target. The position of the plastic hinge can be determined through solving angular and linear momentum equations.

Woodward divided the problem in two stages. In the first stage plug formation occurs and accelerates to the same velocity with the projectile. During this stage, elastic wave interactions are neglected to decrease complexity of the problem. Immediately after the touch, plug gains the velocity V_p and the projectile velocity reduces to V_p and they move together. Using conservation of momentum law, one

can determine the common velocity V_p by considering the impacting mass and plug masses. As the two bodies interact the target plate deforms under the rotation about a plastic hinge. The position of the hinge $z(t)$ is time dependent and changes at every time increment (Figure 28 and Figure 29).

Any change in angular momentum equals to the impulse of the torque (Eq.(23)).

$$-mV_0z + mV_pz + \frac{1}{2}m_0R^2V_pz + \frac{1}{3}m_0z^2V\left(R + \frac{1}{4}z\right) = -2\int_0^t (M_{p0} + M_{pz})dt \quad (23)$$

Where m is projectile mass, z is the hinge distance, R is the projectile radius, V_0 is projectile impact velocity, V_p is plug velocity, V is velocity of the plate near the plug and $m_o = 2\pi\rho h_0$

Shear force and bending moments at plastic hinges can be evaluated from the following set of equations (Eq.(24)).

$$F_s = \frac{\pi}{\sqrt{3}}\sigma_y Rh \qquad M_{p0} = \frac{\pi}{4}\sigma_y Rh^2 \qquad M_{pz} = \frac{\pi}{4}\sigma_y(R + z)h_0^2 \quad (24)$$

In the above equation F_s is the shear force, M_{p0} is plastic hinge moment around the projectile and M_{pz} denotes the plastic hinge moment travelling from impact zone to distant zones.
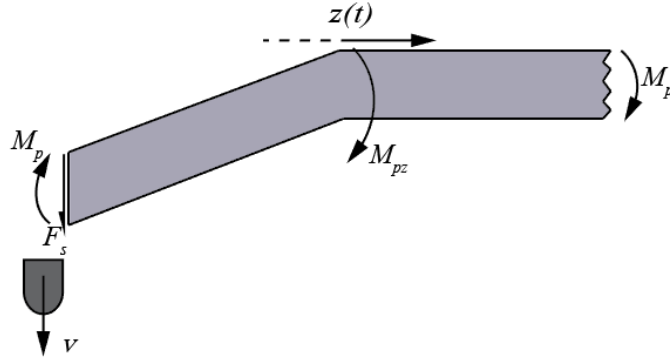
Figure 28 Free Body Diagram of a Target Being Pierced by a Projectile [79]

At the subsequent stage, since the plug is completely cut from the plate, no sliding force remains between the plate and the plug. However, the plate is stretched and bent at the hinge locations (Figure 29). When the plastic strain reaches a critical value, it will no longer withstand the load anymore. The failure type depends on the loading case and the material type. The details are given in [79] .

Conservation of angular momentum in the second stage yields to, Eq.(25),

$$\frac{1}{2}mz\Delta V cos\theta + \frac{1}{4}m_0 R^2 z\Delta V cos\theta + \frac{1}{6}m_0 z^2 \left(R + \frac{1}{4}z\right)\Delta V cos\theta = -(M_p' + F_p z sin\theta)\Delta t \quad (25)$$

Conservation of linear momentum in the second stage yields to, Eq.(26),

$$m\Delta V + \frac{1}{2}m_0 R^2 \Delta V + \frac{1}{2}m_0 z \left(R + \frac{1}{3}z\right)\Delta V + m_0 \left(R + \frac{2}{3}z\right)V\Delta z = 0 \quad (26)$$

where

Δt is time change, Δv is the velocity change, Δz is the hinge location change

h_0 is the initial plate thickness, h is the reduced section thickness

F_p is membrane stretching force $F_p = \pi\sigma_y Rh$, θ is plate bent angle

M_{pz} is the plastic moment

M_p' is the reduced moment which can be expressed as $M_{pz}' = M_{pz}(1 - \left(\frac{Rh}{(R+z)h_0}\right)^2)$
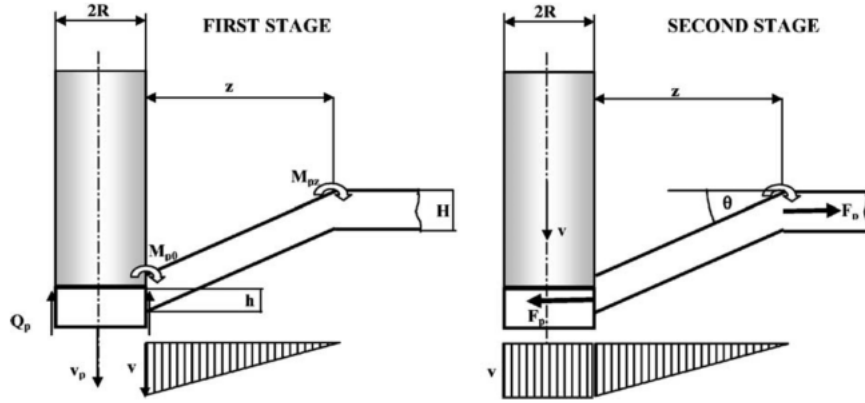
Figure 29 Representation of Two-Stage (Structural Model) [80]

3.1.9. Phenomenological Model of Liss et al. (1983)

Liss et al. [81] assumed a rigid penetrator having blunt nose hits a target which is made of ductile metal as schematically shown in Figure 30. In their work, only the normal impact is considered. Plug formation and thinning of plug section have been considered.
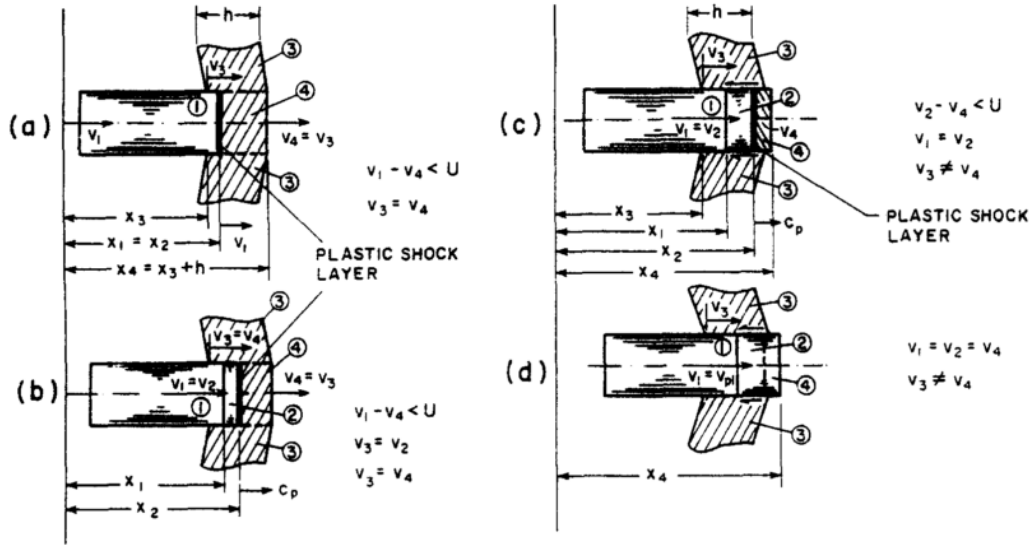
Figure 30 Phenomenological Model of Liss et al.[81]

Velocity of the projectile will be reduced to the V_1 which is equal to the reduced velocity of the plastic zone at the last stage of the impact. This plastic zone starts from the impact end of the projectile and grows until the plastic work done on either part will be sufficient for perforation.

$$\sigma = \frac{1}{1-\varepsilon}[\sigma_y - Bln(1-\varepsilon)] \qquad \tau = \tau_y - \frac{1}{3}B\gamma \qquad (27)$$

Where B is the material strength parameter, σ_y and τ_y are normal and shear yield strength of material, ε and γ are engineering strain and shear strain.

Liss et al. proposed an analytical expression given in Eq.(28) of compressive plastic wave propagation speed C_p in terms of strain.

$$C_p = \frac{V_1 - V_4}{\varepsilon} + V_4 \qquad \varepsilon(\sigma_c - \sigma_y) = \rho(V_1 - V_4)^2 \qquad (28)$$

σ_c and σ_y are uniaxial constrained stress in the plate and compressive yield stress of the target material respectively.

As the bending part and plug part of the plate have different velocities commence of the first stage ends and the second stage starts.

Eq.(29) expresses the acceleration of the plug as depicted in Figure 30.

$$\dot{V}_1 = -\frac{\sigma_c A + \rho A (V_1 - V_4)^2 + 2\pi R \tau_q (x_2 - x_1)}{m + \rho A (x_2 - x_1)} \qquad V_1 = V_2 \qquad (29)$$

where A is projectile diameter, x is axial displacement, R is plastic hinge radius and τ_q is dynamic peripheral shear stress.

The model developed by Liss et al [81] used a nondeformable penetrator model and a rigid-plastic target under normal impact scenario. They constructed their model on plastic wave theory.

Liss and Goldsmith [82] revised this model for the deformable penetrator with linear hardening material assumption as seen in Figure 31. The final velocity of the projectile is determined through the Eq.(30). As one can see from the Eq.(30), the final velocity in this revised model depends on the material properties of both elements. The impact stages are clearly depicted in Figure 32.
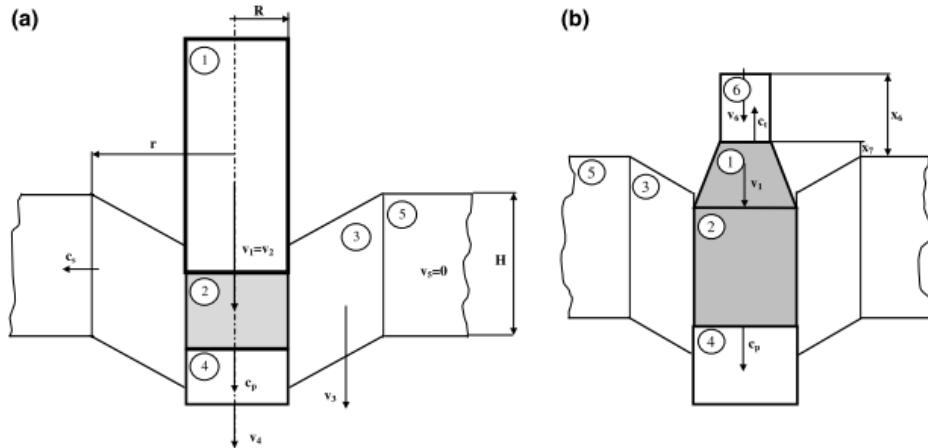
Figure 31 Comparison of Phenomenological Model and Modified

Phenomenological Model [66]

$$V_1 = \frac{V_0}{1 + \frac{\rho_t C_{e_t}}{\rho_p C_{e_p}}} \tag{30}$$

where subscripts t and p represent the target and projectile respectively, ρ is the material density, C_e denotes the speed of sound in the material defined as $C_e = \sqrt{E/\rho}$.
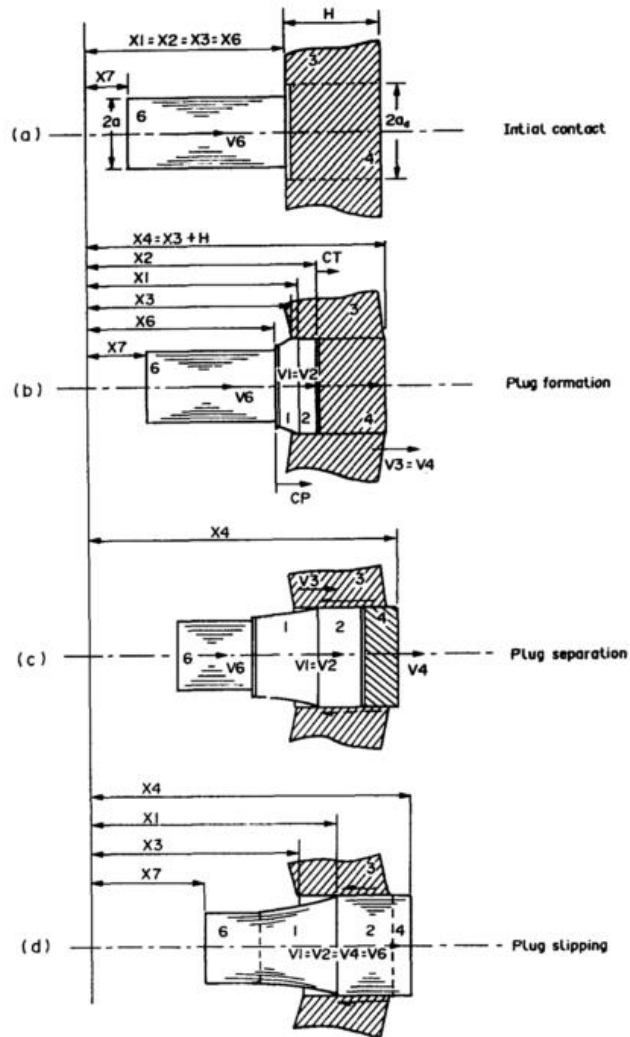
Figure 32 Dimensions in Modified Phenomenological Model [82]

3.1.10. Dynamic Cavity Expansion Model of Luk & Forrestal (1988-1991)

Forrestal and Luk [83] developed an analytical dynamic model for compressible elastic-plastic solid. The model describes the elastic and plastic response of the material on dynamic spherical cavity expansion by assuming a spherically

symmetric cavity is formed at a constant speed in the material that has initially no hole.

The pressure required to open a spherical hole from zero initial radius in the target under the constant cavity expansion velocity V by assuming quasi-static response of the compressible elastic-plastic material is given as in the Eq.(31).
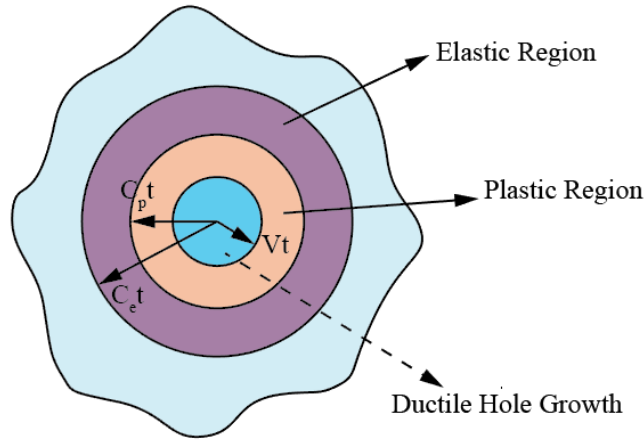
Figure 33 Ductile Hole Enlargement Mechanism with Elastic and Plastic Stress Zones

$$\sigma_s = \frac{2\sigma_y}{2}\left\{1 + ln\left[\frac{E}{3\sigma_y(1-v)}\right]\right\} \qquad (31)$$

In this equation, σ_s denotes the finite pressure required to form a hole on the cavity wall.

Both radial and circumferential stresses act on the material during the cavity expanding process. In the elastic zone, by using Hooke's Law, stress-displacement relations are evaluated in the following set of equations (Eq.(32)).

$$\sigma_r = -\frac{E}{(1+v)(1-2v)}\left[(1-v)\frac{\partial u}{\partial r} + 2v\frac{u}{r}\right] \qquad (32)$$

$$\sigma_\theta = -\frac{E}{(1+v)(1-2v)}\left(v\frac{\partial u}{\partial r} + \frac{u}{r}\right)$$

In the plastic region, the response of the compressible material against deformations is assumed to be linear and Tresca yield criterion is valid. Then the yield stress can be calculated in terms of radial and tangential stresses (Eq.(33)).

$$\sigma_r - \sigma_\theta = \sigma_y \tag{33}$$

By using the conservation of momentum and mass laws, radial stress at cavity wall is evaluated. The radial stress in the elastic-plastic region for homogenously growing cavity problem is described by the Eq.(34).

$$\sigma_r = \frac{2}{3}\sigma_y\left[1 + ln(\frac{2E}{3\sigma_y})\right] + \frac{3}{2}\rho V^2 \tag{34}$$

3.1.11. Chen-Li Model (2003)

Chen and Li [84], [85], [86] considered the perforation of plates by rigid projectiles. Two main perforation mechanisms play a dominant role. Perforation begins with ductile hole enlargement process and ends with the plug ejection. In their model, sharp nose projectile is also considered. The residual velocity of the projectile is bounded to incidence velocity, ballistic limit velocity, the nose shape and plate thickness to projectile diameter ratio. The residual velocity of the projectile can be calculated by Eq.(35).

$$V_r = \left\{\frac{\left(V_0^2 - V_{bl}^2\right)}{exp(\frac{\pi\chi}{2N})}\right\}^{0.5} \tag{35}$$

Where N is the characteristic nose geometry function of the projectile and χ is the plate thickness to projectile diameter ratio.

In the case of blunt projectile the model reduces to Recht-Ipson Model [87].

Same authors [88] proposed another model (Eq.(36)) for oblique perforation of thick plates.

$$V_r = \sqrt{\frac{(V_0^2 - V_1^2)\cos^2\delta}{\exp[\pi\chi sec(\beta + \delta)/2N]}} \tag{36}$$

Where β is the angle of obliquity and δ is the change in obliquity of the projectile just after the penetration.

3.1.12. Forrestal-Warren Model (2009)

Forrestal & Warren [89] developed equations for perforation of aluminum targets by normal impact of rigid conical and rigid ogival nose projectiles. From the experimental results, they seen that projectiles having high strength undergoes limited or no deformation during the penetration. Furthermore, aluminum plates represent ductile hole enlargement type failure during the process. They assumed the material as elastic-plastic behavior. In this approach target inertia effect is neglected.

Residual velocity is calculated using Eq.(37) for conical nose rigid projectile

$$V_r = \sqrt{V_0^2 - V_{bl}^2}\, exp\left[-\frac{h}{\left(L + \frac{l}{3}\right)}\frac{\rho_t}{\rho_p}B_0\,tan^2\,\emptyset\right] \tag{37}$$

Where h is the thickness of target plate, $\emptyset$ is the nose angle, B_0 is the dimensionless constant obtained from curve fitting, L and l are dimensional constraints of projectile.

Residual velocity is calculated using Eq.(38) for rigid ogival nose projectile.

$$V_r = \sqrt{V_0^2 - V_{bl}^2}\, exp\left[-\frac{h}{(L + k_1 l)}\frac{\rho_t}{\rho_p}B_0 N(\psi)\right] \tag{38}$$

where $k_1, N(\psi)$ are functions developed for the geometry of nose type (Figure 34).
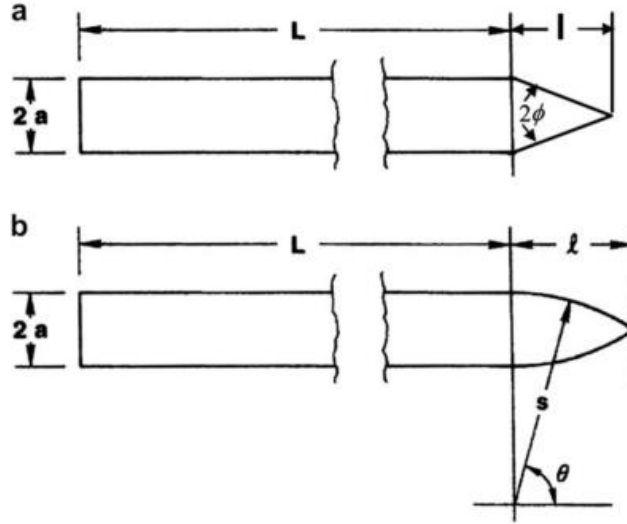
Figure 34 Projectile Geometries Used by Forrestal & Warren [89]

3.1.13. Marom and Bodner's Multilayer Penetration Model (1979)

Marom & Bodner [62] constructed a multilayer perforation model on Recht-Ipson model and dynamic beam bending theory. They proposed this model for aluminum beams of thin layers and carried out experimental studies along with the numerical study.

Recht-Ipson model has discussed energy balance method for a single layer target. The residual velocity of the projectile can be calculated numerically by using the Eq.(39).

$$V_r = \sqrt{\frac{V_0^2 - V_{bl}^2}{\left(1 + \frac{m_e}{m_p}\right)\left(p + q\frac{m_e}{m_p}\right)}} \tag{39}$$

61

where m_e is mass of ejected material, m_p is mass of projectile without loss, p post to pre-impact projectile mass ratio, q is the ratio of plug mass moving with the projectile to total plug mass.

When the target is layered, and configured as in contact and being hit by an impactor, subsequent layers will apply additional resistance to perforation and plug movement. Hence the residual velocity of the projectile is expressed in Eq.(40).

$$V_r = \sqrt{\frac{V_0^2 - V_{bl}^2}{\left(1 + \frac{m_e}{m_p}\right)^2} - \frac{\sigma_{uc}\pi d^2 h}{2(m_p + m_e)}} \tag{40}$$

In Eq.(40), h denotes target thickness, d denotes the projectile diameter.

3.1.14. Penetration Model for Multilayer Targets of Liaghat et al. (2005)

Liaghat et al. [90] proposed an analytical model for multilayer metallic targets assuming rigid-conical projectile impact. They derived some empirical relations on the works done during penetration of a target. Also, they assumed that when the yield stress is achieved the material is assumed to fail and target impact zone thickness remains the same. Residual velocity of a projectile after piercing the contacting n-layered plates is calculated by energy balance method, Eq.(41).

$$V_{r_{n-1}} = \sqrt{V_i - \frac{2W_n}{m}} \qquad\qquad W_n = W_{b_n} + W_{p_n} + W_{d_n} \tag{41}$$

Total work is the sum of W_{b_n} bending work, W_{p_n} work spent to plastic deformation and W_{d_n} dynamic work at n number of layers.

Bending work of two-contacting plates is given as Eq.(42).

$$W_b = M_p \theta_r \tag{42}$$

Plastic moment in bending

$$M_p = \frac{z_1 h_1^2}{4} \sigma_{y_1} + \frac{z_2 h_2^2}{4} \sigma_{y_2} + \frac{\pi}{3} h_1 h_2^2 \sigma_{y_2} \tag{43}$$

Local deformations after perforation creates petal formation. Liaghat et al. assumed that a homogeneous petal formed around the hole after perforation.

$$\theta_r = \frac{\pi}{2} + 2 \int_{-\pi/2}^{\pi/2} \frac{sin\emptyset cos\emptyset}{cos[sin^{-1}(sin\emptyset cos\delta)]} d\delta \tag{44}$$

Work spent for bending of an n-layer spaced target can be shown in summation form (Eq.(45)).

$$W_b = \sum_{i=1}^{n} \frac{z_i h_i^2}{4} \sigma_{y_i} \theta_r \tag{45}$$

A very similar model for contacting and spaced armor systems is offered by Liang et al. [91]. They modeled two and three-layered armor structures which are separated or in contact configuration at normal impact. Main differences between the two models were Liang et al. neglected plate bending, dishing and petal formation but elastic wave speed is included in their model.

3.2. Comparison of Some Analytical Models

Table 6 A Comparison Chart for Mentioned Analytical Models of Projectile Penetration into Metal Targets

Analytical Model	Year Proposed	Velocity Range (m/s)	Impact Orientation	Target Material	Target Parameters	Remarks
De Marre [73]	1886	V < 900	Normal	Ductile Steel	-	Blunt nose projectile
SRI/m-SRI (Neilson) [73], [74]	1963	100 < V < 250	Normal	Ductile Steel	1-10 mm thick	Blunt/Hemispherical nose projectile
BRL[8]	1968	V < 270	Normal	Ductile Steel	$315 < \sigma_u < 500$ MPa	Blunt nose projectile
Recht-Ipson [30], [31]	1963	$V \sim V_{50}$	Normal/Oblique	Steel-Aluminum	Medium thickness	Projectile erosion and global bending neglected, deformable projectile assumed. Cons. of momentum, energy balance principles are used
Lambert-Jonas [75]	1976	$V \sim V_{50}$	Normal	Steel-Aluminum	Medium thickness	Constant energy absorbed by target assumed
Awerbuch-Bodner [77]	1974	$V \sim 400$	Normal	Metallic plates	Thick plates	Blunt, hemispherical, conical nose Frictional loss included
Woodward-de Morton [78]	1976	-	Normal	Aluminum	Intermediate thick plates $d/h \approx 1$	Blunt nose rigid projectile Elastic-plastic stress waves Plate ending neglected
Woodward's Structural Model [79]	1987	V < 200	Normal	Metallic plates	Thin metallic plates	Bending, membrane stretching deformations on target plate are assumed Rigid projectile
Phenomenological Model [81]	1983	V < 900	Normal	Aluminum	Thin-Intermediate thickness	Rigid & Deformable blunt projectile are considered Plastic wave theory is used
Dynamic Cavity Expansion Model [83], [92]	1991	V < 900	Normal/Oblique	Compressible & Incompressible Materials	-	Elastic-plastic stress waves are considered
Chen-Li [84]–[86]	2003	V < 900	Normal/Oblique	Metallic plates	Thick plates	Rigid projectile assumption Nose geometry is an important parameter
Forrestal-Warren [89]	2009	V < 1500	Normal	Steel-Aluminum	Thick & thin plates	Rigid conical and hemispherical projectiles Ductile hole enlargement is suggested
Marom-Bodner Multilayer Model [62]	1979	$375 \sim 1000$	Normal	Aluminum	Thin layers	Thin layers, spaced and in contact arrangement
Liaghat's Multilayer Model [90]	2005	V < 700	Normal/Oblique	Steel-Aluminum-Polycarbonate	Thin layers	Spaced and in contact arrangement Rigid conical nose projectile During penetration velocity vector remains unchanged

CHAPTER 4

MATERIAL MODELS

Materials represent very different behavior under dynamic loading cases comparing to static loading response. At high strain rates, the particle velocity and the stress vary a lot from point to point due to the propagation of elastic stress and plastic waves. Shock loads cause stress interactions in the material [56], [93]. Moreover, materials show additional resistance against high strain rate deformations due to inertia [94] and thus, some of elastic-plastic work done on the material converted into heat production.

Under quasi-static loading, heating and the heat diffusion by conduction are balanced. However, since the time duration of the deformation is very short in high strain rate loadings, the material does not have enough time to dissipate much of the generated heat. Heat production at high loading rates cause local temperature rise. Local temperature rise becomes more effective in high rate loadings and it impairs the material strength called as the thermal softening.

4.1. Material Characterization Methods

Material characterization is an important stage before the simulations of high strain rate deformations. A material subjected to large deformations gives unique stress-strain relationship against any high rate deformations. On the other hand, damage initiation and the damage evolution phenomena with the observable failure modes of the material should be known beforehand. The mathematical relation which

relates the yield strength, strain, strain rate, temperature related physical properties affects the equivalent plastic stress. Mathematical description of the material which can describe the dynamic behavior of the material is called the constitutive model [95].

A typical constitutive model can be written in the form of Eq.(46).

$$\sigma_{eq} = \sigma(\varepsilon, \dot{\varepsilon}, T) \tag{46}$$

4.1.1. Quasi-Static Uniaxial Tension Tests

Strain rates below $\dot{\varepsilon} = 10^{-3}$ s^{-1} are accepted as quasi-static deformations and test methods of this level deformations are standardized by ASTM and performed by standard tensile testing machines [96]. Higher rate of deformations need more specialized machines to obtain a meaningful result. These machines and corresponding rating of deformations are tabulated in Table 7.

Contrary to quasi-static loadings, deformations above quasi-static mode to below the strain rates of $\dot{\varepsilon} = 10^{3}$ s^{-1} are called as high strain rate deformations and requires specialized machines to perform reliable tests. Ramesh [94] reports that beyond the $\dot{\varepsilon} = 10^{3}$ s^{-1} more specific methods should be utilized due to increasing strain rate exceed machine capability.

Quasi-mode deformation tests are performed by servo controlled hydraulic tensile test machines. This type of machines can conduct experiments up to $\dot{\varepsilon} = 10^{-2}$s^{-1}.

Higher rate material properties require the equipment that can measure the higher rates of deformations. High speed deformations which correspond to strain rate from $\dot{\varepsilon} = 10^{2}$ s^{-1} to $\dot{\varepsilon} = 10^{4}$ s^{-1} can be measured by Kolsky and Split Hopkinson Pressure Bar method respectively.

Table 7 Conventional Material Test Methods at Various Strain Rates [94]

Strain Rate (s^{-1})	Method
10^{-6}	Servo-hydraulic Machines
10^{-4}	
10^{-2}	
10^{0}	Specialized Machines
10^{2}	Kolsky Methods
10^{4}	Miniaturized Kolsky Bar
10^{6}	Pressure-Shear Plate Impact
10^{8}	

4.1.2. Split-Hopkinson Pressure (Kolsky) Bar

Split-Hopkinson Pressure Bar (SHPB) is used to determine material properties at high strain rates in the range of $\dot{\varepsilon} = 10^2 \sim 10^4$ s^{-1}. SHPB and Kolsky use almost the same principle and the method is named as either of them. However, while SHPB method only used for compression experiments, Kolsky method is used for tension, torsion and even compression experiments [97]. A principal model of SHPB (Kolsky) test setup is presented in Figure 35.

If the part is too small to produce standard tensile test specimen then such cases, Kolsky Bar test method may become the only method to evaluate the material properties at high rate deformations.
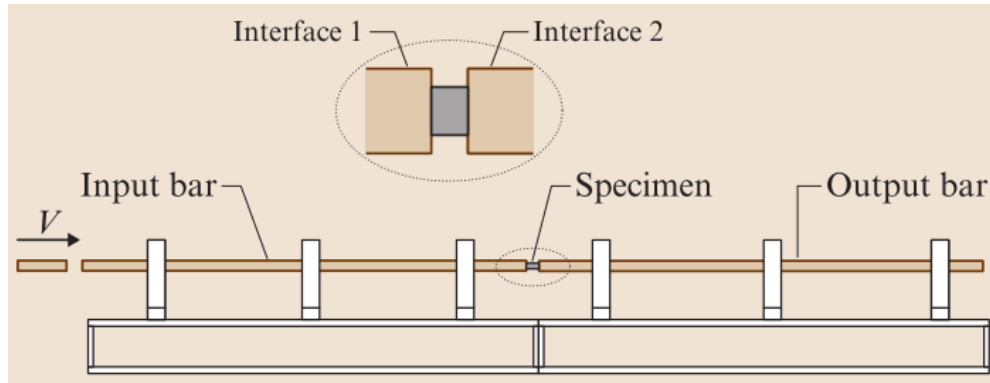
Figure 35 Kolsky Method [94]

The Kolsky compression bar test design consists of an input and an output bar which will go only elastic deformations during the test. The input and output bars are attached to each other at the ends by interfacing of the specimen as shown in Figure 35. A striker bar hits at the free end of the input bar. As it hits the input bar two compressive stress waves generated and starts to propagate in opposite directions. The elastic stress waves moving in the input bar reaches to the specimen again two stress waves are generated; First one is the reflection into the input bar and the second one is the transmitted into the specimen and afterwards into output bar as shown in Figure 36. These elastic compressive stress waves moving in input and output bars are measured by strain gages glued on the bars. The strain gage locations and the stress interactions are illustrated in Figure 36.
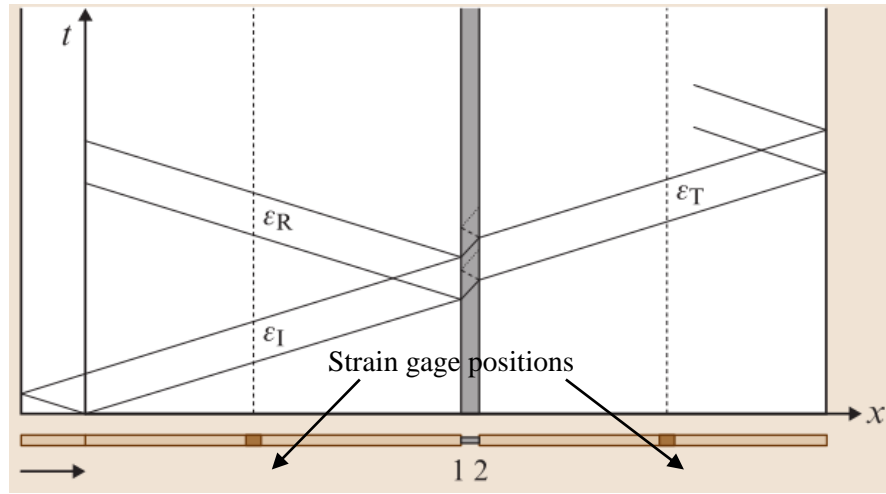
Figure 36 Wave Propagation in Kolsky Method [94]

Important parameters for Kolsky Compression Bar experiment design are

- Bar length to diameter ratio should be $L/D \geq 100$
- Diameter of input/output bars to specimen diameter should be $2 \leq D/d_0 \leq 4$
- Specimen length to diameter ratio should be $0.6 \leq l_0/d_0 \leq 1$

4.1.3. Taylor Cylinder Impact Test

Taylor cylinder impact test is the easiest method to determine the stress state and the dynamical properties of a specimen subjected to high rate deformations [98]. A cylindrical specimen is directly launched to hit a target which is assumed as a rigid surface, hence it should be hard enough to withstand the impact. It is possible to measure the strain rates on the order of 10^5-10^6 s^{-1} [99]. After impact of the specimen by macroscopic inspection of deformed and mushroomed shape of the specimen, material properties can be determined (Figure 37).

The flow stress of the material is traditionally calculated with quasi-static tensile test. However, the Taylor's method gives alternative approach to calculate yield strength of the material especially in the case of manufacturing of a standard test specimen is not possible. In Figure 37, the distance L_1 undergoes plastic deformation. The strain in this zone can be calculated by knowing the initial length, undeformed length, and deformed length of the specimen by utilizing the Eq.(47).
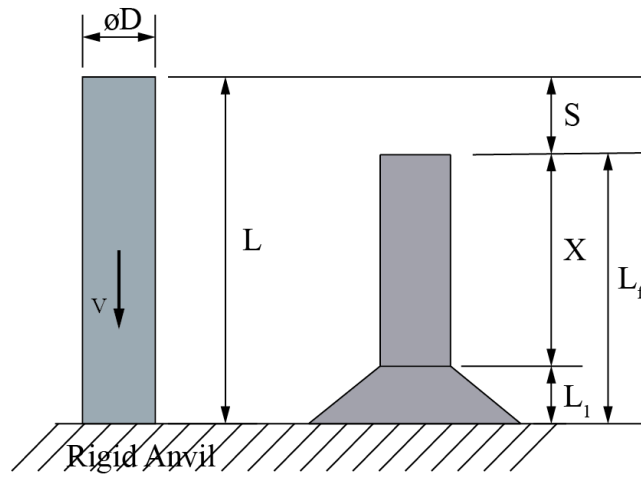
Figure 37 Taylor Impact Test

$$\epsilon = -ln(\frac{L_f - X}{L - X}) \tag{47}$$

Since, this experimental technique incorporates the strain rate dependency, we need a relation to calculate the strain rate (Eq.(48)).

$$\dot{\epsilon} = -\frac{V}{2(L - L_f)} ln \frac{(L_f - X)}{(L - X)} \tag{48}$$

The flow stress of the subjected specimen can be calculated by Eq.(49).

$$\sigma_f = \frac{\rho V^2 (L - X)}{2(L - L_f)ln(\frac{L}{X})} \tag{49}$$

Calculation of the further parameters used for JC constitutive model can be followed from [100], [101].

4.2. Observable Failure Modes in Target Plates

The failure of the materials strongly depends on the toughness of the target material. However, target thickness and the impact velocity also affects the failure mode of the target. The interrelations between the dominant parameters are tabulated in Table 8. The main failure modes reported in the literature are;

- fragmentation due to brittle behavior,
- plugging due to shearing,
- bulging due to unconstrained plastic flow,
- dishing, tearing and petaling due to stretching.

Table 8 Target Failure Types and Comparison of Deformations at Target [102]

Failure Mode	Target Ductility	Target Thickness	Velocity Regime
Ductile hole formation	Low to Moderate	Moderate thick	Well above to the ballistic limit velocity
Plugging	Tough/Moderate Hardness	Moderate thick	Low to Moderate impact
Dishing	Ductile	Thin materials	Close to ballistic limit velocity
Petaling	Ductile	Rear Petaling/ Very Thin Front Petaling/Very Thick	Low to High impact velocity
Fragmentation	Brittle	High hardness thick targets metallic materials	High impact velocity
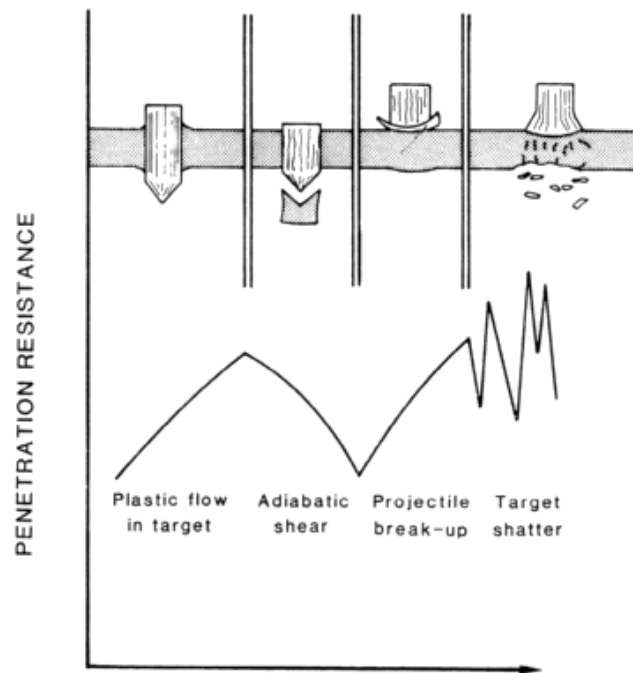
Figure 38 The Relation of The Target Hardness with Armor Resistance Against
Deforming Projectiles [103]

4.3. Equation of State (EOS)

An equation of state (EOS) defines the volumetric response of the material because
of the hydrodynamic behavior. It defines the relation between hydrostatic pressure,
density, and the internal energy [104]. EOS is strongly pressure dependent. In other
words, it is a function of impact velocity of the projectile. The significance of EOS
depends on the impact velocity. The higher the impact velocity, the higher the
pressure generated (p > 10 GPa) and the internal energy becomes significant, thus
the pressure and the volumetric strain response behaves nonlinearly. However, at
low impact velocities small pressures generated at the impact zone and the relation
between pressure and volumetric strain behaves linearly through elastic bulk
modulus [105]. Zukas et al. [106] stated that EOS has a minor importance when the

impact of any two solid bodies below 2000 m/s velocity. The scope of this thesis does not cover hyper-velocity impacts. The impact velocity regime in this thesis is well below of the hyper velocity limit.

4.4. Constitutive Strength Models

Constitutive material models represent the large strains, high rate deformations and the temperature increase caused by rapid deformations. A constitutive model for highly brittle and crack sensitive materials, such as glasses and ceramics which are under high strain rate deformations has been developed by Johnson & Holmquist [107]. This model is an updated form with significant differences of Johnson-Holmquist-Beissel (JHB) model.

There are several other efforts to express material behavior under dynamic loading cases. This work covers only metallic materials that are assumed to be isotropic material. Therefore, anisotropic constitutive relations are not considered here. However, for further information about constitutive material model one may refer to Lukyanov's report [108].

4.4.1. Johnson-Cook (JC) Constitutive Model

Equivalent von Mises stress under dynamic loading condition is proposed by Johnson & Cook [33]. The JC constitutive model (Eq.(50)) is a thermo-visco-plastic model which includes the temperature softening due to adiabatic heating and strain rate sensitivity terms. JC model fits the experimental results with a good agreement for a wide range of impact problems.

$$\sigma_{eq} = \left[A + B\varepsilon_{eq}^n\right]\left[1 + Cln\dot{\varepsilon}^*\right]\left[1 - T^{*m}\right] \qquad (50)$$

where ε_{eq} is the equivalent plastic strain,

n is the hardening exponent,

$\dot{\varepsilon}^* = \frac{\dot{\varepsilon}}{\dot{\varepsilon}_0}$ is the dimensionless plastic strain rate where $\dot{\varepsilon}_0$ is the reference strain rate,

$T^* = \frac{T - T_r}{T_m - T_r}$ is the homologous temperature, where T_r is room temperature and T_m is the melting temperature.

The material is subjected to quasi-static tensile test in order to calculate the strain rate independent terms A, B and n. Also, the subjected material tested at different elevated temperatures for temperature dependency term m.

4.4.2. Modified JC (m-JC) Model

Børvik et al. [34] proposed a modified version of JC constitutive model (Eq.(51)). They revised the JC constitutive model by replacing strain-rate sensitivity term for the sake of the conditions $\dot{\varepsilon}^* < 1$.

$$\sigma_{eq} = \left[A + B\varepsilon_{eq}^n\right]\left[1 + \dot{\varepsilon}^*\right]^C\left[1 - T^{*m}\right] \qquad (51)$$

Both the JC and the m-JC model have five distinct material constants which are A, B, C, n, and m.

Børvik et al. proposed another form (Eq.(52)) of the modified JC constitutive model coupled which includes damage status.

$$\sigma_{eq} = [1 - D]\left[A + B\varepsilon_{eq}^n\right]\left[1 + \dot{\varepsilon}^*\right]^C\left[1 - T^{*m}\right] \qquad (52)$$

Damage phenomena is first analytically defined by Johnson and Cook [109].

$$D = \sum \frac{\Delta\varepsilon_{eq}}{\varepsilon_{eq}^f} \qquad (53)$$

Eq.(53) defines the sum of the ratio of increment of equivalent plastic strain to equivalent plastic strain for fracture to occur reaches to unity. For D being equal to unity the elements of the material will no longer withstand the loads. Namely, the elements fit to this criterion will lose their stiffness.

4.4.3. Zerilli-Armstrong (ZA) Model (1997)

JC model does not include the effect of lattice structure of the materials. Zerilli & Armstrong [35] developed a different constitutive model based on metallographic structure of the materials. In some metals, multi-phase crystallographic structures can exist in the material at the same time. They developed a dislocation mechanics based model especially for FCC and BCC metals as presented in Eq.(54) [110].

$$\sigma_{eq} = C_0 + [C_1 + C_2\sqrt{\varepsilon}]ex\,p[-C_3T + C_4Tln\dot{\varepsilon}] + C_5\varepsilon^n \qquad (54)$$

Where $C_{0,1....5}$ are material constants, for FCC metals $C_1 = C_5 = 0$, for BCC metals $C_2 = 0$, n is the strain hardening parameter and T is temperature.

4.5. Failure Models

Different failure models proposed by various authors. There are two major parameters that triggers the degradation of an element in the material. Stress triaxiality and critical plastic strain will cause the damage in the material. The models such as constant fracture strain and maximum shear stress considers the failure depends on only one parameter and give a rough estimation to user.

4.5.1. Johnson-Cook Fracture Model (1985)

Johnson & Cook [109] offered a damage model for strained materials. They included the stress triaxiality, hydrostatic stress and some material parameters. Also, the model works for the materials represent different behaviors at different temperatures.

$$D = \sum \frac{\Delta \varepsilon_{eq}}{\varepsilon_{eq}^f} \tag{55}$$

In this model (Eq.(55)) fracture occurs when $D = 1$. Hence until the value of D reaches to unity the material does not lose its stiffness. The JC damage model relates the fracture strain to five distinct damage parameters stated in Eq.(56).

$$\varepsilon_f = [D_1 + D_2\, exp(D_3\sigma^*)\,][1 + \dot{\varepsilon}^*]^{D_4}[1 + D_5T^*] \tag{56}$$

Where $\sigma_{max}^* = \frac{\sigma_h}{\sigma_{eq}} = \frac{1}{3} + ln\left(1 + \frac{a}{2R}\right)$ is the maximum value that stress triaxiality ratio can take, a and R are the initial cross-section diameter and the notch diameter of the test specimen respectively, σ_h is hydrostatic stress and parameters $D_{1...5}$ are the material damage parameters.

4.5.2. Cockcroft-Latham (CL) Fracture Criterion

The CL model suggests that the material fails with fracture when the fracture energy density reaches to a specific value [111]. The CL fracture model is given in Eq.(57).

$$D_{cr} = \int_0^{\bar{\varepsilon}_f} [\![(\sigma_I, \sigma_{II}, \sigma_{III})_{max}]\!]\, d\bar{\varepsilon}_{pl} \tag{57}$$

Where $\sigma_I, \sigma_{II}, \sigma_{III}$ are principal stresses, $\bar{\varepsilon}_f$ is equivalent fracture strain, $\bar{\varepsilon}_{pl}$ is equivalent plastic strain and $\sigma_i = [\![(\sigma_{I}, \sigma_{II}, \sigma_{III})_{max}]\!] = \begin{pmatrix} \sigma_i \ if \ \sigma_i > 0 \\ 0 \ if \ \sigma_i \leq 0 \end{pmatrix}$.

Cockcroft & Latham modified their model with a normalized version. A normalized version of CL model with equivalent stress is given in Eq.(58).

$$D_{cr} = \int_0^{\bar{\varepsilon}_f} \frac{[\![(\sigma_{I}, \sigma_{II}, \sigma_{III})_{max}]\!]}{\sigma_{eq}} d\bar{\varepsilon}_{pl} \tag{58}$$

The CL model depends on only one parameter to calibrate the fracture model. Thus, this model allows one to select different calibration methods such as tension, compression, or shear tests.

4.5.3. Bao-Wierzbicki (BW) Fracture Criterion (2004)

This fracture criterion claims that as the stress triaxiality term reaches to the critical value $-\frac{1}{3}$, fracture will occur [112]. Damage D fracture model is presented in Eq.(59).

$$D = \int_0^{\bar{\varepsilon}_{pl}} \frac{1}{f(\frac{\sigma_h}{\bar{\sigma}})} d\bar{\varepsilon}_{pl} \tag{59}$$

where weighting function $f(\frac{\sigma_h}{\bar{\sigma}})$ is a function of stress triaxiality and highly depends on the material type [113].

BW model is valid for ductile materials. The failure of the material can be dominated either void growth or shear decohesion. In other words, single parameter for identifying the fracture of the material could be insufficient for different loading cases. BW model deals with the fracture behavior of ductile metals under tension as well as compression loading. Figure 39 illustrates how the loading case effects the fracture strain.
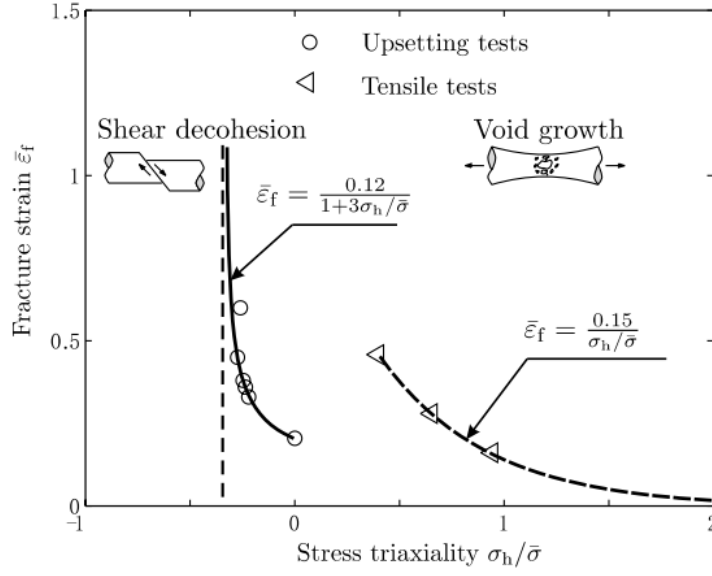
Figure 39 Critical Fracture Strains in Different Loading Cases for 2024-T351
Aluminum [112]

Iqbal et al. [114] reported that BW model does not give accurate results in wide range problems. Meanwhile, the prediction of JC model reportedly gives more accurate and realistic results.

There are many alternative models proposed for failure of the material. For example, The Wilkins Model depends on only material characteristics (fracture strain, hydrostatic and deviatoric stress states), and it does not depend on the loading or geometry of the material. [111]. Further information and the calibration of the failure models can be followed from the reports [112], [115].

As a conclusion of this section a comparison of failure modes regarding fracture models would be good to visualize. Teng et al. [116] reported a small comparison table for three different models in Figure 40.
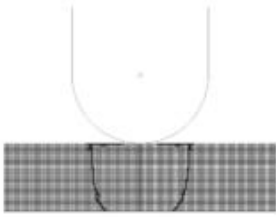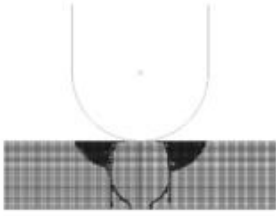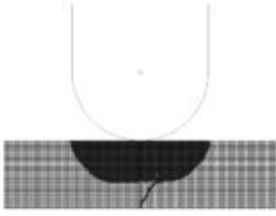
Fracture criteria	Fracture patterns	Failed elements
Bao-Wierzbicki Eq. (4)		
Johnson-Cook Eq. (7)		
Const. frac. strain $\varepsilon_f = 0.3$		

Figure 40 Comparison of Failure Criteria [116]

CHAPTER 5

NUMERICAL AND EXPERIMENTAL STUDIES

The experimental investigations of this work are done in shooting gallery of Makina Kimya Endüstrisi Kurumu (MKEK) Small Arms Weapon Factory located in Kırıkkale, Turkey.

Since the scope of the thesis covers only ballistic behavior of layered target systems, the dynamic material properties of target materials are directly taken from the literature. So, the experiments conducted do not cover the material characterization testing procedures.

In terminal ballistics, there are many factors which are very hard to control and measure that affect the results of the tests. These factors are impact velocity, ambient temperature and humidity, angle of impact, horizontal and vertical yaw motion of the projectile etc. Thus, there is no globally accepted test standard for ballistic studies. However, NATO published several reports on test procedures of some kinetic energy projectile impact cases [12], [117].

According to the NATO AEP-55 standard, there is no ballistic test setup with specific construction details. But, there are some equipment needed to make a valid experiment. The equipment are as follows.

- Launching system
- Time counters (velocity detectors)
- Test specimen
- Target positioning equipment
- Yaw card (optional)

- Witness plate (optional)
- Camera (optional)

AEP-55 dictates that yawing of the KE bullet should be controlled for a valid impact test. Measurement of projectile yaw could be made by any proper method such as yaw card, orthogonal photography, X-ray method or Doppler radar system. The yaw card should be so designed that it must not cause an instability of the projectile. Yaw angle of a level 3 threat should be less than 5 degrees at any impact angle. Moreover, the impact velocity tolerance should be in the range of ±20 m/s at nominal impact speed [6].

Since the projectile velocity cannot be measured directly just prior to impact, velocity measurement equipment placed at a distant point where the target shattering would not cause a damage to the measurement equipment.

The velocity of the projectile drops due to the air drag by the distance between the measurement equipment and target. Furthermore, the distance from launcher to the target would affect the time of flight of the projectile, consequently the projectile will undergo gravitational forces which may ultimately increase the yawing motion of the bullet.

The velocity drop of the projectile can be calculated by the Eq.(60) where C_d is the air drag coefficient which is constant and it is taken as 0.33 for threat level 1-4 projectiles, 0.165 for threat level 5 projectiles, 1.5 for 20 mm FSP, ρ is air density (1.225 kg/m^3), D is the bullet caliber, m is the projectile mass, and X is the distance from measurement device to the target, V_i is incidence velocity and V_s corrected velocity [6].

$$V_s = V_i exp(-\frac{X\rho C_d \pi D^2}{8m})$$ (60)

84

In order to decrease the effect of air resistance in measuring the impact velocity read by detectors to negligible levels, the distance between the target and the velocity detectors should be kept short.

The schematics of test set up is presented in Figure 41. For the experimental studies 7.62 mm AP bullets are used. A G3 automatic rifle is placed 16.5 m away from the target position. This distance is just enough for achieving stable flight of the bullet. Laser switching method is utilized to measure the bullet velocity. While the bullet is passing from the first switch the bullet cuts the laser light curtain and triggers the chronograph. As the bullet reaches and cuts the second light curtain the chronograph stops counting the time and calculates the bullet speed. The distance between the two switches is 5 m, and the distance from gun to the first switch is selected as 8 m. The distance between the second-time switch and the target position is selected as 3.5 m as shown in Figure 41.
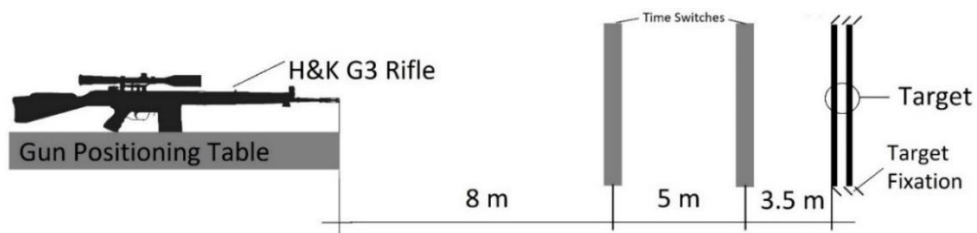
Figure 41 Experimental Test Setup

The target plates are press-cut in square shapes from 10 mm and 5 mm thick mild steel sheets. Since the area of sight is reduced for the oblique targets, the square target plate dimensions are selected as the side dimension of 200 mm to ensure subsequent strikes would not be affected by the former impact craters. The target plates are welded to each other or to 25 mm L-profile at the corners of the plates to demonstrate the pinned support boundary condition. Then, each welded target module is anchored to a massive table by bolted joints.

85

5.1. The Numerical Studies

5.1.1. Computational Scheme

There are mainly two types of hydrocodes developed to solve linear and non-linear engineering problems. They are Implicit and Explicit hydrocodes. Implicit solvers may converge during the solution of contact or material complexities. On the other hand, Explicit solvers use less disk space and memory during the computation. Explicit method is effective on wave propagation analyses. In general, explicit solvers are used for dynamic problems while implicit solvers give better results in static problems. Since the impact problems are very strain rate sensitive and requires element deletion and wave propagation, Abaqus/Explicit solver is selected as numeric solver.

There are several computation methods to simulate physical problems. Solid continua with finite deformations can be computed by Lagrangian processor. The Lagrangian Method describes problem with conservation laws. The code tries to solve the problem for each calculation step for every discrete element with the following criteria: Conservation of mass, conservation of energy and conservation of momentum. If the problem contains very large deformations such as fluid or gases flow, Eulerian processors may give better results. In such problems, sometimes a hybrid of the two may be a better approach. The Arbitrary Lagrangian-Eulerian (ALE) method is utilized for this kind of problems. However, the above-mentioned methods require mesh discretizing of the media. An alternative method describing scattering behavior of the media is the Smoothed Particle Hydrodynamics (SPH) method [117]. Although Abaqus v6.14 can use any of these methods to solve engineering problems, the Lagrangian method is used for impact problems in this thesis.

In order to solve a high-speed impact problem, a numerical model should be constructed. The constructed numerical model includes mechanical and material

properties of the media being interaction. As a last step, a numerical solver should be determined. The obtained numerical results should be compared with the experimental findings (Figure 42).
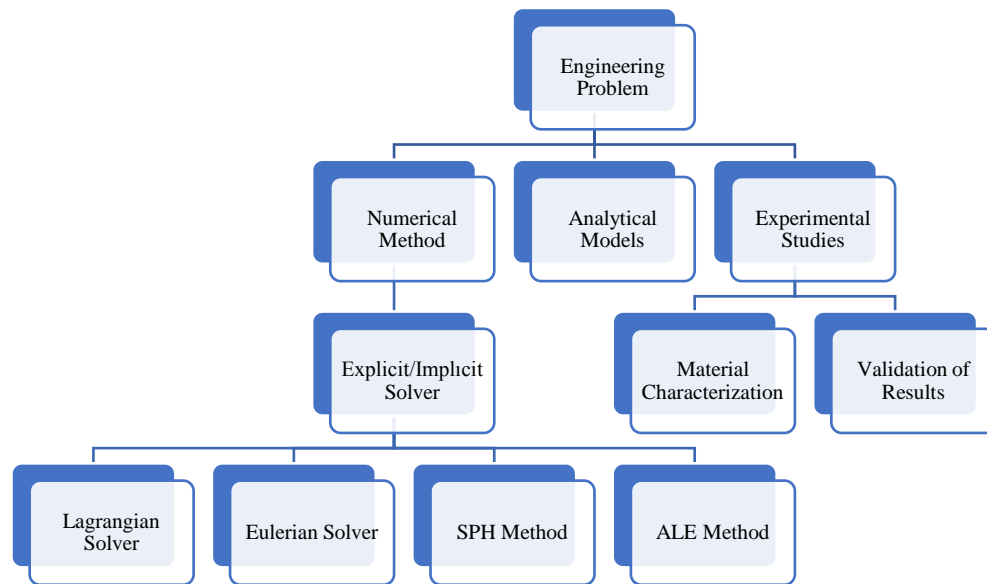
Figure 42 Approach to Engineering Problems

5.1.2. The Contact Algorithm

There are mainly three different types of contact algorithm embedded in Abaqus finite element analysis program. They are general contact, contact pairs and contact element. The explicit solver module includes the general contact and contact pairs algorithms. These algorithms allow the user to define contact of rigid-deformable body interactions, self-contact of the body, contact of eroding bodies with node-based surface definition, moreover, contact between Eulerian or Lagrangian bodies also can be defined. In more complicated problems, the general contact and the contact pair algorithm can be defined to the problem at the same time.

In the general contact algorithm, the bodies in the interaction are included in the model definition. However, including or excluding of selective surfaces of the model is possible for user intervention. The contact pairs algorithm requires definition of each pair of surfaces being interacted. The contact pairs definition includes the kinematic or penalty method.

5.2. Selected Material Model and Material Properties

The nature of the impact problem highly depends on the material properties being interacted. The proposed material model should describe stress-strain relations, effect of high strain rate deformations and temperature softening parameters. Material damage initiation criteria should also be identified in the numerical model.

The most commonly used constitutive model describing these properties is Johnson-Cook Constitutive model and Johnson-Cook Damage model. These models are also available in many hydro-codes as well as in Abaqus v6.14. In the scope this thesis, the material of the target plates is chosen as mild steel. The hardness of the target plates is measured as 132 HV (128 BHN). A standard tensile test specimen coupon [96] with 50 mm gage length is manufactured from the target plate. The tensile test performed with DARTEC tensile test machine. The yield strength (at $\varepsilon=0.2\%$) of the mild steel is found as 270 MPa and the ultimate tensile strength is found as 371 MPa. The plastic strain at fracture is calculated as 0.38.

Iqbal et al. [114] presented physical and mechanical properties of mild steel at high strain rate deformations. The material properties of hardened steel and brass jacket for the bullet core, and mild steel for the target are tabulated in Table 9. The same authors also noted the physical and mechanical properties of brass jacket of the bullet.

The JC-Damage criterion D3 is imposed as a positive value in the Abaqus implementation, because the software does not accept the negative value for this

parameter. In the JC Damage model definition, the parameter D3 exists in the exponential term. At the onset of damage, equivalent plastic strain decreases in most cases with the increase of stress triaxiality. Since the equivalent plastic strain at the beginning of ductile damage is an accumulative quantity it cannot be negative and the sign of this parameter should be reversed so that it will take a positive value [118].

Table 9 Johnson-Cook Material Properties of Bullet Components

Symbol		Unit	Hardened Steel Core [114]	Brass Jacket [28]	Mild Steel [114]
P	Density	kg/m^3	7850	8960	7850
E	Young's Modulus	GPa	202	124	209
N	Poisson's Ratio	-	0.32	0.34	0.33
A	Yield Strength Constant	MPa	2700	90	304.33
B	Strain Hardening Constant	MPa	211	292	422.007
N	Strain Hardening Exponent	-	0.065	0.31	0.345
$\dot{\varepsilon}_0$	Reference Strain Rate	1/s	0.0001	1	0.0001
C	Viscous Effect	-	0.005	0.025	0.0156
C_p	Temperature Softening	J kg^{-1} K^{-1}		386	477
T_r	Room Temperature	K	293	300	293
T_m	Melting Temperature	K	1800	1356	1800
M	Thermal Softening Parameter	-	1.17	1.05	0.87
D1		-	0.4	0.54	0.1152
D2		-	0	4.89	1.0116
D3	JC Damage Parameters	-	0	-3.03	-1.7684
D4		-	0	0.014	-0.05279
D5		-	0	1.12	0.5262

5.3. The Numerical Model of 7.62 mm AP Bullet

The geometrical properties and the mass of 7.62 mm AP bullet core are taken from the study of Børvik et al. [119]. They stated that the material of the armor piercing (AP) bullet core is a hardened steel with 6.1 mm in diameter and 27.6 mm in length with ogive nose profile. The major dimensions and the structure of the 7.62 mm AP bullet is presented in Figure 43. However, the exact profile geometry of the bullet nose, jacket and the lead cap are not available in open literature. Knowing the major dimensions of the bullet components, proper curves are fit to the nose profile and jacket profile which satisfy the mass properties of given components as presented in Figure 44.
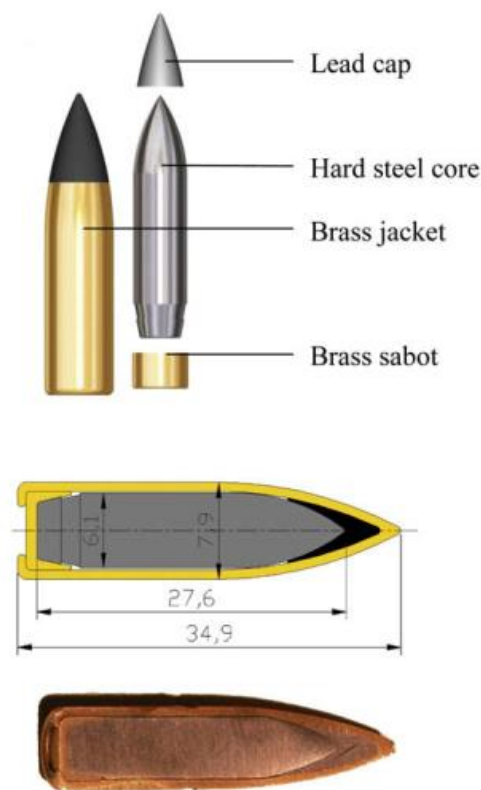
Figure 43 The Geometrical Properties of a 7.62 mm AP Bullet [119]
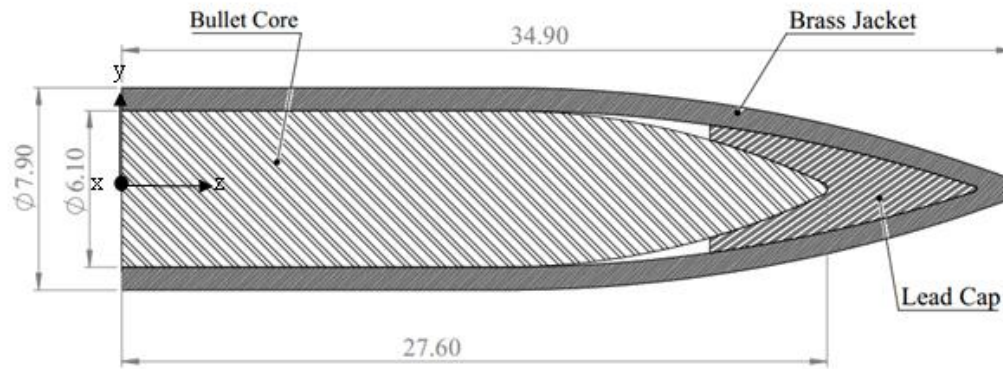
Figure 44 7.62 mm AP Bullet Assembly and Dimensions

The same authors also report the masses of brass jacket and lead cap. The brass jacket, which is made of CuZn10, has a mass of 4.4 g and the lead cap, which is an antimony-lead alloy, is 0.7 g in mass. The entire bullet is remodeled and assembled.

In the model presented in Figure 44 the mass-specific properties of the bullet core are calculated.

The bullet is modeled as analytical rigid part in Abaqus/CAE v14. The mass of the bullet core is found as 5.0 g which is consistent with the measured value in [119]. The mass is assigned to the calculated center of mass of the bullet core.

The moment of inertia around longitudinal axis (z axis) of the bullet is calculated as I_{zz}=21.69 g.mm^2 and the location of the center of mass of rigid core is found at 11.18 mm on z axis. The moment of inertias around x and y axes are calculated as I_{xx}=842.94 g.mm^2 and I_{yy}=842.94 g.mm^2, due to the symmetry of the problem, there will be no rotation around these y and z axes so, they are actually not needed to be imposed to the model.

Since there is no solid data about the tip radius of the bullet core in the literature, the nose radius the tip of the bullet is taken as R = 0.25 mm. A detailed drawing of 7.62 mm AP is presented in Appendix-A.

5.4. Numerical Model of Mild Steel Target

To visualize the plate bending and to decrease the computational cost, the target plates are modeled as 100 mm side length. Also, due to the symmetry and the boundary conditions of the problem half model symmetry is valid for the nature of the problem. Thus, the numerical model of the target plate is simplified to 100 mm x 50 mm with half symmetry.

The bullet core is assumed to make pure translation motion along –z axis. The symmetry plane of the target is assigned as x symmetry as shown in Figure 45.
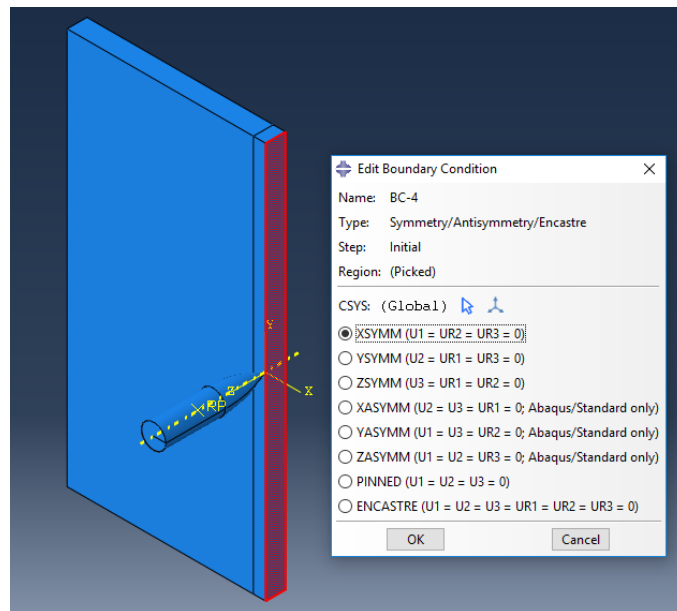
Figure 45 Half Symmetry Plane of The Target

A pinned support boundary condition is assigned to the free ends of the plate to simulate the fixing for the experimental studies as highlighted in Figure 46.
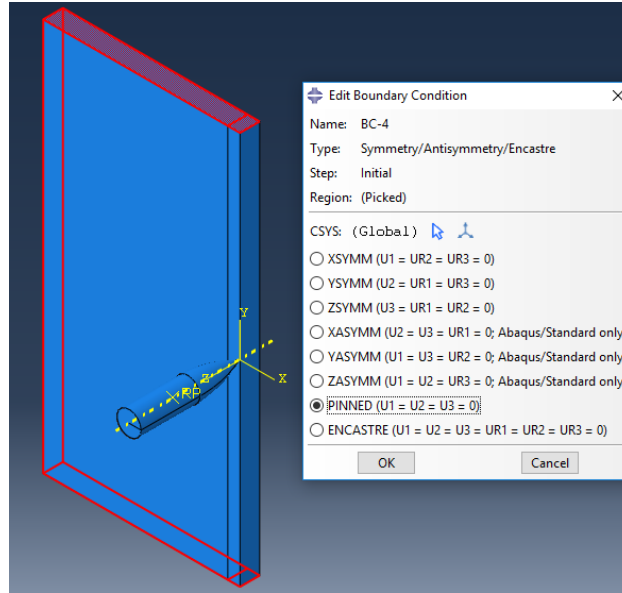
Figure 46 Pinned Support Boundary Conditions of The Target Plate

5.4.1. Mesh Convergence Study

High speed impact problems are highly mesh sensitive. The convergence study is carried out by discretizing the impact zone with different mesh sizes. In order to reduce the computational cost, the plates are partitioned in 4 distinct zones as shown in Figure 47 to determine the optimum mesh size for the problem. A 6.2 mm diameter zone on the plate is meshed with 8-node linear brick elements with reduced integration (C3D8R), an outer zone of 10 mm diameter ring is created and meshed with wedge elements (C3D6) in order to make mesh transition from the impact zone to the distant regions of the plate. This zone is enclosed with a diameter 16 mm ring zone which is meshed with 8-node linear brick elements (C3D8R) and the rest of the plate is discretized with larger size brick elements (C3D8R).

94
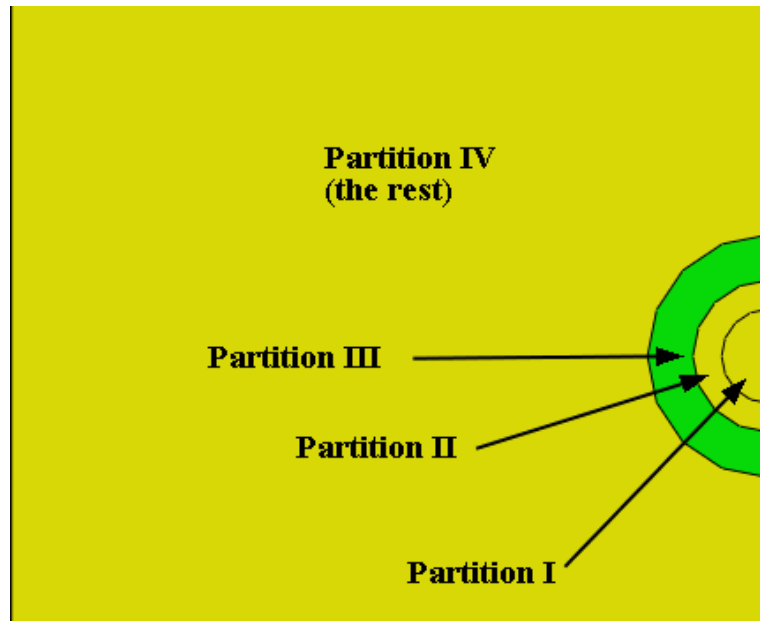
Figure 47 Partitioning of The Target Plate for Mesh Convergence Study

Since the partition I is greatly affected by the bullet impact, it is meshed with the smallest element size. The element sizes are increased with every subsequent expanding portion as seen in Figure 48. The outmost partition (partition IV) is meshed with approximate size of 0.5 mm elements. The approximate element lengths are 0.25 mm, 0.20 mm in partition III and partition II respectively. In the impact zone (partition I), mesh sizes are changed to find the optimum element size for the problem (ranging from 0.1 mm to 0.5 mm).
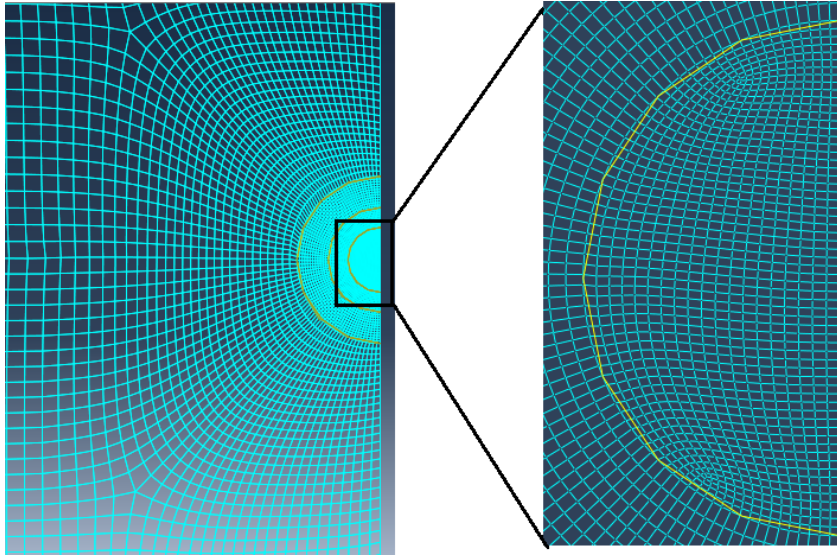
Figure 48 Mesh Transition (Front View)

Between the partition zones I and III, wedge elements are used to ensure the mesh transition uniform from fine elements to coarse elements. The element transition in partition zone II is presented in Figure 49.
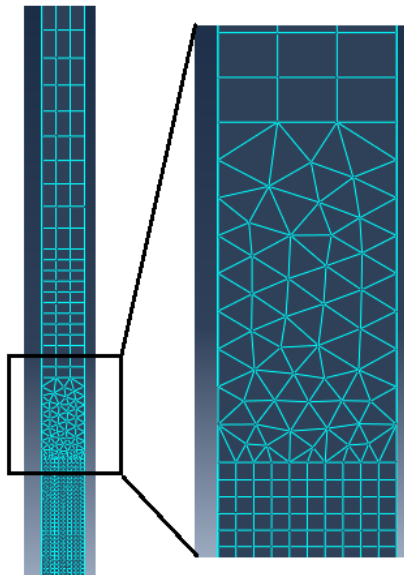
Figure 49 Mesh Transition for 1 mm Thick Target Plate (Section View)

In order to understand the mesh sensitivity of the problem, a 1 mm thick target plate and the rigid bullet core are chosen. To visualize a better mesh convergence, the bullet velocity is chosen as 100 m/s which is very close to ballistic limit for 1 mm thick target. The coefficient of friction between the plate and the bullet is selected as 0.1. The approximate element sizes at impact region (Partition I) decreased from 0.5 mm to 0.4, 0.3, 0.2, 0.1 mm respectively by keeping the aspect ratio of the elements (1:1:1) and exit velocity of the bullet core is plotted in Figure 50. Beyond the approximate element size of 0.2 mm no significant change of bullet exit velocity is observed despite there is a significant increase in the computation time. Thus 0.2 x 0.2 x 0.2 mm^3 element size selected for further calculations regardless of the target thickness. On the other hand, further decreasing the element size increases computational cost significantly as can be seen in Table 10.
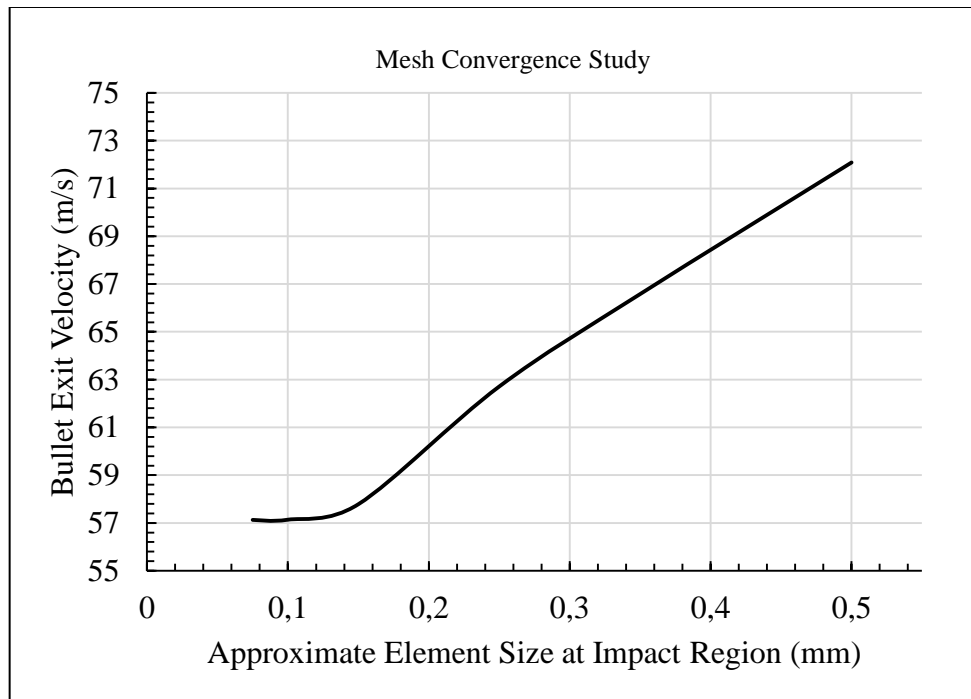
Figure 50 Mesh Convergence for Appropriate Element Sizes

Table 10 Computational Costs of Mesh Convergence Study

No. of Elements	Appr. Element Size (mm)	CPU Time (s)	Step Time (s)	No. of Increments
4352	0.5	0:47	8.000E-04	36452
7213	0.4	2:09	8.000E-04	58550
8489	0.3	2:33	8.000E-04	55659
11841	0.2	6:33	8.000E-04	95558
28619	0.1	31:10	8.000E-04	159942
43539	0.075	2:13:17	8.000E-04	435419

Since this work mainly investigates the oblique impact cases with spaced targets, another meshing strategy is needed to simulate impact zone behavior more accurately. The impact zone at the target plate is severely affected by the projectile at oblique impacts. In such cases, the projectile pierces the target with an elliptic hole and gains some angular velocity while exiting the first target. Thus, the projectile starts tumbling motion and hits the next plate with a greater angle (oblique plus yawing angles) causing a wider of elliptic penetration and generates a much wider elliptic exit hole.

Due to this reason, oblique impact cases require a comparatively larger contact region than the normal impact cases. This zone, may also referred as contact anticipated region, may increase by the angle of obliquity. Since the contact anticipated region at oblique impact cases is a very large zone, meshing of the first zone requires using the same element types with same sizes entirely.

Since, the target plate requires uniform meshing at the impact affected zone and it is comparatively wider, the further cases require a different meshing strategy. Because of this requirement, the target plate is partitioned with two distinct zones as shown in Figure 51. For example, for 5 mm thick target plate, the first zone covers a 3.1 mm width narrow distance from the symmetry plane. This zone is discretized with 187500 hexahedral brick elements with reduced integration type. However, in the second zone the element aspect ratio is gradually increased starting from 1:5 to 1:25 to reduce the number of elements and the computational cost. The same element type is selected for the rest of the plate and a total of 425000 elements are generated for the whole plate. Another mesh web is generated on the part using a different meshing strategy in order to reduce the number of elements. However, utilizing the alternative meshing strategy, less number of elements does not reduce the computational effort. This detail is discussed in detail in Appendix-B.

The contact definition between the bullet core and the contact anticipated zone at the target plate is defined using two distinct contact formulations. The "Normal Contact" with "Hard Contact" definition and the "Tangential Behavior" with "Penalty Contact" formulations were used to model bullet-plate interaction. The coefficient of friction for the penalty term in the contact formulation is selected as 0.1. The analytical rigid surfaces of the bullet core are selected as "Master Surface" and the impact region in the target plate is assigned as "Slave Surface". In-contact layered targets require one additional contact definition. That is the interlayer contact definition. In this type of target arrangement, both the contact anticipated zone and the rest of plate interacts with the subsequent layer. To define this contact formulation "General Contact" algorithm code is added to the input file.
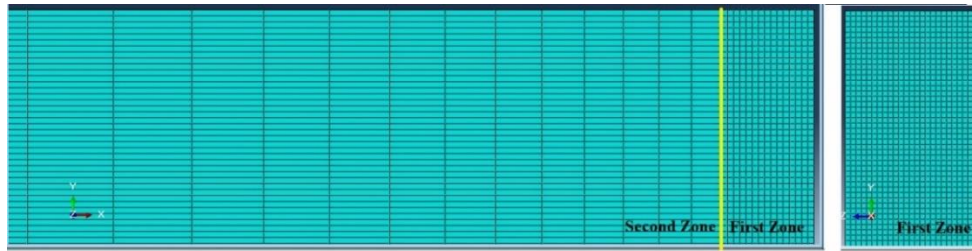
Figure 51 X-Axis Symmetric Model Mesh Web

5.4.2. Determination of Ballistic Limit Thickness Numerically

While determining the ballistic limit thickness of the mild steel against normal incidence of 790 m/s AP bullet core an iterative method is utilized. Starting from 40 mm thick target, the thickness is iteratively decreased and the analysis is rerun so that the bullet cannot completely pierces the target. The army ballistic limit definition is taken as basis while determining the ballistic limit thickness of mild steel plate against 7.62 mm AP bullet core having 790 m/s. This ballistic limit definition requires the bullet core to pierce the target but should be embedded in as can be seen in Figure 52. The ballistic limit thickness of the mild steel against a 7.62 mm AP core which have 790 m/s impact velocity at normal incidence is found numerically as 27 mm. This result is experimentally verified.
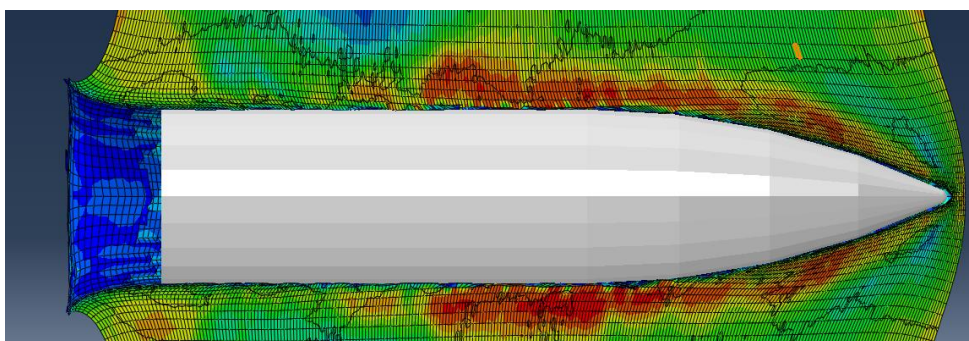
Figure 52 Ballistic Limit of a Mild Steel Against 7.62 mm AP Bullet

The bullet cores removed from the target after the experiment are shown in Figure 53. As observed from the figure, the deformation at the tip of the bullet core is negligible, so that even the turning marks did not vanish due to impact. This evidence shows that, assuming the bullet core as a rigid part will not affect the penetration mechanics of the bullet core.

Figure 53 The Bullet Cores Ejected From 27 mm Thick Mild Steel Target

The kinetic energy loss of the bullet core having an initial velocity of 790 m/s is plotted in Figure 54. Total time spent to full penetration of the bullet is calculated as 75 µs. As one can see, kinetic energy drop rate of the projectile is initially low, yet, it increases by the course of penetration, and the maximum deceleration is observed when the ogive part of the projectile totally penetrates the target.
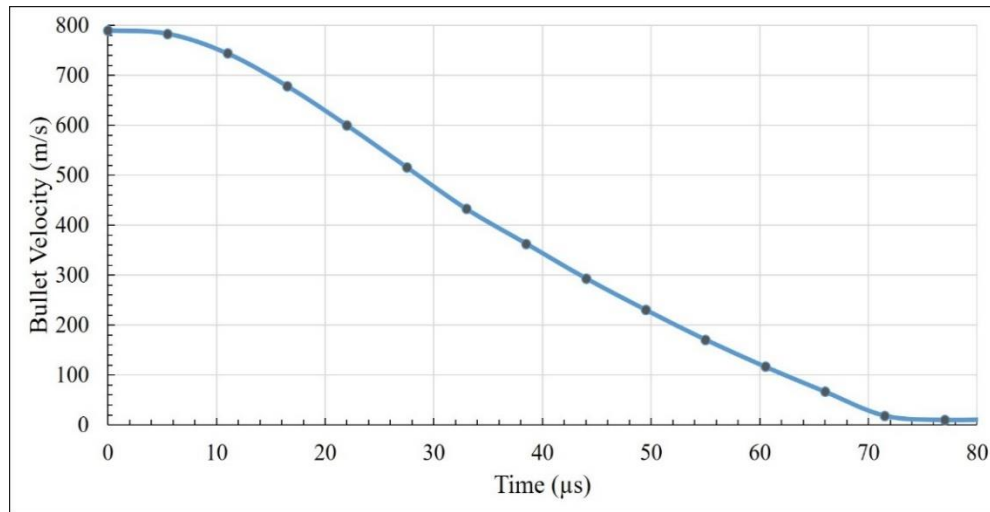
Figure 54 Velocity Drop of the 7.62 mm AP Projectile Against Ballistic Limit
Thickness Target

5.5. A Comparison on Analytical and Numerical Results

A 5 mm thick target is impacted with normal incidence angle at various velocities
ranging from 330 m/s to 800 m/s and bullet exit speeds were plotted in Figure 55.
The Recht-Ipson model parameters for 5 mm thick mild steel impacted by 7.62 mm
bullet core are obtained by curve fit of the results. Since there is not considerable
plug ejection observed by bullet core, the plug ejection parameter a in Recht-Ipson
empirical model is taken as unity. The parameter p is found as 2.13 from curve fit
of results of the numerical analyses.
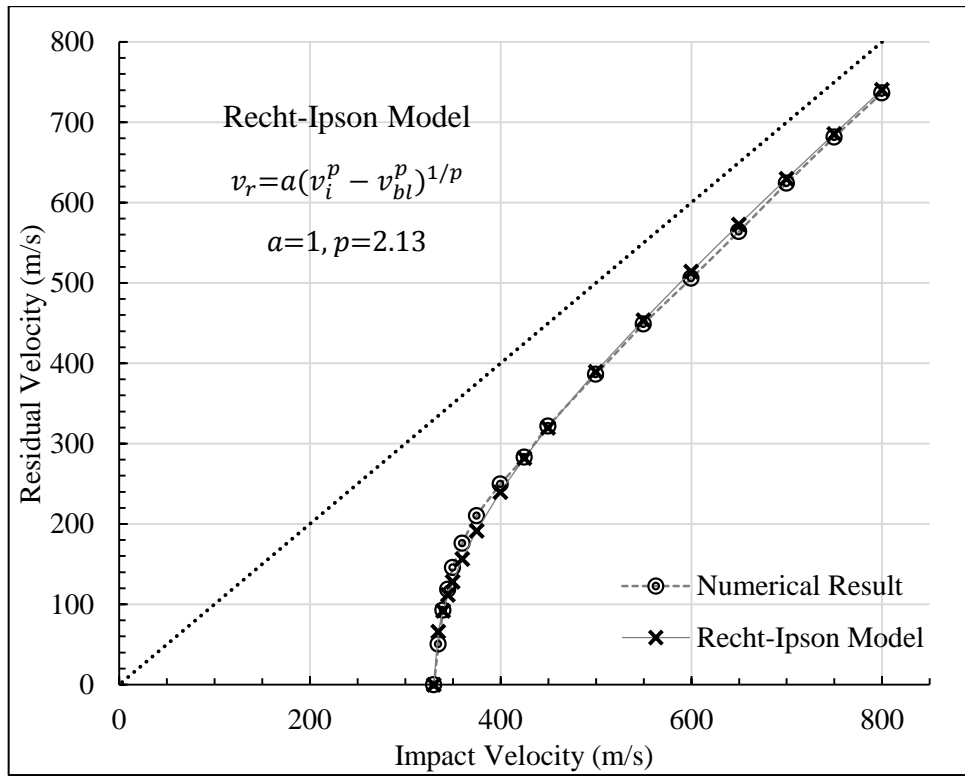
Figure 55 Bullet Exit Speeds Against 5 mm Mild Steel Target Obtained by Recht-Ipson Model Calculations and The Numerical Results

The Recht-Ipson model and the corresponding numerical analyses show great consistency at high velocities. However, the results of the analyses deviate from the calculated bullet exit speeds at the velocities close to the ballistic limit. The bullet exit speeds obtained by numerically and calculated by analytical model proposed by Recht & Ipson are tabulated in Table 11.

Table 11 Recht & Ipson Model and Numerical Results

v_i Incidence Velocity (m/s)	v_r Numerically Calculated Bullet Exit Velocity (m/s)	v_r Recht-Ipson Calculated Bullet Exit Velocity (m/s)
800	736,4	740,6
750	681,6	685,6
700	624,0	629,8
650	564,1	572,8
600	505,8	514,3
550	448,8	453,5
500	386,2	389,5
450	321,8	319,9
425	283,1	281,7
400	249,6	239,8
375	210,2	191,3
360	176,0	156,3
350	145,8	128,2
345	118,6	111,6
340	92,6	91,9
335	50,5	66,1
330	0,0	0,0

5.6. The Resistance of Single Targets with Varying Obliquities

Understanding how the obliquity affects the kinetic energy drop of a bullet core is important before proceeding the oblique and layered target systems. First of all, the critical angle of ricochet of the projectile having 800 m/s incidence velocity is determined for every thickness of the target from 1 mm to 10 mm. An iterative method is followed to determine the critical angle of ricochet of the projectile at 800

m/s incidence velocity. Numerically obtained results are plotted in Figure 56 and tabulated in Table 12.
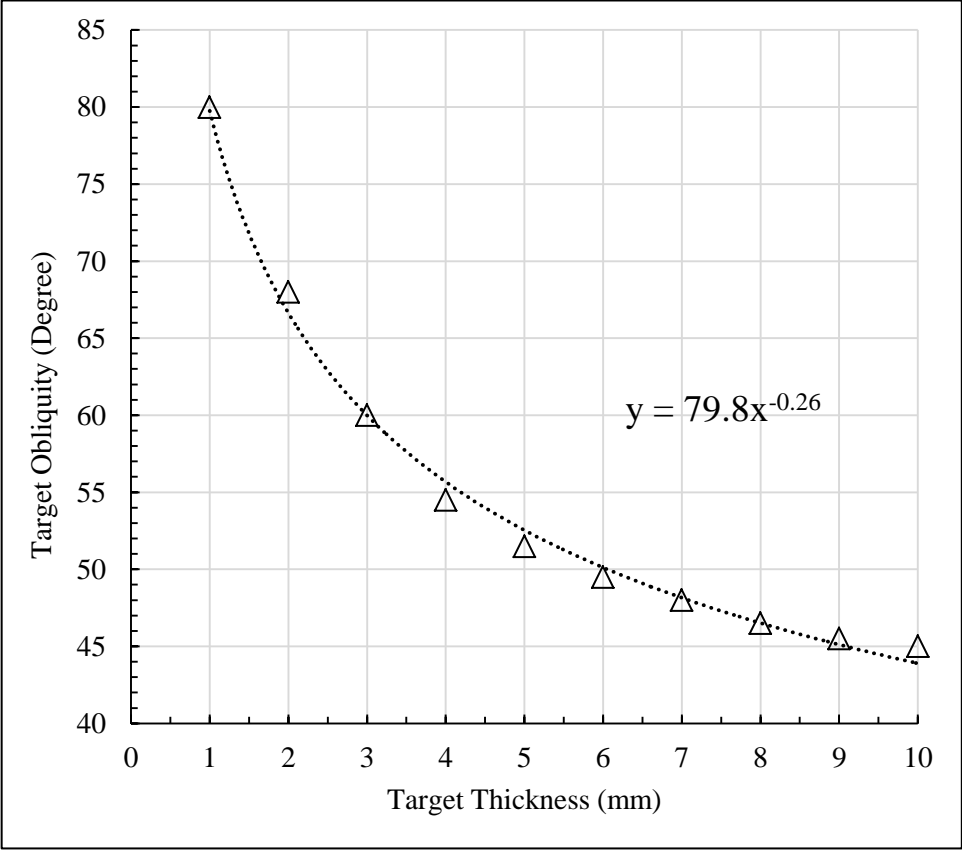
Figure 56 Critical Angle of Ricochet vs Target Thickness at 800 m/s Incidence Velocity

As one can see from Figure 56, there is an inverse relation between the critical angle of ricochet and the target thickness. In other words, defeating the bullet by ricocheting is possible at higher degrees of obliquity for thinner plates. However, thicker the target, lower the critical angle of ricochet until 45 degrees. This result may also indicate that, by controlling the angle of impact of the projectile at every

subsequent layer of target configuration one can determine the order of layers of the target plates.

Table 12 The Table of Critical Angle of Ricochet by per Thickness of Target Plate

Target Thickness (mm)	Critical Angle of Target for Projectile Ricochet (°)
1	80
2	68
3	60
4	54,5
5	51,5
6	49,5
7	48
8	46,5
9	45,5
10	45

The target plates from 1 mm to 10 mm thickness are modelled and simulated for purely oblique impact cases including zero obliquity, assuming the bullet moves without any yawing, and the bullet exit velocities are plotted. As shown in Figure 57 the bullet exit velocities are greatly affected by the oblique angle of the projectile. However, velocity drop of the bullet against oblique targets of different thicknesses represent clearly a distinct behavior. Thin targets do not show considerable increase in the ballistic resistance against the projectile above 20-degree obliquity, while, an opposite fashion is observed for the thicker targets. Namely, the ballistic resistance of the thick and intermediate thick targets drastically increases above 20 degrees of obliquity.
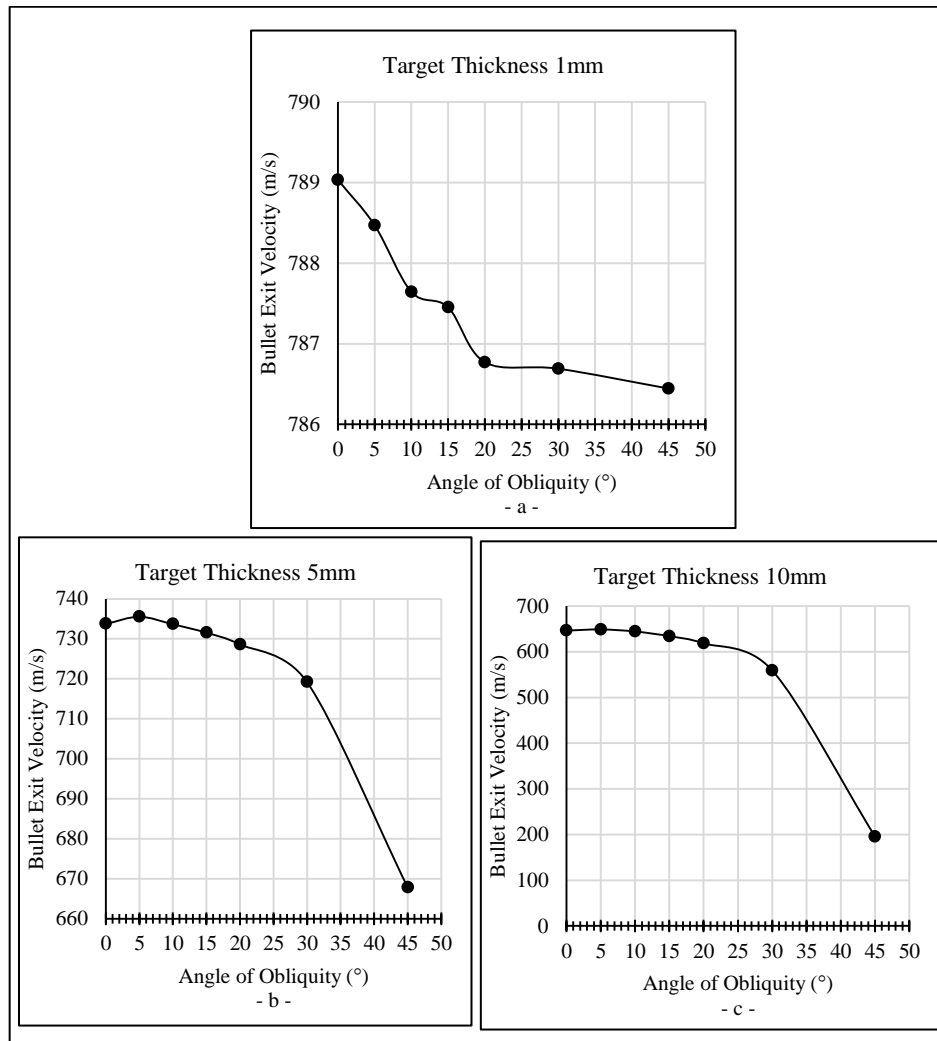
Figure 57 Target Plates in Different Thicknesses Impacted by Varying Degrees of Obliquities (Impact velocity = 800 m/s)

As seen in Figure 58, the analytical approach shows that the kinetic energy loss of a rigid projectile having 800 m/s initial velocity impacting a 1 mm thick target can be increased from 2.7% to 3.4% as the angle of obliquity is increased from 0 degree to 45degrees. Numerical results of 1 mm thick mild steel target show that increasing

the obliquity beyond 20 degrees do not contribute the target effectiveness in a broad sense (Figure 58).
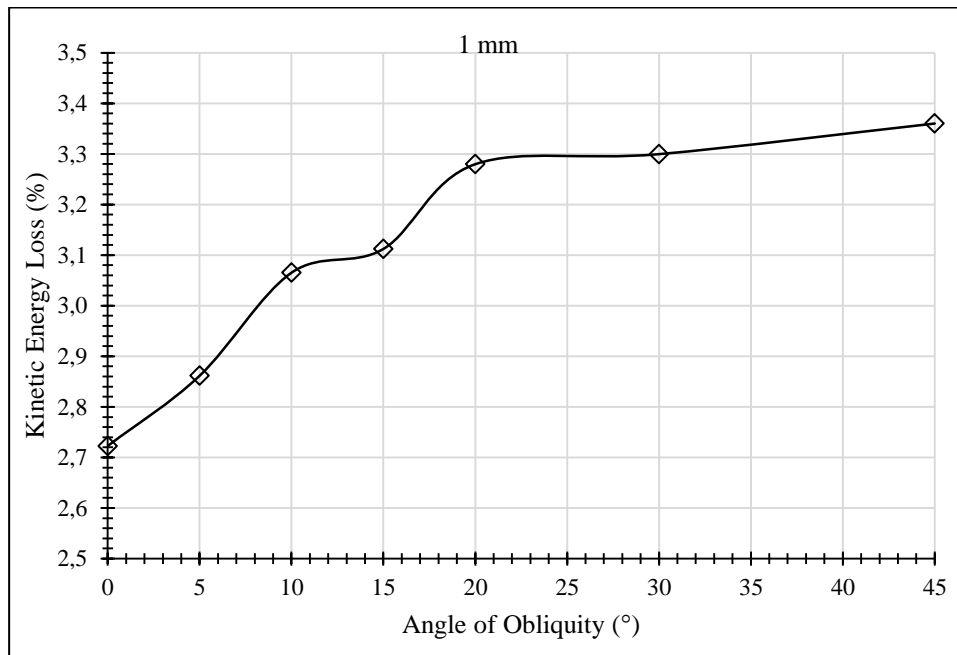
Figure 58 Kinetic Energy Drop of the Projectile Against 1 mm Target at Varying Obliquities

Contrary to this result, increasing the target thickness makes the projectile more sensitive to target obliquities especially beyond 15 degrees of obliquities. Figure 59 presents the effect of the angle of obliquity on the kinetic energy of the projectile. As one can see in the same figure, beyond 15 degrees of obliquity, considerable kinetic energy drop occurs for any target thickness. Another important result can be seen at this point is the targets especially thicker than 5 mm, resist oblique bullet impact to a greater extent.
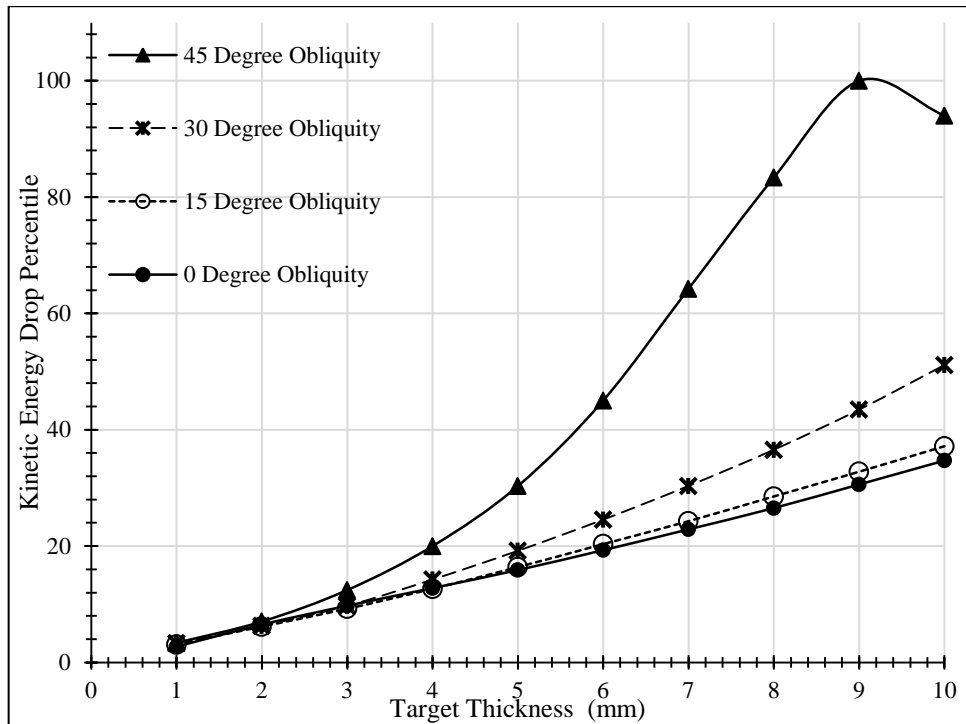
Figure 59 Effect of Target Obliquity

For example, the results reveal that at normal incidence angle, 10 mm target reduces the kinetic energy of the projectile by 34.7%, however, when the angle of incidence is increased to 45 degrees, the projectile ricochets with a kinetic energy loss of 94%. Figure 60 shows the resistance of 5 mm and 10 mm targets of varying obliquities.
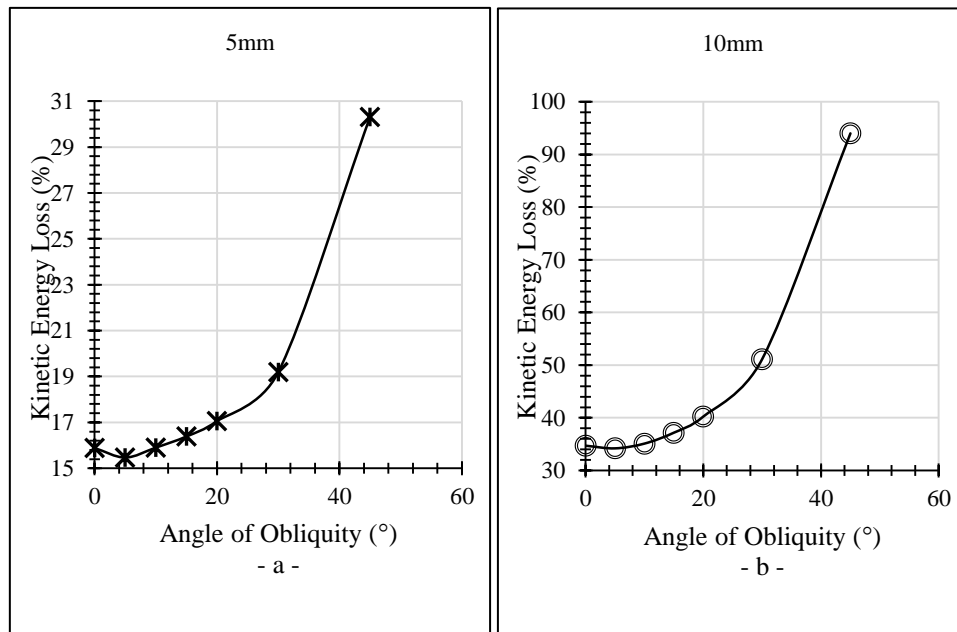
Figure 60 Kinetic Energy Drop of The Projectile Against 5 mm and 10 mm Targets
at Varying Obliquities

45 degrees of obliquity is found as the critical angle of ricochet numerically. This result is also verified with the experiments. The experimental depth of penetration and the penetration crater length have great consistency with the numerical results. Figure 61 shows the sectional and isometric views of 10 mm thick target with 45-degree obliquity impacted by a rigid bullet core having initial velocity of 800 m/s. Figure 62 shows the experimental results of the same target shot twice. The bullet velocities for the shot numbers, #4 and #5 which are written on the parts, were measured as 794.7 m/s and 791.1 m/s respectively.
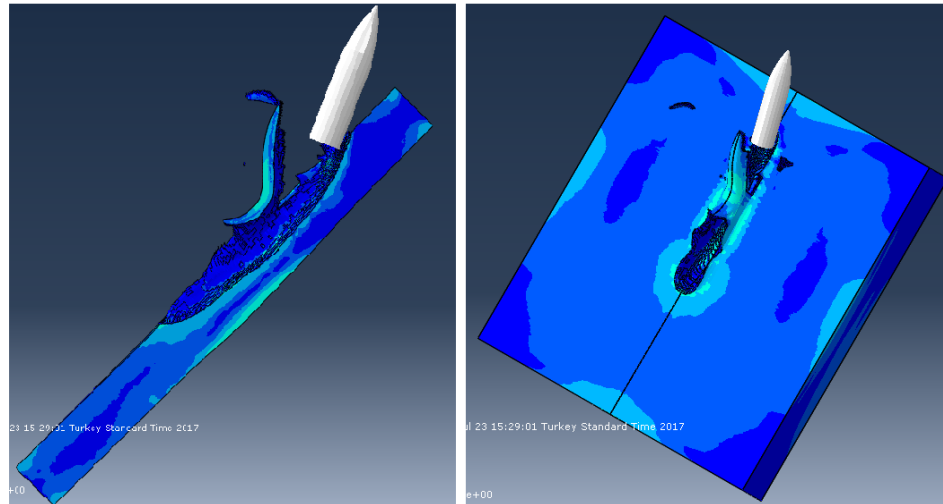
Figure 61 Ricochet of the Projectile from 10 mm-Thick Target

V_i=791.1 m/s V_i=794.7 m/s

Figure 62 Deformations on the Target Plate by the Ricochet of 7.62 mm AP Bullets

Another criterion mentioned before is the target effectiveness in terms of the areal density of target plates. The areal density is the weight per unit projected area [13], [2]. A comparison of areal density and the kinetic energy loss of the projectile calculated numerically is presented in Figure 63.

The nonlinear increase in kinetic energy loss of the plates can easily be observed. This increase becomes more effective as the target thickness increases.

$$Areal\ Density\ [\frac{kg}{m^2}] = t' * \rho \qquad (61)$$
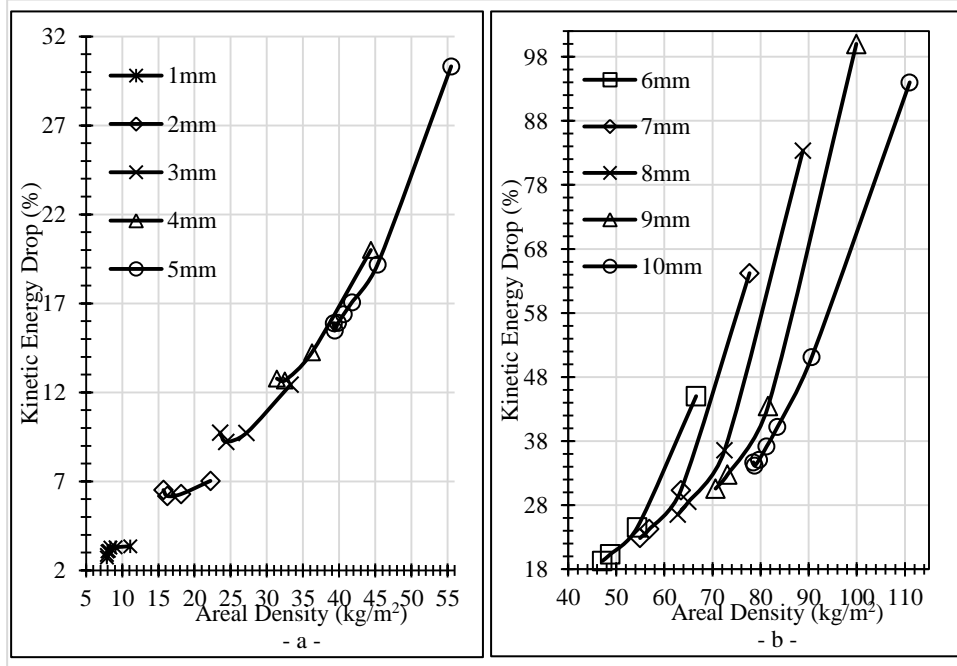
Figure 63 Areal Density vs Kinetic Energy Drop (V_i=800 m/s)

5.7. Effect of Layering and Spacing of Target Plates

Layering, spacing and different obliquity possibilities require many combinations of arrangements. These combinations may sometimes be confusing. Furthermore, elimination of some target thicknesses is needed to decrease the number of numerical analyses and experimental efforts. In this work, only two different plate thicknesses are considered. 5 mm and 10 mm thick mild steel plates and their numerical models are used for the sake of reducing the total number of possible

target arrangements. Also, 4 different obliquities and 4 different spacing cases are projected for 5 mm and 10 mm target plates.

A nomenclature guide of investigated target arrangements is presented in Table 13. This nomenclature is used for naming the target configurations in this work.

Table 13 Target Nomenclature

	Target Thickness		Interlayer Spacing	
Target Obliquity	5 mm	10 mm	0 mm	-
0	**1**	**2**	30 mm	**A**
15	**3**	**4**	50 mm	**B**
30	**5**	**6**	75 mm	**C**
45	**7**	**8**	100 mm	**D**
Bold Characters Represent the Case Numbers				
All angles are CW rotation, reversed angle denoted by letter "R", CCW				
Subsequent numbers (numbers without letter config.) denote contacting plates (i.e.; 1-1-1-1 denotes 4 x 5 mm contacting plates)				

5.7.1. Effect of Layering and Spacing of Plates in Normal Impact Cases

In order to understand how the velocity of the bullet core drops against normal impact, the total thickness of 20 mm target plates is investigated. Keeping the total thickness 20 mm, the target is layered using 5 mm and 10 mm thick plates. Furthermore, the layered plates are arranged both in-contact and spaced configurations. In Figure 64 the velocity change of the bullet core is plotted for 20 mm thick monolithic target, four pieces 5 mm thick contacting plates (1-1-1-1 case), four 5 mm thick 30 mm spaced target (1A1A1A1 case) and four 5 mm thick 75 mm spaced target (1C1C1C1 case).
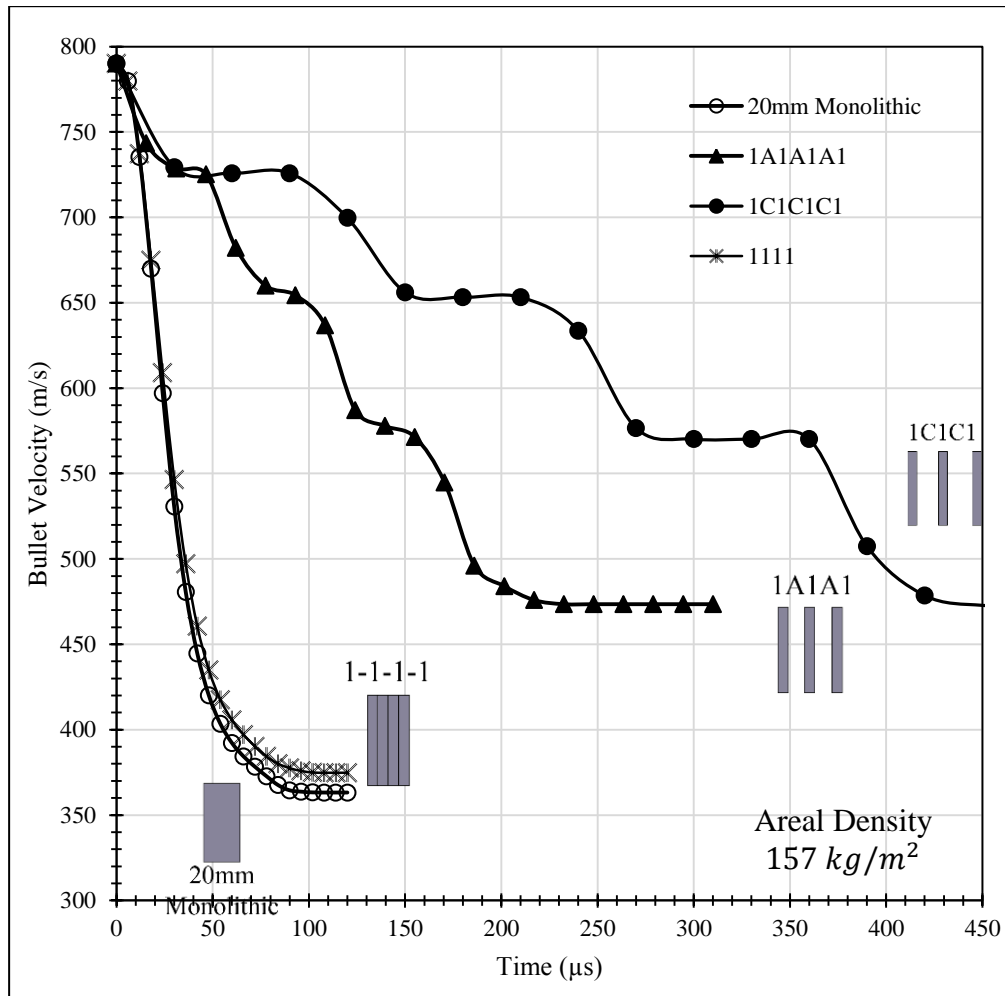
Figure 64 Velocity Drop of Some In-Contact and Spaced Targets (Normal Impact Cases)

Table 14 presents the bullet exit velocities of 20 mm thick monolithic target, 5 mm in-contact layered target, 30 mm and 75 mm spaced targets of 5 mm thick plates. The highest target resistance is obtained by the monolithic target configuration while, the layering of the target (provided that the plates are in contact) impairs the protection of the target by 3.5%. This finding is confirmed by Gökgöz's work [120]. As a result, it can be said that at normal impact cases, the interlayer distance (the

114

shortest distance between layers) does not cause a significant change in the bullet exit velocity.

Table 14 Bullet Exit Velocities of Monolithic, In-Contact and Spaced Targets

Configuration	Bullet Exit Velocity (m/s)
1-1-1-1	375
1C1C1C1	472,8
1A1A1A1	473,2
20 mm Monolithic	363,2

The sequence of the layer thicknesses may also affect the ballistic resistance of the target. 2-2, 1-1-2 and 2-1-1 cases are arranged and analyzed to evaluate how the sequence of the layers affects the ballistic resistance of target. The bullet velocities are plotted for 20 mm monolithic target, 1-1-2, 2-1-1 and 2-2 target arrangements in Figure 65. In example, whether placing the thicker plate in the front (bullet to impact first) would affect the ballistic resistance is investigated.
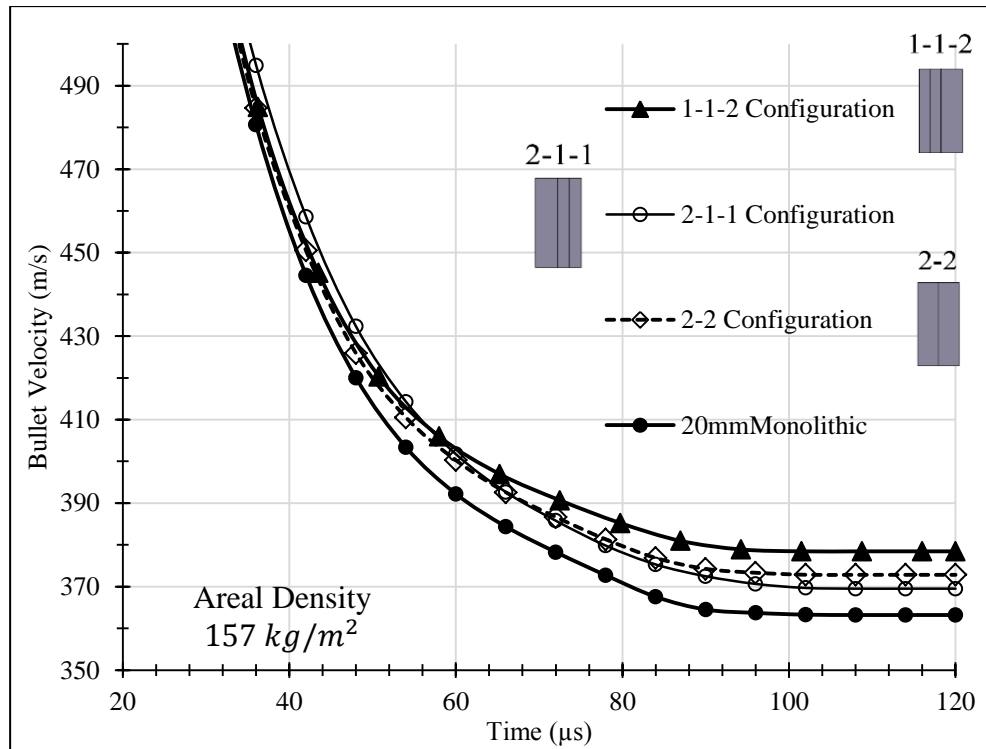
Figure 65 Velocity Drop of the Projectile Under In-Contact Layering
Configurations (V_i = 790 m/s)

As can be seen from the Table 15, using thinner plates as frontal plates impairs the resistance of the target. However, using a thick target as a front plate contributes to the resistance of the target. Changing the order of layer from thinner layer as a front to thicker layer as a front plate influences the penetration of the bullet which causes a drop of the bullet exit velocity about 2.6%.

Table 15 Residual Velocity of Bullet of In-Contact Type Layered Targets

Configuration	Residual Velocity (m/s)
2-2	372,8
1-1-2	378,5
2-1-1	369,5
20 mm Monolithic	363,2

The experiments conducted show that the average bullet velocity is measured as 790 m/s. Thus, 790 m/s initial velocity is assigned to the bullet core for all cases in numerical analyses.

From the numerical results, the bullet exit speed from the 20 mm thick monolithic target is found as 363 m/s. This result is compared with a case in which the plate thicknesses are reduced to half but the total target thickness kept the same.

The two 10 mm thick plates are arranged as in-contact type target. The experiment conducted on 2-2 configuration (10+10 mm in-contact) shows that the numerical result and the experimental study are in good agreement. The frontal and rear surfaces of the impacted target plates are shown in Figure 66 and Figure 67. The bullet velocities before impact for the shots #1 and #2 are recorded as 792 m/s and 793.5 m/s respectively.

Figure 66 Frontal Image of the Impacted Plate 2-2 Configuration (20 mm Total Thickness)

By inspecting the pierced target holes from Figure 66, there is a considerable bullet rotation in the target material is observed. In the Figure 66, shot number #1, the jacket material of the bullet smeared petal formations in the to the bullet entry hole. The inhomogeneous bullet entry petal formations show that, the bullet actually does not hit to the target perfectly normal to the target surface.

Figure 67 Rear Surface of The Impacted 2-2 Configuration (Back of Second Layer)

118

5.7.2. Effect of Parallel Layering and Spacing of Plates in Oblique Impact Cases

Effect of obliquity in parallel spaced targets investigated numerically. 5 mm thick target plates are separated at 30 mm, 50 mm, 75 mm and 100 mm distances. The results are plotted in Figure 68, Figure 69 and Figure 70. Figure 68 shows the kinetic energy of the bullet core during penetration of 15-degree oblique plates with different gap distances. 3C3C3C3 arrangement is found as the best arrangement among 15-degree oblique plates with different interlayer spacings. 75 mm interlayer distance causes 87% kinetic energy drop of the projectile. While 30 mm spaced target (3A3A3A3) causes 71.5% kinetic energy reduction in the bullet, 75 mm spaced target (3C3C3C3) causes 86.8% kinetic energy reduction.
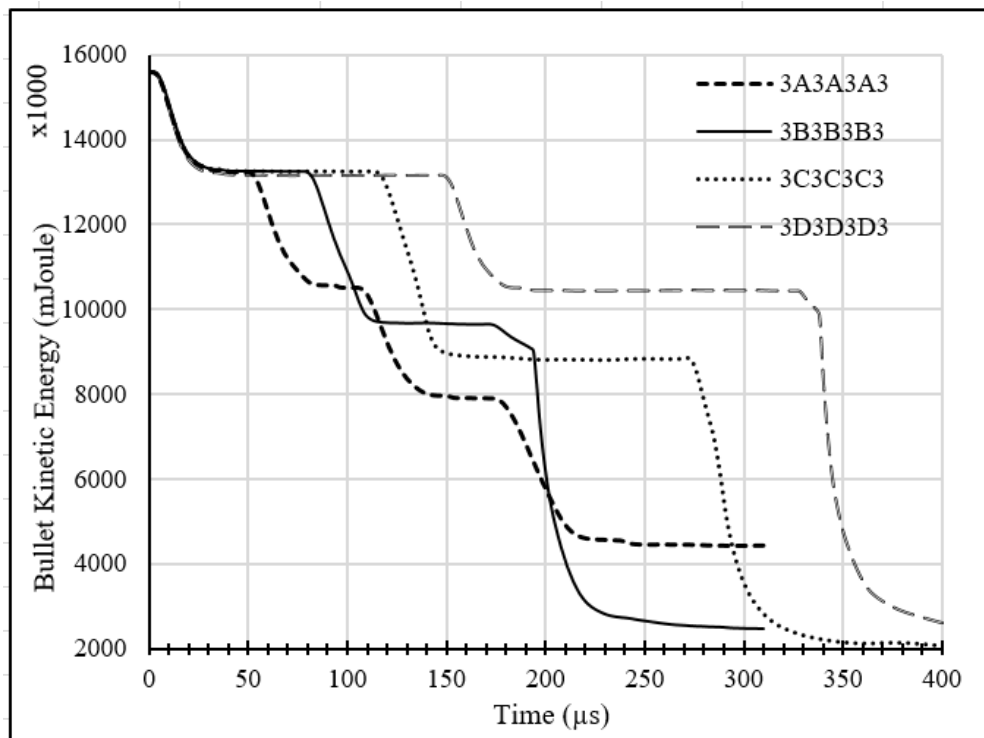
Figure 68 Effect of Spacing in 15 Degrees of Obliquity Target Arrangements

From the Figure 68, the best arrangement is found as the 75 mm spacing (3C3C3C3) which is superior to the other spacing cases. However, 30 degrees of obliquity eliminates the negative effect of the spacing of the target layers as seen in Figure 69. The interlayer gaps do not affect the bullet residual kinetic energies as seen in Figure 69 in 30-degree oblique target configuration. Yet, 50 mm spacing with 30-degree obliquity provides a better protection compared to the other spacing conditions. Interpreting the numerical results and Figure 68, the bullet completely pierces the first 3 layers of the target 5A5A5A5, but it ricochets from the fourth layer. On the other hand, the bullet pierces the first two layers of the other arrangements 5B5B5B5, 5C5C5C5 and 5D5D5D5, and loses the 95%, 98% and 95% of its initial velocity respectively.
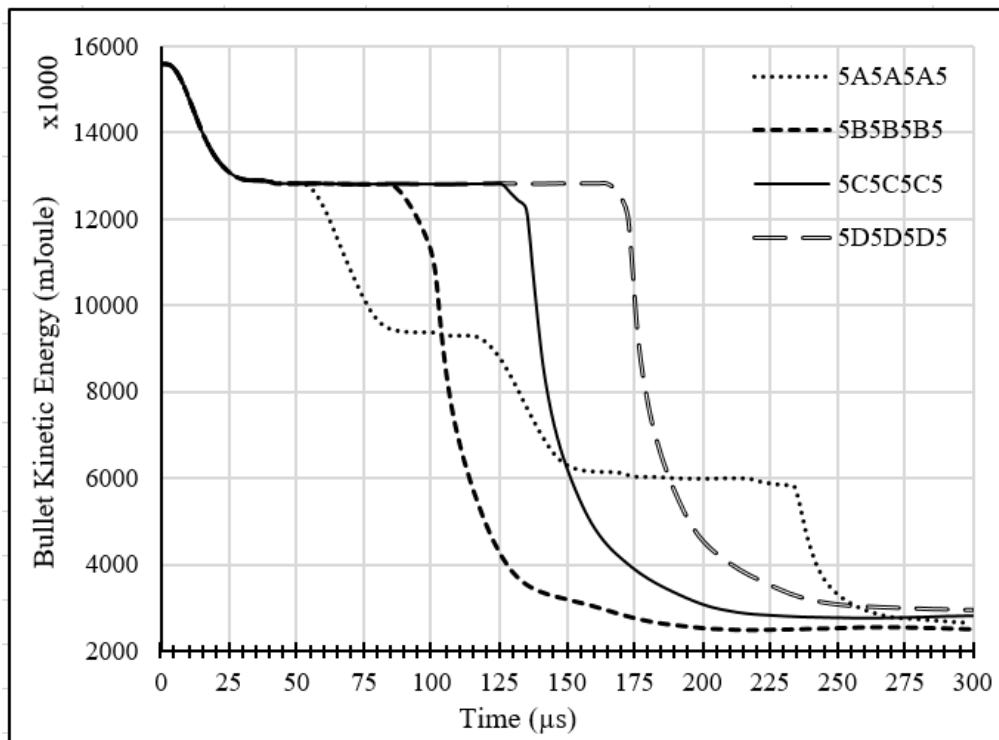
Figure 69 Effect of Spacing in 30 Degrees of Obliquity Target Arrangements

The kinetic energy loss of the projectile is found almost the same 45-oblique plates irrespective of the layer spacing. The kinetic energy drop of the projectile against

different spacing cases is presented in Figure 70. All the target arrangements cause the bullet to ricochet from the second layer after completely piercing the first layer. Thus, the residual kinetic energy of the projectile is close to each other for 45 degree oblique targets.
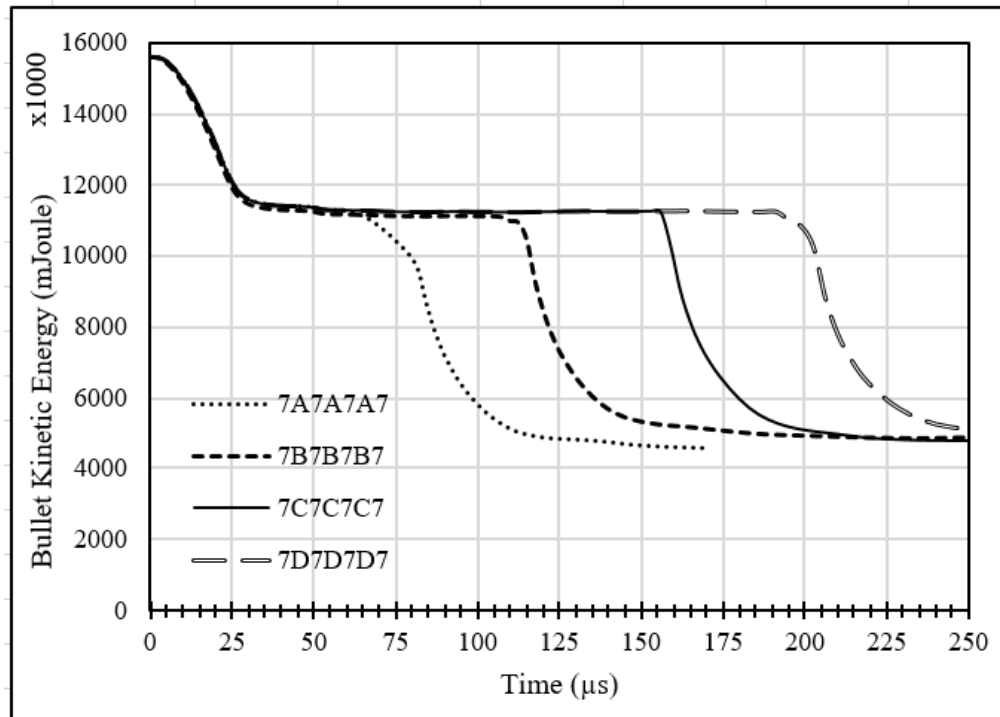
Figure 70 Effect of Spacing in 45 Degrees of Obliquity Target Arrangements

45-degree oblique targets ensure the total protection with projectile ricochet. The bullets completely ricochet from the second plate (plate no.1 is assumed at the impact side) at the targets 7A7A7A7, 7B7B7B7, 7C7C7C7 and 7D7D7D7. The bullet core pierces first layer and cause a wide bulging on the second layer and ricochets. Though, the bullet core causes a great damage to the second layer, it loses much of its kinetic energy by attaining tumbling motion as can be seen in Figure 71. Kinetic energies of the bullet core in 45-degree target arrangements are plotted in Figure 70.
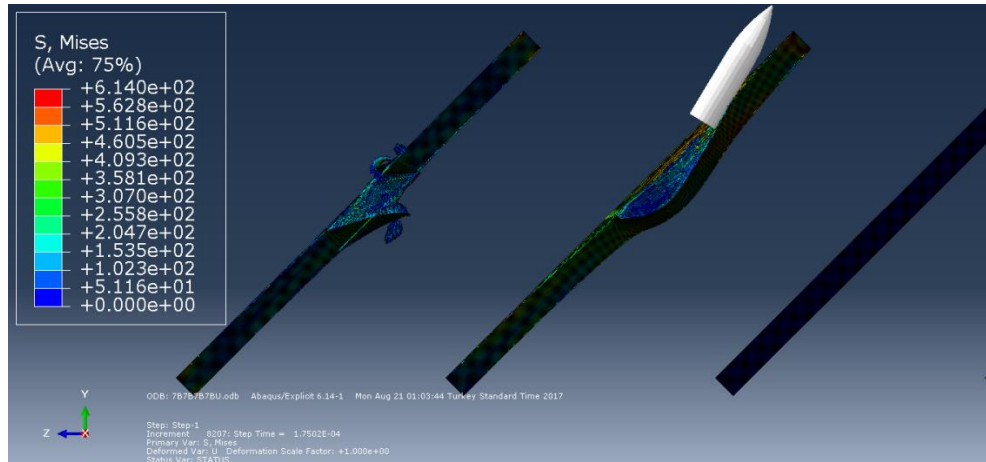
Figure 71 The Numerical Result of The Damage of 7B7B7B7 (Impact Side Left)

The 7B7B7B7 plates are impacted experimentally, and the impacted plates are presented in Figure 72. The bullet speeds for the shot numbers #11 and #12 are measured as 790.7 m/s and 791 m/s respectively. As can be seen in Figure 72, the bullet core pierces the first layer and causes a wide bulge on the second plate but it ricochets from the second layer. This result seems contradicting with the experimental result. The both shots #11 and #12 shows that the projectile breaks into two pieces and one piece of the projectile is found completely pierces the second layer. This result shows that rigid projectile assumptions may overestimate the real case in highly oblique targets.
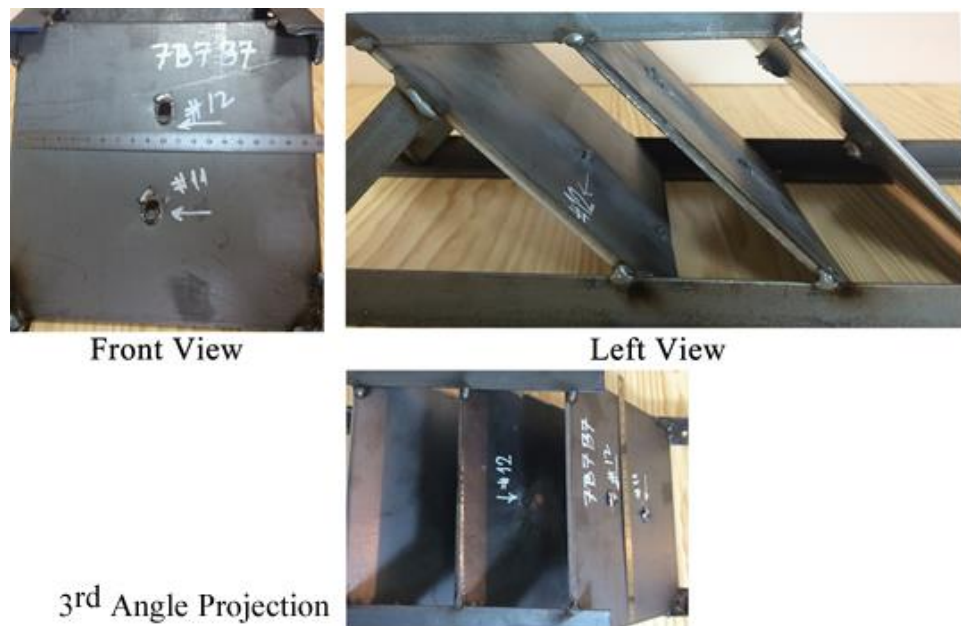
Figure 72 View of The Impacted 7B7B7B7 Target

The effect of obliquity in parallel spaced targets is investigated both numerically and experimentally. Numerically calculated results of kinetic energy drop of the bullet core are plotted in Figure 73, Figure 74, Figure 75 and Figure 76. Considering 30 mm spacing of layered targets, the best obliquity for the targets is found as 30 degrees. The kinetic energy loss of the bullet core against 30 mm spaced of varying obliquity is plotted in Figure 73. The lowest projectile residual velocity after ricocheting from the fourth layer is calculated in the target which have 30 degrees of obliquity and 30 mm interlayer distance (5A5A5A5). The bullet completely pierces the target (3A3A3A3) with 388m/s residual velocity, while the bullet ricochets from the second layer.
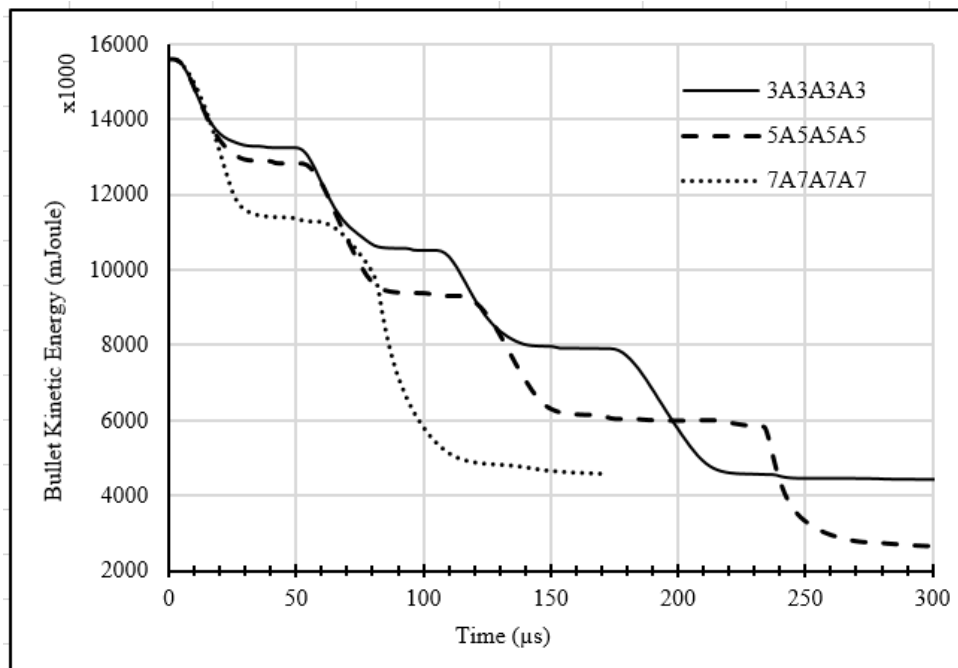
Figure 73 Effect of Interlayer Spacing and Obliquity (30 mm Spaced Targets)

Inspecting the Figure 74, the kinetic energy loss of the bullet core against the obliquity of 30 degrees and 45 degrees show a very similar fashion. If the spacing is increased to 75 mm the highest protection is obtained from 15 degrees of obliquity with the highest ranking of all parallel and oblique impact cases using 5 mm thick targets. The bullet exit velocity is calculated as 80.6 m/s after exiting of the third target which is not high enough to defeat the fourth plate. A similar mode is observed in Figure 75.
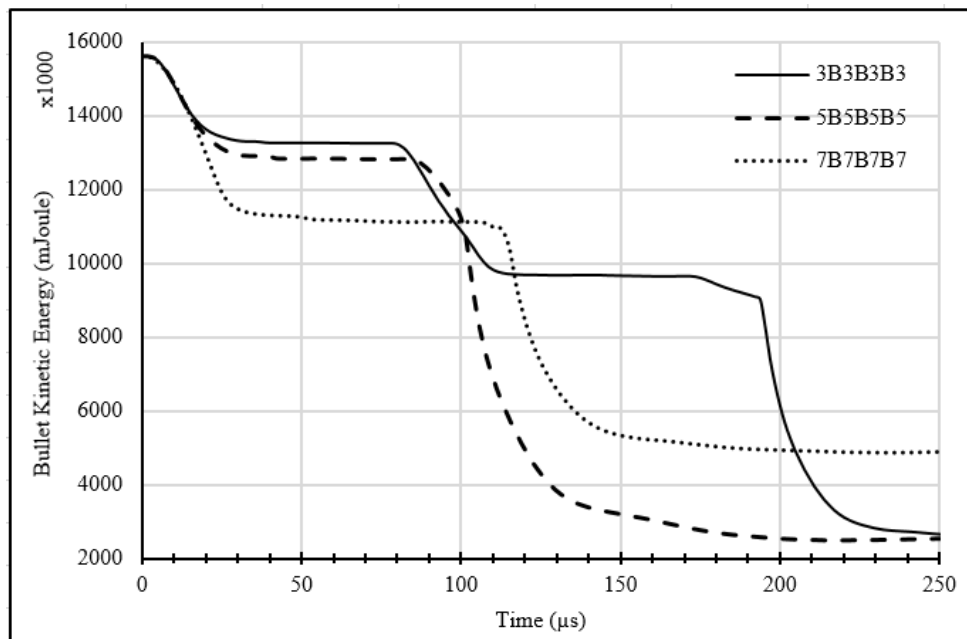
Figure 74 Effect of Interlayer Spacing and Obliquity (50 mm Spaced Targets)
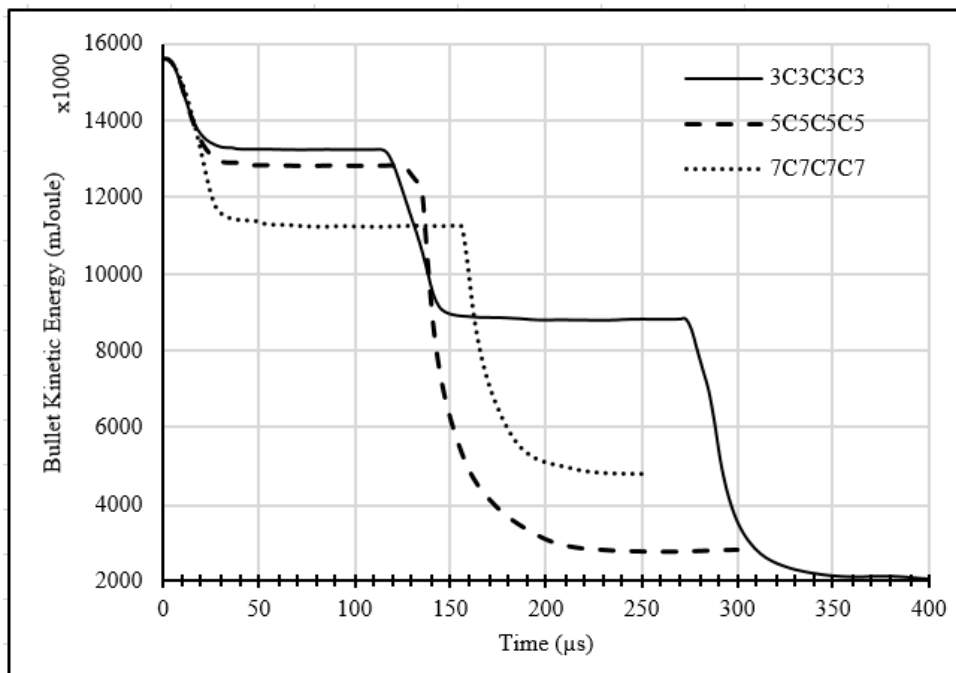
Figure 75 Effect of Interlayer Spacing and Obliquity (75 mm Spaced Targets)
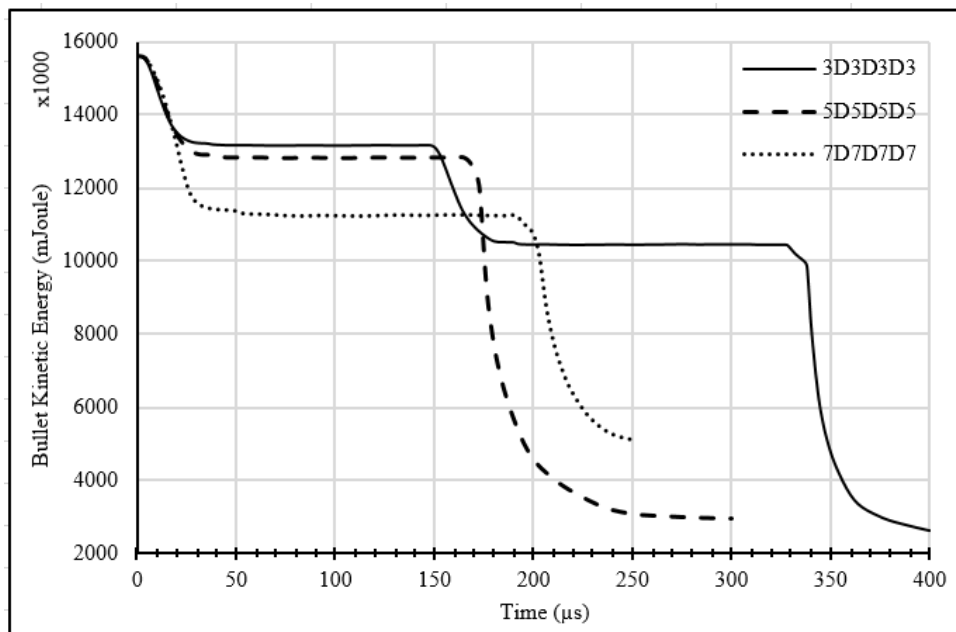
Figure 76 Effect of Interlayer Spacing and Obliquity (100 mm Spaced Targets)

126

Impact cases 3D3D3D3 and 5C5C5C5 are experimentally tested. The tests show that the numerical results and the experiments conducted have a good agreement. However, during the oblique penetration of the targets the projectile is broken into at least two pieces. For example, the broken bullet pieces embed in the third layer of the target 5C5C5C5 as shown in Figure 78. The impact velocities of the shot numbers denoted by #17 and #18 in the Figure 78 are 785 m/s and 789 m/s respectively. The postmortem view of the target 5C5C5C5 is presented in Figure 77.
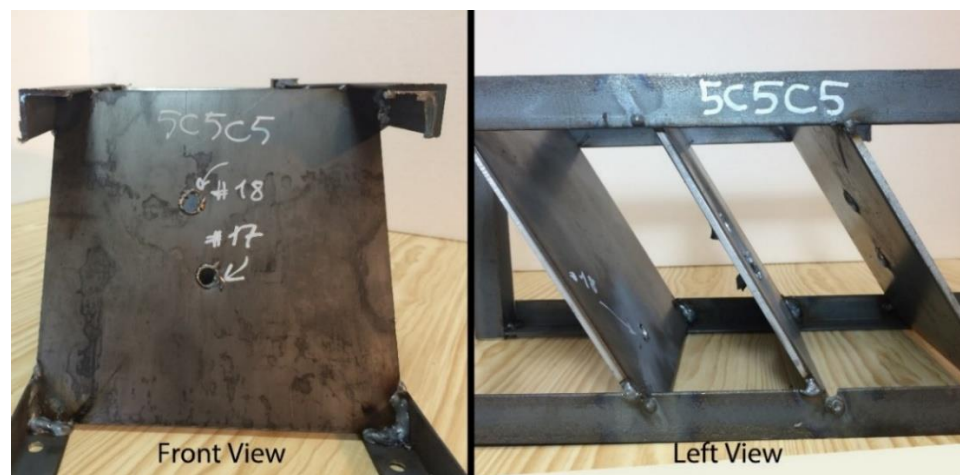
Figure 77 Post-Impact Front and Left View of The Target 5C5C5C5 (Left View: Impact Side Right to Left)

Figure 78 Third Angle View of the Second Layer of the Target 5C5C5C5

The numerical results estimate the second layer of the target will undergo severe deformations with the highly oblique impact of the rigid bullet core but the third layer will remain undefeated. The analytical rigid assumption of the bullet core prevents the failure of the bullet core which underestimates the deformations and the major failure of the bullet, however, the overall plate defeat mechanism shows similar results with the experimental findings. The corresponding numerical result is given in Figure 79. The bullet tumbling increases so considerably that, although it completely pierced the second layer, when it hit to the second layer it loses 98% of its of initial velocity. Figure 79 shows the considerable bullet tumbling (180-degree rotation from its direction of flight is observable) at second plate.
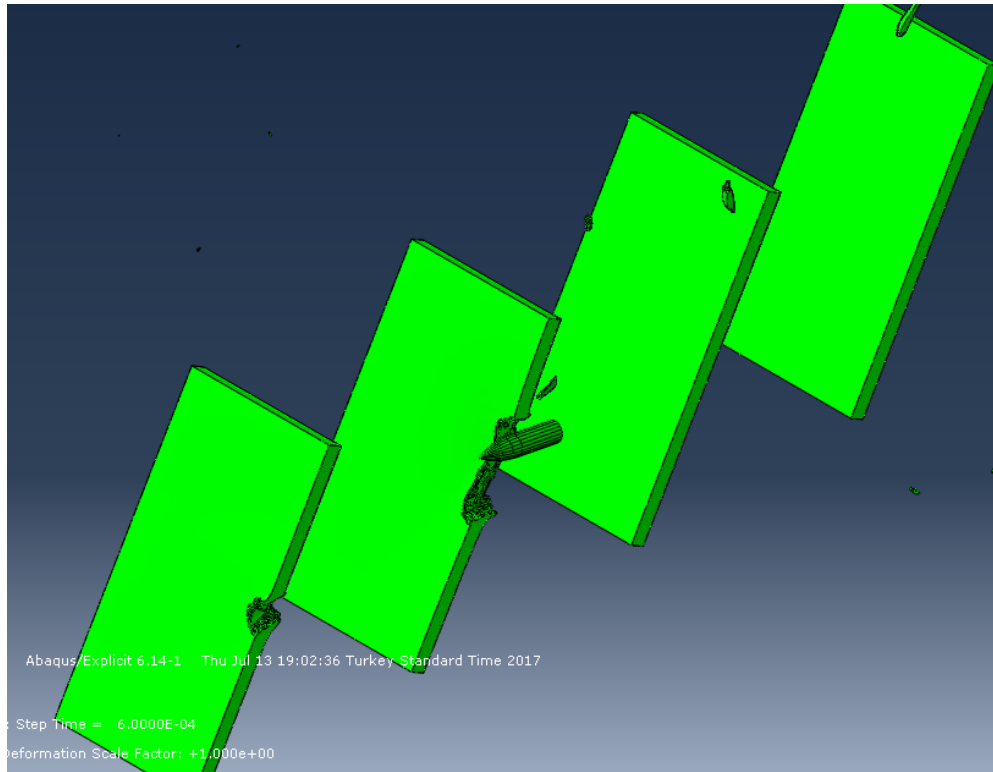
Figure 79 Numerical Result of The Target 5C5C5C5 (Impact Side on the Left Plate)

A similar result is observed for the target 3D3D3D3. The target 3D3D3D3 is shot twice and the bullet velocities are recorded before impact as 797.2 m/s and 790 m/s respectively. The bullet speed and damage to first two targets are predicted well by the numerical results. Although, the numerical results show that the third layer is defeated and severely deformed by the projectile, the experimental results of shot numbers #15 and #16 shows that the damage at the third layer is not to that extent. The deformation in the third layer of the target is presented in Figure 80.
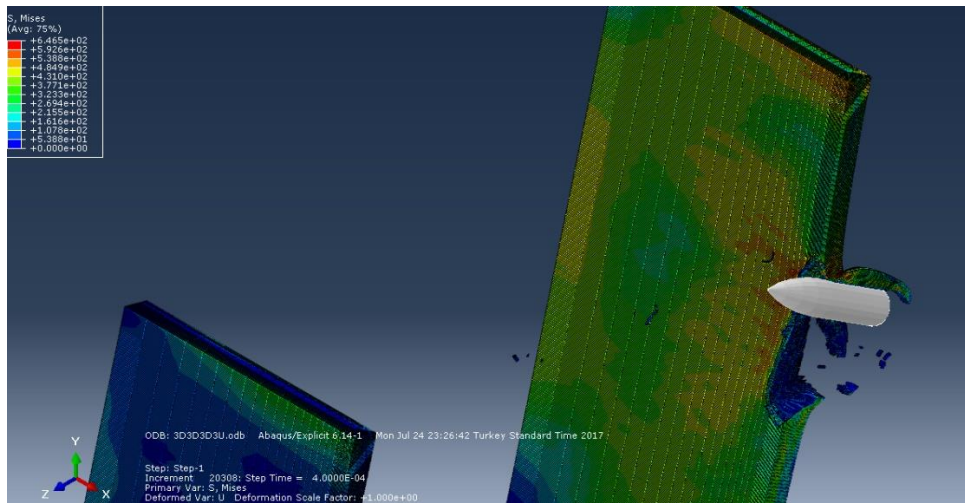
Figure 80 The Damage in The Third Layer of The Target 3D3D3D3

Moreover, the bullet core in shot #15 impacted to the third layer in two pieces. The deformations after impact tests are presented in Figure 81.

Figure 81 The View of The Target 3D3D3D3 (Right to Left: First-Second-Third Layers)

130

Increasing the plate thickness from 5 mm to 10 mm is investigated both numerically and experimentally. In other words, instead of using 4 plates each having 5 mm thickness, this time two plates each having 10 mm thickness are being used. The bullet velocity against the targets 4A4, 4B4, 4C4 and 4D4 are plotted in Figure 82. The numerical results show that both 75 mm and 100 mm spacing of 10 mm thick 15-degree oblique plates provide ballistic protection.
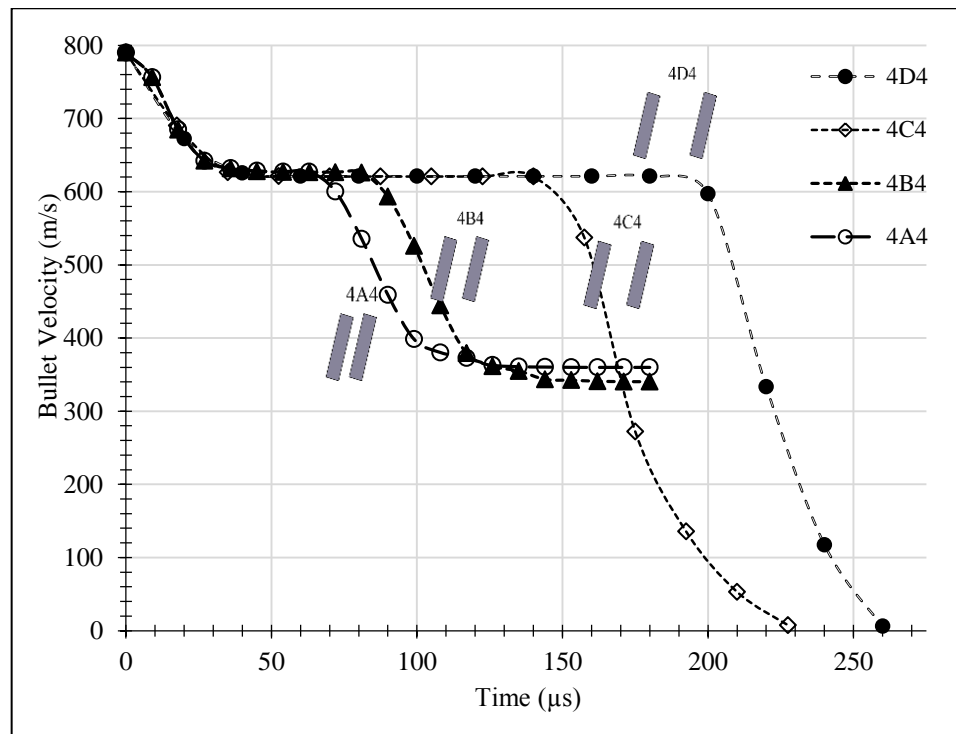
Figure 82 Effect of Spacing of 10 mm Mild Steel Targets with 15 Degree Obliquity

Although the simulations show that the bullet pierce the targets having 50 mm and 30 mm interlayer spacing, the 4B4 target (having 50 mm spacing) is experimentally tried and the bullet core embeds into the second layer as shown in Figure 83. This

finding is contradicting with the numerical analysis in which the bullet exit velocity is found as 340 m/s.

Figure 83 Rear of The Target 4B4 (Back Surface of the Second Layer)

Inspecting Figure 84, one can notice that the bullet entry petal around the hole of the impact side of the target plate shows there is a considerable amount of bullet rotation due to horizontal yaw despite the target is aligned to the shooting direction properly at 15-degree obliquity. The discrepancy between the numerical and experimental conduct could stem from improper impact of the bullet.
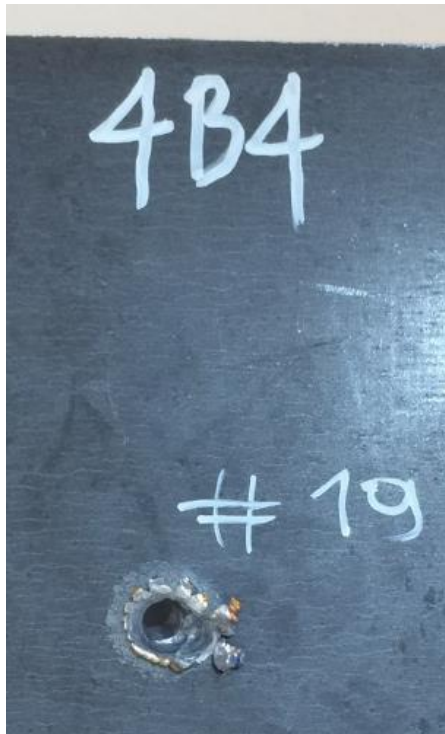
Figure 84 View of The Frontal Petal of the Target 4B4

Tabulation of the numerical results are presented in Table 16. It is clear from the table that increasing the interlayer spacing enhanced the ballistic protection in parallel layered oblique targets.

Table 16 The Tabulated Results of Numerical Analyses of Parallel Layered Targets

Target	Residual Velocity (m/s)	Remark
3-A-3-A-3-A-3	388	Pierces the target
3-B-3-B-3-B-3	192	Pierces three layers
3-C-3-C-3-C-3	80	Pierces three layers
3-D-3-D-3-D-3	71	Pierces three layers
5-A-5-A-5-A-5	270	Ricochets from the fourth layer
5-B-5-B-5-B-5	242	Pierces two layers
5-C-5-C-5-C-5	12	Pierces two layers
5-D-5-D-5-D-5	25	Pierces two layers
7-A-7-A-7-A-7	383	Ricochets from the second layer
7-B-7-B-7-B-7	403	Ricochets from the second layer
7-C-7-C-7-C-7	395	Ricochets from the second layer
7-D-7-D-7-D-7	397	Ricochets from the second layer
4-A-4	360	Pierces the target
4-B-4	340	Pierces the target
4-C-4	0	Embedded in the second layer
4-D-4	0	Embedded in the second layer

5.7.3. Effect of Obliquity in Target Systems (Cassette Structures)

Up to this point the effectiveness of the parallel layering of the targets are discussed. The effectiveness of non-parallel arrangements of target layers, which can also be considered as cassette structure of target, is investigated. The alternative target combinations could be as follows: Increasing the layer obliquity in subsequent layers, decreasing the layer obliquity in subsequent layers or zigzag arrangement of layers with various spacing may worth investigated.

For this sake, 13 target cases are considered and investigated numerically and experimentally. For the constituted targets, corresponding bullet exit velocities numerically predicted and experimental results are tabulated in Table 17.

Table 17 Bullet Exit Velocities of Non-Parallel Layers

Target Configuration	Residual Velocity (m/s)	Remark
1-3-5	553	Pierces the Target
1-3-7	444	Pierces the Target
1-5-7	168	Ricochets from the 3rd Layer
7-5-1	453	Pierces the Target
1-A-3-A-5	533	Pierces the Target
1-A-3-A-7	212	Pierces the Target
1-A-5-A-7	356	Ricochets from the 3rd Layer
3R-1-3	576	Pierces the Target
3R-A-1-A-3	155	Pierces the Target
5-1-5R	544	Pierces the Target
5R-A-1-A-5	0	Embeds in the 3rd Layer
7R-1-7	458	Pierces the Target
7R-A-1-A-7	121	Ricochets from the 3rd Layer Good agreement with the experiment

Figure 85 shows the bullet velocity drop for the considered cases. As one can see clearly from the figure, 1-5-7 configuration gives superior ballistic protection compared to the other targets. However, changing the orientations of target plates reverse, constituting the case 7-5-1, the target dramatically loses its ballistic resistance. Moreover, increasing the interlayer spacing contributes the ballistic resistance of targets 1-3-5 and 1-3-7 but it shows an opposite fashion for target 1-5-7. Considering the targets 1-3-5 and 1A3A5, there is a slight decrease in the bullet exit velocity when the spacing is increased to 30 mm. Nonetheless, when the targets

1-3-5 and 1A3A5 are compared, increasing the interlayer distance does not contribute to protection effectiveness of the target clearly.
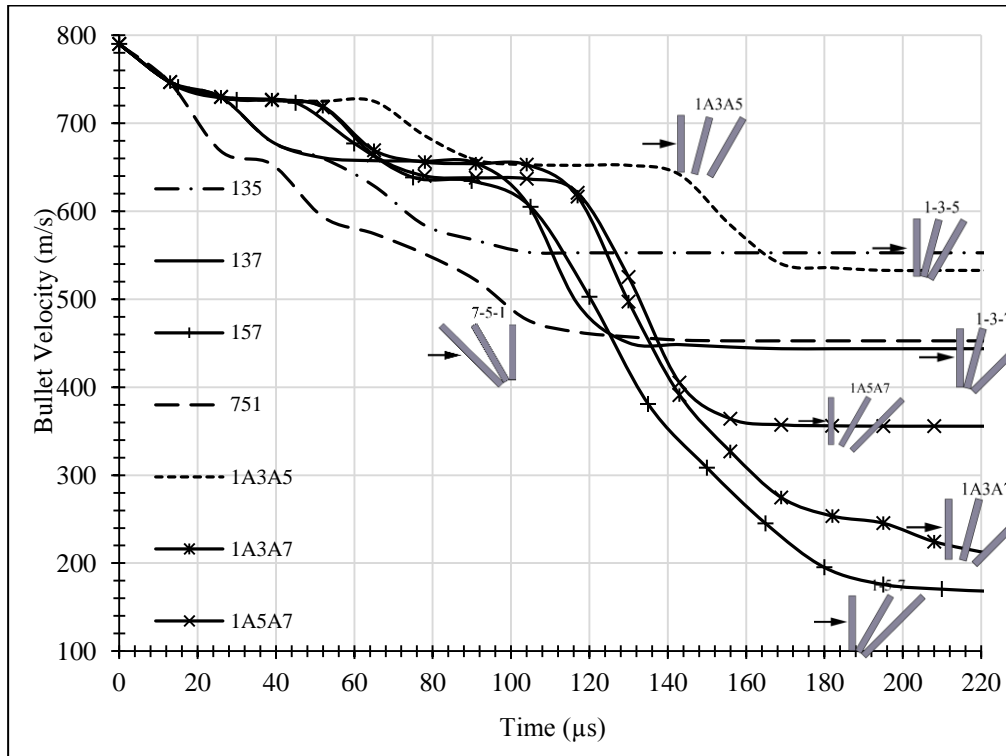
Figure 85 Comparison of Target Effectiveness by Considering the Bullet Exit Velocities of Non-Parallel Targets

As a last remark, configurations 1-5-7 and 1A5A7 give the total protection of the bullet by ricocheting.

The angle of obliquity does not affect the bullet exit velocity much, as presented in Figure 86. However, the spacing of zigzag layers can cause a bullet velocity drop drastically. Zigzag arrangements of targets are found very sensitive to 30 mm spacing. If the bullet exit velocities are compared for the targets 3R-1-3, 5R-1-5 and 7R-1-7 and their spaced configurations, 3R-A-1-A-3, 5R-A-1-A-5, 7R-A-1-A-7 the sensitivity of spacing can be clearly observed. The target 5R-A-1-A-5 is found

superior ballistic resistance against the armor piercing bullet comparing the other cases.
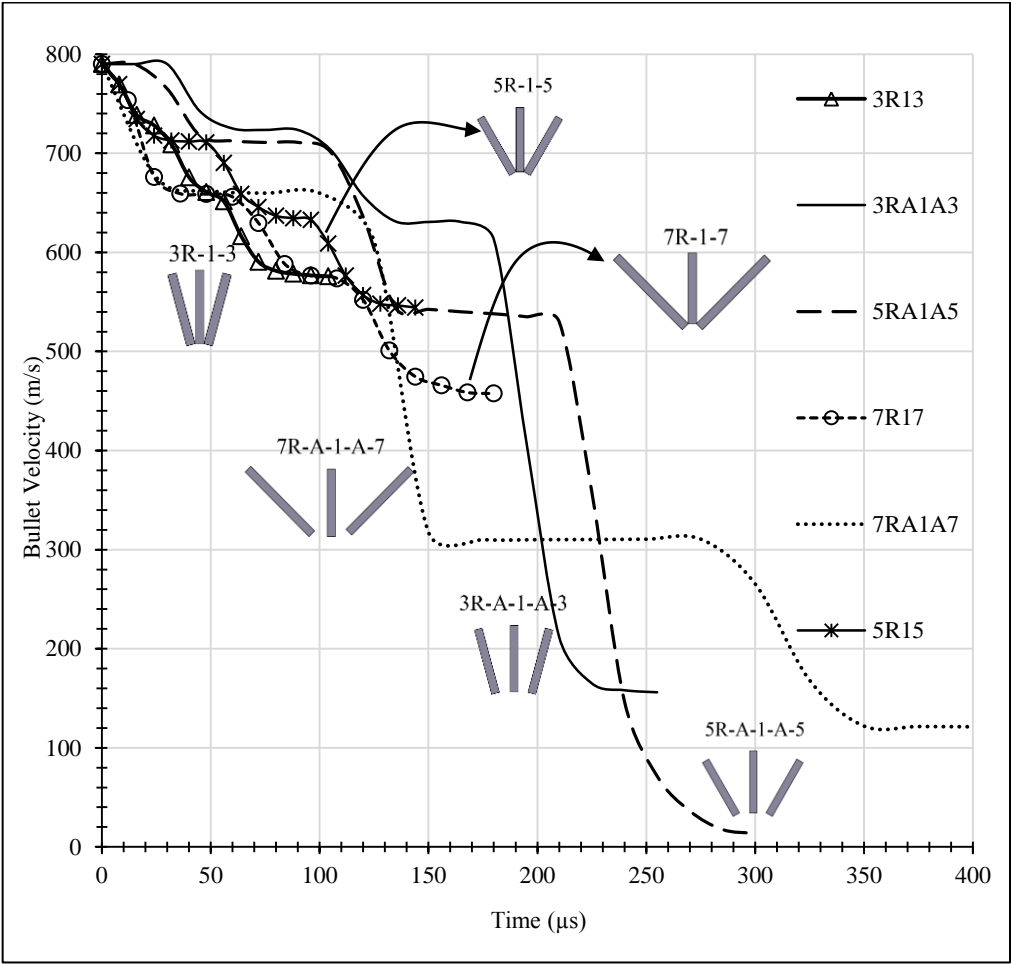
Figure 86 Projectile Velocity Drop Against Zigzag Arrangement Targets

The bullet core ricochets from the third layer of the target 7R-A-1-A-7 which is presented in Figure 87 and this result is experimentally verified as seen in Figure 88.
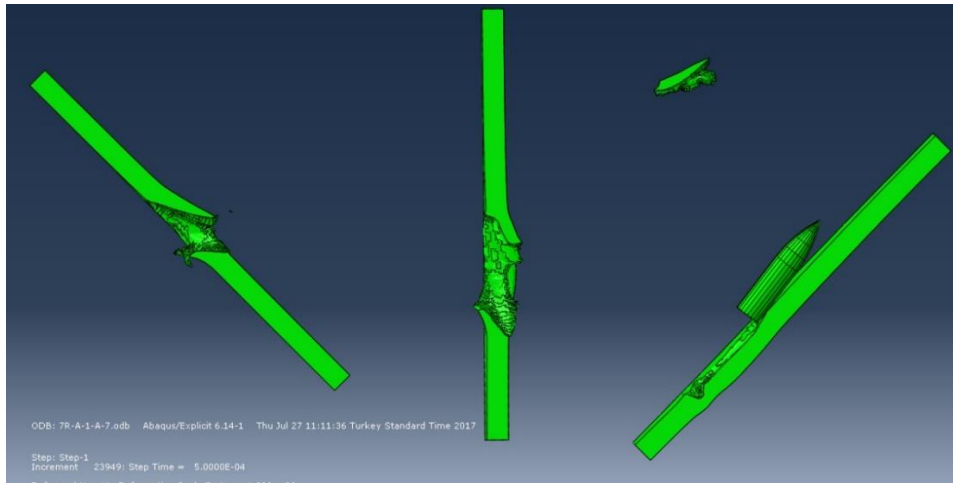
Figure 87 The Numerical Result of 7R-A-1-A-7

The target 7R-A-1-A-7 is impacted with the shots #20 and #21 and the projectile ricochets from the third layer of target causing a negligible deformation on it. The bullet initial velocities for these shots are measured as 788.3m/s and 799.4m/s respectively.
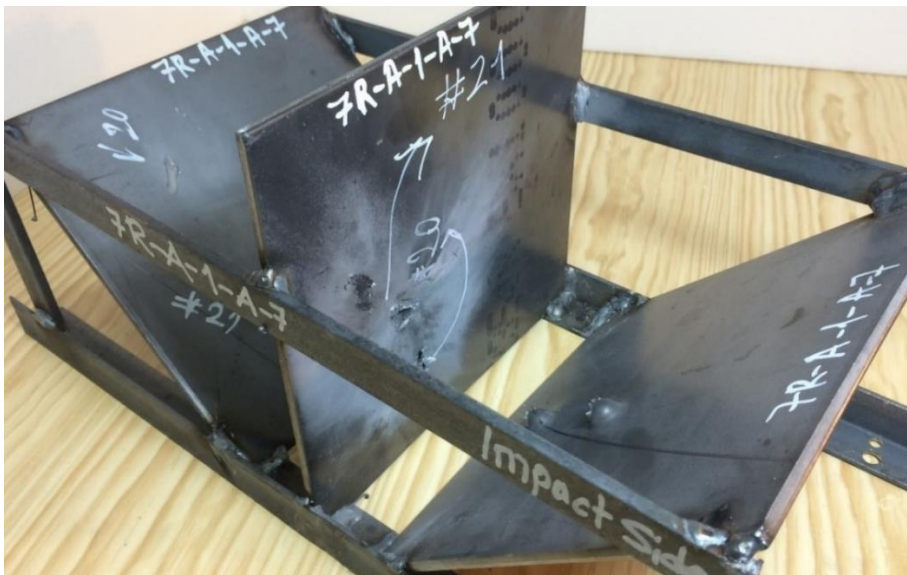
Figure 88 Impacted Target 7R-A-1-A-7

CHAPTER 6

DISCUSSIONS AND CONCLUSIONS

6.1. Discussions

In this work, the ballistic behavior of monolithic, layered, layered with spacing, layered-spaced and oblique targets is investigated numerically and experimentally. Since the experimental work is costly and time consuming, only some selected target arrangements are tested experimentally. The selected impact cases show great consistency with the numerical results. The constructed numerical model can be extended to further impact cases.

Considering the normal impact cases, the highest target resistance is obtained by the monolithic target compared to layered targets. The 20 mm thick monolithic mild steel target reduced the initial velocity of the projectile to 363m/s. The velocity drop of the projectile is 54%. Layering of the monolithic target by 4 x 5 mm and 2 x 10 mm layers clearly impairs the target by keeping the total thickness (total areal density) the same. Bullet exit velocities against 2 x 10 mm configuration (2-2) and 4 x 5 mm configuration (1-1-1-1) are calculated as 373 m/s and 375 m/s respectively. Decreasing the individual areal density of the layers by half weakens the whole 20 mm thick target by 2.7%. If the thickness of the target layer is reduced to one-fourth, then the target weakens by 3.6% compared to monolithic target when the bullet exit velocities are considered. Leaving gaps between the target layers dramatically impairs the target resistance. The target resistance drops by 30% against the AP bullet having 790 m/s initial velocity. The amount of the gap does not affect the penetration of the bullet.

If the target is composed of different thickness in-contact plates, as in the case of 2-1-1 and 1-1-2 configurations, choosing the thicker plate (10 mm in our investigation) as frontal position would yield better ballistic performance.

The numerical results and the corresponding experimental results show that, Johnson-Cook damage model well predicts the failure of the target material. However, highly oblique targets also cause the projectile fracture due to high bending stress. This causes the numerical results to deviate from experiments.

Two layers of 5 mm thick 45-degree oblique plates provide protection from 7.62 mm AP projectile. The bullet ricochets from the second layer in 45-degree oblique layered targets.

The lowest projectile exit kinetic energy is calculated for the target arrangement 3C3C3C3 among the other parallel layered targets.

Although some of the parallel layering configurations using 5 mm thick layers provide protection by ricocheting the projectile, none of the configurations is able to stop the projectile completely. The target 4B4 is found strong enough to stop the projectile. The numerical result of the 4B4 arrangement and the experimental result do not match well. The reason of this difference may be caused from poor alignment of the target with respect to the gun position, yawing/oblique impact of the projectile or inhomogeneous deformations of the jacket and filler lead.

In cassette target structures, the penetration behavior of the projectile is found very sensitive to second plate position and the oblique angle of the layer. The interlayer distance is not a major factor for small degrees of obliquity in cassette structures if the velocity drop of the projectile is considered. However, this fashion shifts to opposite in highly oblique impacts. The targets 1-3-5, 1-3-7, 3R-1-3, 5-1-5R and 7R-1-7 and their spaced configurations are good examples on this phenomenon.

A summary table for comparison of the targets with respect to their areal densities is presented in Table 18.

Table 18 An Overview of The Investigated Cases for Areal Densities

Target	Total Areal Density Until Ricochet kg/m^2	Remark
20 mm Monolithic	157	Pierces the Target
27 mm	212	Ballistic Limit Thickness
3A3A3A3	163	Pierces the Target (FAIL)
3B3B3B3	163	Pierces 3 layers
3C3C3C3	163	Pierces 3 layers
3D3D3D3	163	Pierces 3 layers
5A5A5A5	181	Ricochets from fourth layer
5B5B5B5	136	Pierces 2 layers
5C5C5C5	136	Pierces 2 layers
5D5D5D5	136	Pierces 2 layers
7A7A7A7	111	Ricochets from second layer
7B7B7B7	111	Ricochets from second layer
7C7C7C7	111	Ricochets from second layer
7D7D7D7	111	Ricochets from second layer
4A4	181	Pierces the target (FAIL)
4B4	181	Pierces the target (FAIL)
4C4	181	Embeds in the second layer
4D4	181	Embeds in the second layer
135	125	Pierces the Target (FAIL)
137	135	Pierces the Target
157	140	Ricochets from the 3rd Layer
751	140	Pierces the Target (FAIL)
1A3A5	125	Pierces the Target (FAIL)
1A3A7	135	Pierces the Target (FAIL)
1A5A7	140	Ricochet from the 3rd Layer
3R13	121	Pierces the Target (FAIL)
3RA1A3	121	Pierces the Target (FAIL)
5R15	130	Pierces the Target (FAIL)
5RA1A5	130	Embeds in the 3rd Layer
7R17	150	Pierces the Target (FAIL)
7RA1A7	150	Ricochets from the 3rd Layer

6.2. Conclusions

- 5 mm thick target is found enough to strip off the lead and brass jacket covering the bullet core. However, the jacket and the lead may affect the bullet exit velocity and as well as the orientation depending on the obliquity.

- For thinner targets, the jacket and the lead may cause a deviation in numerical result from the experimental studies. The inertial effects of the jacket and the lead are neglected but thin targets can be affected by the inertial effects of these parts. Furthermore, perforation energy may be lower than the energy required to strip of the jacket. For such cases using a full bullet model including jacket and the lead may yield accurate results.

- The bullet impact holes inspected and noticed that the bullet motion had considerable horizontal and vertical yaw. This yawing impact can be detected by inspecting the hole entry petals inhomogeneity on the target plates. Increasing the distance between the target and the gun may yield more accurate results.

- The tumbling motion and the flight path of the bullet core in the interlayer space is not predicted well. The reason of prediction of the projectile trajectory in the interlayer spaces could be the inhomogeneous deformations of jacket and lead at the early stages of the impact to the front plate. This inhomogeneity may have created rotation of the bullet core at hole entry and it may have contributed the bullet tumbling motion in other planes then may turned out the results seem to be pathological in some cases.

- Material properties of mild steel target is directly taken from literature. The dynamic material properties along with the damage initiation and the damage evolution properties of the used plates ideally should be tested and implemented to the numerical model. The results should be updated accordingly.

- The nose shape profile, center of mass and the moment of inertia of the bullet core might be slightly be different than the real case, but these effects are assumed to be small and neglected in simulations. However, the exact nose shape of the bullet core may also play a role on consistency of the numerical results with experimental outcomes.

- The target material anisotropy is not taken into account. Normalization tempering of the target materials before the experiments can improve the accuracy of the numerical predictions. However, the failure parameters of the material should be updated after the normalization.

- The bullet core is assumed to be rigid in this work. However, in the tests, in some cases the projectile breaks into pieces. In such cases, while some half of the bullet core embedded in a layer, the other half pierced that layer and embedded in or ricocheted from the next layer. Utilizing a proper failure criterion for the bullet core can yield to more realistic solutions.

- Up to 15 degrees of obliquity thinner targets (thickness ≤ 5 mm) seems to weaken the target compared to normal impact cases in present investigation. This phenomenon needs to be verified with the further experimental and numerical investigations.

- The numerical simulations showed that the position and the angle of obliquity may greatly affect the protection limit of the layered targets. The maximum protection is assured if the projectile hits a target with its bearing surface. Since the angular velocity due to tumbling has a great effect on the bullet rotation. Together with the interlayer spacing it may result in an impact by the bearing surface of the bullet. Thus, the angle of obliquity and the position of the second layer is very critical when the maximum is considered. This may be called as second plate effect in ballistics.

- In order to exploit the second plate effect as much as possible, the direction of the angle of obliquity of the second layer should be opposite to the bullet rotation after exiting the first layer.
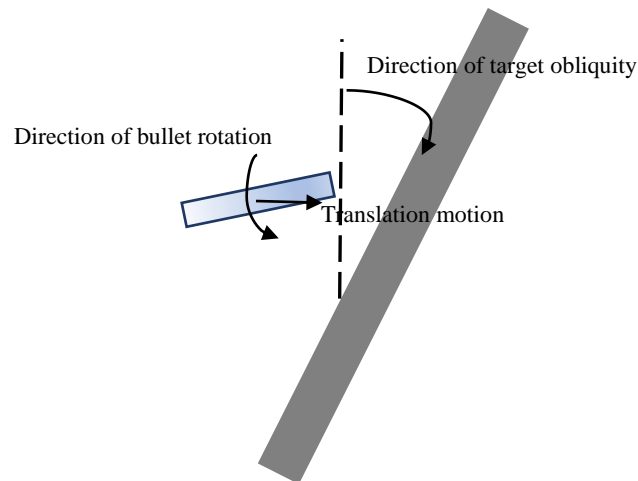
Figure 89 Bullet Rotation vs Target Obliquity

- The ballistic limit thickness is found as 27 mm for the 7.62 mm AP projectile. This thickness may also be called as protection limit thickness for a Level 3 threat. This protection limit can be reduced to 10 mm by single or double layer oblique plates.
- Considering the areal density of the armor structure, using proper layering and spacing configuration together, the total weight of the target can be reduced to 64%.

6.3. Future Works

- Changing the target material types with the high-low strength couple the effectiveness of the target could also be improved.

- Using some filler materials such as rubber, silica, granular materials, sand etc. between the plates could be a potential research project.

- The target plates were stress-free at initial conditions and they were assigned pinned support boundary conditions from surrounding surfaces in this study. Impacting of the prestressed targets and the effect of pre-stressing on the ballistic behavior of the targets could attract the potential interest.

- The target resistance at small degrees of obliquity should be investigated in a separate work.

REFERENCES

[1]   M. Park, J. Yoo, and D. T. Chung, "An optimization of a multi-layered plate under ballistic impact," *Int. J. Solids Struct.*, vol. 42, no. 1, pp. 123–137, 2005.

[2]   M. Übeyli, R. O. Yildirim, and B. Ögel, "On the comparison of the ballistic performance of steel and laminated composite armors," *Mater. Des.*, vol. 28, no. 4, pp. 1257–1262, 2007.

[3]   W. Goldsmith, "Non-ideal projectile impact on targets," *Int. J. Impact Eng.*, vol. 22, no. 2, pp. 95–395, 1999.

[4]   R. . Wharton, S. . Formby, and R. Merrifield, "Airblast TNT equivalence for a range of commercial blasting explosives," *J. Hazard. Mater.*, vol. 79, no. 1–2, pp. 31–39, Dec. 2000.

[5]   M. A. Meyers, *Dynamic Behavior of Materials*. 1994.

[6]   NATO, "Procedures for Evaluating the Protection Level of Armoured Vehicles Volume 1: Kinetic Energy and Artillery Threat AEP-55," *Allied Eng. Publ.*, vol. 1, no. AUGUST, 2011.

[7]   NATO, "V50 Ballistic Test for Armor," no. 18 December 1997, pp. 1–17, 1997.

[8]   S. Y. Aly and Q. M. Li, "Critical impact energy for the perforation of metallic plates," *Nucl. Eng. Des.*, vol. 238, no. 10, pp. 2521–2528, 2008.

[9]   National Institute of Justice, "Ballistic Resistant Protective Materials-NIJ Standard 0108.01," *Ballsitic Resist. Prot. Mater.*, pp. 1–16, 1985.

[10]   U.S. Department of Justice, "Ballistic Resistance of Body Armor," *NIJ Stand.*, no. August, 2008.

[11] US, "MIL-A-12560H," 1984.

[12] NATO, "Procedures For Evaluating the Protection Level of Armoured Vehicles-AEP55," *Allied Eng. Publ. 55*, vol. 2, no. AUGUST, 2011.

[13] NATO, "Protection levels for occupants of logistic and light armoured vehicles," *NATO Stand. STANAG 4569*, no. January, pp. 1–8, 2004.

[14] N. K. Gupta, M. A. Iqbal, and G. S. Sekhon, "Experimental and numerical studies on the behavior of thin aluminum plates subjected to impact by blunt- and hemispherical-nosed projectiles," *Int. J. Impact Eng.*, vol. 32, no. 12, pp. 1921–1944, 2006.

[15] T. Jankowiak, A. Rusinek, and P. Wood, "A numerical analysis of the dynamic behaviour of sheet steel perforated by a conical projectile under ballistic conditions," *Finite Elem. Anal. Des.*, vol. 65, pp. 39–49, 2013.

[16] K. M. Kpenyigba, T. Jankowiak, A. Rusinek, and R. Pesci, "Influence of projectile shape on dynamic behavior of steel sheet subjected to impact and perforation," *Thin-Walled Struct.*, vol. 65, pp. 93–104, 2013.

[17] Z. Rosenberg and E. Dekel, "A numerical study of the cavity expansion process and its application to long-rod penetration mechanics," *Int. J. Impact Eng.*, vol. 35, no. 3, pp. 147–154, 2008.

[18] Z. Rosenberg and E. Dekel, "A computational study of the influence of projectile strength on the performance of long-rod penetrators," *Int. J. Impact Eng.*, vol. 18, no. 6, pp. 671–677, Sep. 1996.

[19] Y. H. Yoo and M. Lee, "Protection effectiveness of an oblique plate against a long rod," *Int. J. Impact Eng.*, vol. 33, no. 1–12, pp. 872–879, 2006.

[20] Z. Rosenberg, Y. Ashuach, Y. Yeshurun, and E. Dekel, "On the main mechanisms for defeating AP projectiles, long rods and shaped charge jets," *Int. J. Impact Eng.*, vol. 36, no. 4, pp. 588–596, Apr. 2009.

[21] "7.62x54 rifle cartridge." [Online]. Available: http://gunrf.ru/rg_patron_7_62x54_eng.html. [Accessed: 10-May-2017].

[22] D. Cardoso and F. Teixeira-Dias, "Modelling the formation of explosively formed projectiles (EFP)," *Int. J. Impact Eng.*, vol. 93, pp. 116–127, 2016.

[23] "EFP Illustrated." [Online]. Available: https://laststandonzombieisland.com/tag/i-efp/. [Accessed: 20-Aug-2017].

[24] Q.-L. Yan *et al.*, "Thermobaric effects formed by aluminum foils enveloping cylindrical charges," *Combust. Flame*, vol. 166, pp. 148–157, 2016.

[25] A. C. Jacinto, R. D. Ambrosini, and R. F. Danesi, "Experimental and computational analysis of plates under air blast loading," *Int. J. Impact Eng.*, vol. 25, no. 10, pp. 927–947, Nov. 2001.

[26] G. S. Langdon, I. B. Rossiter, V. H. Balden, and G. N. Nurick, "Performance of mild steel perforated plates as a blast wave mitigation technique: Experimental and numerical investigation," *Int. J. Impact Eng.*, vol. 37, no. 10, pp. 1021–1036, Oct. 2010.

[27] H. N. G. Wadley *et al.*, "An active concept for limiting injuries caused by air blasts," *Int. J. Impact Eng.*, vol. 37, no. 3, pp. 317–323, 2010.

[28] N. Kılıç, S. Bedir, A. Erdik, B. Ekici, A. Taşdemirci, and M. Güden, "Ballistic behavior of high hardness perforated armor plates against 7.62 mm armor piercing projectile," *Mater. Des.*, vol. 63, pp. 427–438, 2014.

[29] R. F. Bishop, R. Hill, and N. F. Mott, "The theory of indentation and hardness tests," *Proc. Phys. Soc.*, vol. 57, no. 3, 1945.

[30] T. W. Ipson and R. F. Recht, "Ballistic perforation dynamics," *J. Appl. Mech.*, vol. 30, no. 3, pp. 384–390, 1963.

[31] T. W. Ipson and R. F. Recht, "Ballistic-penetration resistance and its measurement," *Exp. Mech.*, vol. 15, no. 7, pp. 249–257, 1975.

[32] B. Babaei, M. M. Shokrieh, and K. Daneshjou, "The ballistic resistance of multi-layered targets impacted by rigid projectiles," *Mater. Sci. Eng. A*, vol. 530, pp. 208–217, 2011.

[33] G. R. Johnson and W. H. Cook, "A constitutive model and data for metals subjected to large strains, high strain rates and high temperatures," *Proceedings of the 7th International Symposium on Ballistics*, vol. 547. pp. 541–547, 1983.

[34] T. Børvik, O. S. Hopperstad, T. Berstad, and M. Langseth, "A computational model of viscoplasticity and ductile damage for impact and penetration," *Eur. J. Mech. A/Solids*, vol. 20, no. 5, pp. 685–712, 2001.

[35] F. J. Zerilli and R. W. Armstrong, "Dislocation mechanics based analysis of material dynamics behavior: Enhanced ductility, deformation twinning, shock deformation, shear instability, dynamic recovery," *J. Phys. IV JP*, vol. 7, no. 3, 1997.

[36] R. W. Armstrong and F. J. Zerilli, "Dislocation Mechanics Based Analysis of Material Dynamics Behavior," *Le J. Phys. Colloq.*, vol. 49, pp. C3-529–534, 1988.

[37] T. L. Warren, "The effect of target inertia on the penetration of aluminum targets by rigid ogive-nosed long rods," *Int. J. Impact Eng.*, vol. 91, pp. 6–13, May 2016.

[38] H. Ebrahimi, R. Ghosh, E. Mahdi, H. Nayeb-Hashemi, and A. Vaziri, "Honeycomb sandwich panels subjected to combined shock and projectile impact," *Int. J. Impact Eng.*, vol. 95, pp. 1–11, 2016.

[39] X. Jia, Z. Huang, X. Zu, X. Gu, C. Zhu, and Z. Zhang, "Experimental study on the performance of woven fabric rubber composite armor subjected to shaped charge jet impact," *Int. J. Impact Eng.*, vol. 57, pp. 134–144, Jul. 2013.

[40] T. Børvik, O. S. Hopperstad, M. Langseth, and K. A. Malo, "Effect of target thickness in blunt projectile penetration of Weldox 460 E steel plates," *Int. J. Impact Eng.*, vol. 28, no. 4, pp. 413–464, Apr. 2003.

[41] X. Teng, S. Dey, T. Børvik, and T. Wierzbicki, "Protection performance of double-layered metal shields against projectile impact," *J. Mech. Mater. Struct.*, vol. 2, no. 7, pp. 1309–1330, 2007.

[42] M. A. Iqbal, A. Diwakar, A. Rajput, and N. K. Gupta, "Influence of projectile shape and incidence angle on the ballistic limit and failure mechanism of thick steel plates," *Theor. Appl. Fract. Mech.*, vol. 62, no. 1, pp. 40–53, 2012.

[43] T. Børvik, O. S. Hopperstad, T. Berstad, and M. Langseth, "Perforation of 12 mm thick steel plates by 20 mm diameter projectiles with flat, hemispherical and conical noses Part I : experimental study," *Int. J. Impact Eng.*, vol. 27, pp. 37–64, 2002.

[44] M. A. Iqbal, G. Gupta, A. Diwakar, and N. K. Gupta, "Effect of projectile nose shape on the ballistic resistance of ductile targets," *Eur. J. Mech. A/Solids*, vol. 29, no. 4, pp. 683–694, 2010.

[45] M. A. Iqbal, S. H. Khan, R. Ansari, and N. K. Gupta, "Experimental and numerical studies of double-nosed projectile impact on aluminum plates," *Int. J. Impact Eng.*, vol. 54, pp. 232–245, Apr. 2013.

[46] T. Børvik, O. S. Hopperstad, T. Berstad, and M. Langseth, "Numerical simulation of plgging failure in ballistic penetration," *Int. J. Solids Struct.*, vol. 38, no. 34–35, pp. 6241–6264, 2001.

[47] R. L. Woodward and S. J. Cimpoeru, "A study of the perforation of aluminium laminate targets," *Int. J. Impact Eng.*, vol. 21, no. 3, pp. 117–131, 1998.

[48] G. Wijk, M. Hartmann, and A. Tyrberg, "A model for rigid projectile

penetration and perforation of hard steel and metallic targets," 2005.

[49]   T. Demir, M. Übeyli, and R. O. Yildirim, "Investigation on the ballistic impact behavior of various alloys against 7.62 mm armor piercing projectile," *Mater. Des.*, vol. 29, no. 10, pp. 2009–2016, 2008.

[50]   M. Übeyli, T. Demir, H. Deniz, R. O. Yildirim, and Ö. Keleş, "Investigation on the ballistic performance of a dual phase steel against 7.62 mm AP projectile," *Mater. Sci. Eng. A*, vol. 527, no. 7–8, pp. 2036–2044, 2010.

[51]   S. N. Dikshit, V. V. Kutumbarao, and G. Sundararajan, "The influence of plate hardness on the ballistic penetration of thick steel plates," *Int. J. Impact Eng.*, vol. 16, no. 2, pp. 293–320, 1995.

[52]   M. A. Iqbal, A. Chakrabarti, S. Beniwal, and N. K. Gupta, "3D numerical simulations of sharp nosed projectile impact on ductile targets," *Int. J. Impact Eng.*, vol. 37, no. 2, pp. 185–195, 2010.

[53]   S. Dey, T. Børvik, O. S. Hopperstad, J. R. Leinum, and M. Langseth, "The effect of target strength on the perforation of steel plates using three different projectile nose shapes," *Int. J. Impact Eng.*, vol. 30, no. 8–9, pp. 1005–1038, 2004.

[54]   X. Teng, T. Wierzbicki, and M. Huang, "Ballistic resistance of double-layered armor plates," *Int. J. Impact Eng.*, vol. 35, no. 8, pp. 870–884, 2008.

[55]   D. Yunfei, Z. Wei, Y. Yonggang, and W. Gang, "The ballistic performance of metal plates subjected to impact by projectiles of different strength," *Mater. Des.*, vol. 58, pp. 305–315, 2014.

[56]   P. K. Jena, K. Ramanjeneyulu, K. Siva Kumar, and T. Balakrishna Bhat, "Ballistic studies on layered structures," *Mater. Des.*, vol. 30, no. 6, pp. 1922–1929, 2009.

[57]   Y. Deng, W. Zhang, and Z. Cao, "Experimental investigation on the ballistic

resistance of monolithic and multi-layered plates against hemispherical-nosed projectiles impact," *Mater. Des.*, vol. 44, pp. 228–239, 2013.

[58] G. Ben-Dor, A. Dubinsky, and T. Elperin, "Effect of air gaps on the ballistic resistance of ductile shields perforated by nonconical impactors," *Mater. Struct.*, vol. 1, no. 2, pp. 279–299, 2006.

[59] J. A. Zukas and D. R. Scheffler, "Impact effects in multilayered plates," *Int. J. Solids Struct.*, vol. 38, pp. 3321–3328, 2001.

[60] D. W. Zhou and W. J. Stronge, "Ballistic limit for oblique impact of thin sandwich panels and spaced plates," *Int. J. Impact Eng.*, vol. 35, no. 11, pp. 1339–1354, 2008.

[61] J. Radin and W. Goldsmith, "Normal Projectile Penetration and Perforation of Layered Targets," *Int. J. Impact Eng.*, vol. 7, no. 2, pp. 229–259, 1988.

[62] I. Marom and S. R. Bodner, "Projectile perforation of multi-layered beams," *Int. J. Mech. Sci.*, vol. 21, no. 8, pp. 489–504, 1979.

[63] R. S. J. Corran, P. J. Shadbolt, and C. Ruiz, "Impact loading of plates — An experimental investigation," *Int. J. Impact Eng.*, vol. 1, no. 1, pp. 3–22, 1983.

[64] N. K. Gupta and V. Madhu, "An experimental study of normal and oblique impact of hard-core projectile on single and layered plates," *Int. J. Impact Eng.*, vol. 19, no. 5, pp. 395–414, 1997.

[65] A. A. Almohandes, M. S. Abdel-Kader, and A. M. Eleiche, "Experimental investigation of the ballistic resistance of steel-fiberglass reinforced polyester laminated plates," *Compos. Part B Eng.*, vol. 27, no. 5, pp. 447–458, 1996.

[66] P. Elek, S. Jaramaz, and D. Micković, "Modeling of perforation of plates and multi-layered metallic targets," *Int. J. Solids Struct.*, vol. 42, no. 3–4, pp. 1209–1224, 2005.

[67] M. A. Iqbal, G. Gupta, and N. K. Gupta, "3D numerical simulations of

ductile targets subjected to oblique impact by sharp nosed projectiles," *Int. J. Solids Struct.*, vol. 47, no. 2, pp. 224–237, 2010.

[68]   Z. Wei, D. Yunfei, C. Z. Sheng, and W. Gang, "Experimental investigation on the ballistic performance of monolithic and layered metal plates subjected to impact by blunt rigid projectiles," *Int. J. Impact Eng.*, vol. 49, pp. 115–129, 2012.

[69]   A. Durmuş, M. Güden, B. Gülçimen, S. Ülkü, and E. Musa, "Experimental investigations on the ballistic impact performances of cold rolled sheet metals," *Mater. Des.*, vol. 32, no. 3, pp. 1356–1366, 2011.

[70]   N. K. Gupta, M. A. Iqbal, and G. S. Sekhon, "Effect of projectile nose shape, impact velocity and target thickness on the deformation behavior of layered plates," *Int. J. Impact Eng.*, vol. 35, no. 1, pp. 37–60, 2008.

[71]   M. A. Iqbal, N. K. Gupta, and G. S. Sekhon, "Behaviour of thin aluminium plates subjected to impact by ogive-nosed projectiles," *Def. Sci. J.*, vol. 56, no. 5, pp. 841–852, 2006.

[72]   S. Feli, M. E. Aalami Aaleagha, and Z. Ahmadi, "A new analytical model of normal penetration of projectiles into the light-weight ceramic–metal targets," *Int. J. Impact Eng.*, vol. 37, no. 5, pp. 561–567, May 2010.

[73]   G. G. Corbett, S. R. Reid, and W. Johnson, "Impact loading of plates and shells by free-flying projectiles: A review," *Int. J. Impact Eng.*, vol. 18, no. 2, pp. 141–230, Mar. 1996.

[74]   N. K. Gupta, R. Ansari, and S. K. Gupta, "Normal impact of ogive nosed projectiles on thin plates," *Int. J. Impact Eng.*, vol. 25, no. 7, pp. 641–660, 2001.

[75]   J. P. Lambert and G. H. Jonas, "Towards standardization in terminal ballistics testing: Velocity representation," 1976.

[76]   G. Ben-Dor, A. Dubinsky, and T. Elperin, "On the Lambert–Jonas approximation for ballistic impact," *Mech. Res. Commun.*, vol. 29, no. 2, pp. 137–139, 2002.

[77]   J. Awerbuch and S. R. Bodner, "Analysis of the mechanics of perforation of projectiles in metallic plates," *Int. J. Solids Struct.*, vol. 10, no. 6, pp. 671–684, 1974.

[78]   R. L. Woodward and M. E. De Morton, "Penetration of Targets by Flat-Ended Projectiles," *Int. J. Mech. Sci.*, vol. 18, pp. 119–127, 1976.

[79]   R. L. Woodward, "A Structural Model for Thin Plate Perforation by Normal Impact of Blunt Projectiles," *Int. J. Impact Eng.*, vol. 6, no. 2, pp. 129–140, 1987.

[80]   P. Elek, S. Jaramaz, and D. Micković, "Modeling of perforation of plates and multi-layered metallic targets," *Int. J. Solids Struct.*, vol. 42, no. 3–4, pp. 1209–1224, Feb. 2005.

[81]   J. Liss, W. Goldsmith, and J. M. Kelly, "A phenomenological penetration model of plates," *Int. J. Impact Eng.*, vol. 1, no. 4, pp. 321–341, 1983.

[82]   J. Liss and W. Goldsmith, "Plate Perforation Phenomena Due to Normal Impact by Blunt Cylinders," *Int. J. Impact Eng.*, vol. 2, no. 1, pp. 37–64, 1984.

[83]   M. J. Forrestal and V. K. Luk, "Dynamic Spherical Cavity-Expansion in a Compressible Elastic-Plastic Solid," *J. Appl. Mech.*, vol. 55, no. 2, p. 275, 1988.

[84]   X. W. Chen and Q. M. Li, "Perforation of a thick plate by rigid projectiles," *Int. J. Impact Eng.*, vol. 28, no. 7, pp. 743–759, 2003.

[85]   X. W. Chen, X. L. Huang, and G. J. Liang, "Comparative analysis of perforation models of metallic plates by rigid sharp-nosed projectiles," *Int. J.*

Impact Eng., vol. 38, no. 7, pp. 613–621, 2011.

[86] X. W. Chen, Q. M. Li, and Y. Z. Chen, "Perforation of medium thick plate by a sharp projectile," *Int. J. Impact Eng.*, vol. 28, pp. 743–759, 2003.

[87] X. W. Chen, X. Q. Zhou, and X. L. Li, "On perforation of ductile metallic plates by blunt rigid projectile," *Eur. J. Mech. A/Solids*, vol. 28, no. 2, pp. 273–283, 2009.

[88] X. Chen, Q. Li, and S. Fan, "Oblique Perforation of Thick Metallic Plates by Rigid Projectiles," *Acta Mech. Sin.*, vol. 22, no. 4, pp. 367–376, Aug. 2006.

[89] M. J. Forrestal and T. L. Warren, "Perforation equations for conical and ogival nose rigid projectiles into aluminum target plates," *Int. J. Impact Eng.*, vol. 36, no. 2, pp. 220–225, Feb. 2009.

[90] G. H. Liaghat, H. M. Naeini, and S. Felli, "The Mechanics of Normal and Oblique Penetration of Conical Projectiles Into Multilayer Metallic Targets," *Iran. J. Sci. Technol.*, vol. 29, 2005.

[91] C. C. Liang, M. F. Yang, P. W. Wu, and T. L. Teng, "Resistant performance of perforation of multi-layered targets using an estimation procedure with marine application," *Ocean Eng.*, vol. 32, no. 3–4, pp. 441–468, 2005.

[92] V. K. Luk, M. J. Forrestal, and D. E. Amos, "Dynamic Spherical Cavity Expansion of Strain-Hardening Materials," *J. Appl. Mech.*, vol. 58, no. 1, p. 1, 1991.

[93] P. K. Jena, N. Jagtap, K. Siva Kumar, and T. Balakrishna Bhat, "Some experimental studies on angle effect in penetration," *Int. J. Impact Eng.*, vol. 37, no. 5, pp. 489–501, 2010.

[94] K. T. Ramesh, "High Strain Rate and Impact Mechanics," in *Handbook of Experimental Solid Mechanics*, 2008, p. 874.

[95] Vili Panov, "Modelling of Behaviour of Metals at High Strain Rates,"

Cranfield University, 2005.

[96] ASTM Int., "Standard Test Methods for Tension Testing of Metallic Materials," *Astm*, vol. i, no. C, pp. 1–27, 2009.

[97] W. Chen and B. Song, *Split Hopkinson (Kolsky) Bar: Design, Testing and Applications*. 2017.

[98] S. E. Jones, J. a. Drinkard, W. K. Rule, and L. L. Wilson, "An elementary theory for the Taylor impact test," *Int. J. Impact Eng.*, vol. 21, no. 1–2, pp. 1–13, 1998.

[99] J. Nussbaum and N. Faderl, "Evaluation of strength model parameters from Taylor impact tests," *Procedia Eng.*, vol. 10, pp. 3453–3458, 2011.

[100] R. Julien, T. Jankowiak, A. Rusinek, and P. Wood, "Taylor's Test Technique for Dynamic Characterization of Materials: Application to Brass," *SEM Exp. Tech.*, no. 2013, pp. 1–9, 2013.

[101] J. W. House, "Taylor Impact Testing," *Air Force Armament Lab.*, no. September 1989, 1989.

[102] S. N. Dikshit, "Oblique impact study in thin armor plate," *Science (80-.).*, no. 2, pp. 185–195, 1998.

[103] S. Ryan, H. Li, M. Edgerton, D. Gallardy, and S. J. Cimpoeru, "The ballistic performance of an ultra-high hardness armour steel: An experimental investigation," *Int. J. Impact Eng.*, vol. 94, pp. 60–73, 2016.

[104] A. Dorogoy, D. Rittel, and A. Brill, "Experimentation and modeling of inclined ballistic impact in thick polycarbonate plates," *Int. J. Impact Eng.*, vol. 38, no. 10, pp. 804–814, 2011.

[105] T. Børvik, L. Olovsson, S. Dey, and M. Langseth, "Normal and oblique impact of small arms bullets on AA6082-T4 aluminium protective plates," *Int. J. Impact Eng.*, vol. 38, no. 7, pp. 577–589, 2011.

[106] J. A. Zukas, "High Velocity Impact Dynamics." pp. 1–290, 1990.

[107] T. J. Holmquist and G. R. Johnson, "A Computational Constitutive Model for Glass Subjected to Large Strains, High Strain Rates and High Pressures," *J. Appl. Mech.*, vol. 78, no. 5, p. 51003, 2011.

[108] A. A. Lukyanov, "Constitutive behaviour of anisotropic materials under shock loading," *Int. J. Plast.*, vol. 24, no. 1, pp. 140–167, 2008.

[109] G. R. Johnson and W. H. Cook, "Fracture characteristics of three metals subjected to various strains, strain rates, temperatures and pressures," *Eng. Fract. Mech.*, vol. 21, no. 1, pp. 31–48, 1985.

[110] H. Huh, K. Ahn, J. H. Lim, H. W. Kim, and L. J. Park, "Evaluation of dynamic hardening models for BCC, FCC, and HCP metals at a wide range of strain rates," *J. Mater. Process. Technol.*, vol. 214, no. 7, pp. 1326–1340, 2014.

[111] G. H. Majzoobi and F. Rahimi Dehgolan, "Determination of the constants of damage models," *Procedia Eng.*, vol. 10, pp. 764–773, 2011.

[112] X. Teng and T. Wierzbicki, "Evaluation of six fracture models in high velocity perforation," *Eng. Fract. Mech.*, vol. 73, no. 12, pp. 1653–1678, 2006.

[113] X. Teng and T. Wierzbicki, "Numerical study on crack propagation in high velocity perforation," *Comput. Struct.*, vol. 83, no. 12–13, pp. 989–1004, 2005.

[114] M. A. Iqbal, K. Senthil, P. Bhargava, and N. K. Gupta, "The characterization and ballistic evaluation of mild steel," *Int. J. Impact Eng.*, vol. 78, pp. 98–113, 2015.

[115] T. Wierzbicki, Y. Bao, Y. W. Lee, and Y. Bai, "Calibration and evaluation of seven fracture models," *Int. J. Mech. Sci.*, vol. 47, no. 4, pp. 719–743, 2005.

[116] X. Teng and T. Wierzbicki, "Transition of failure modes in round-nosed mass-to-beam impact," *Eur. J. Mech. A/Solids*, vol. 24, no. 5, pp. 857–876, 2005.

[117] D. J. Benson, *Computational methods in Lagrangian and Eulerian hydrocodes*, vol. 99, no. 2–3. 1992.

[118] "Abaqus 2016 Documentation." [Online]. Available: http://50.16.225.63/v2016/. [Accessed: 28-Jul-2017].

[119] T. Børvik, S. Dey, and A. H. Clausen, "Perforation resistance of five different high-strength steel plates subjected to small-arms projectiles," *Int. J. Impact Eng.*, vol. 36, no. 7, pp. 948–964, 2009.

[120] O. Gökgöz, "Investigation of Monolithic and Multi-Layered Plates Against Projectile Impact," 2002.

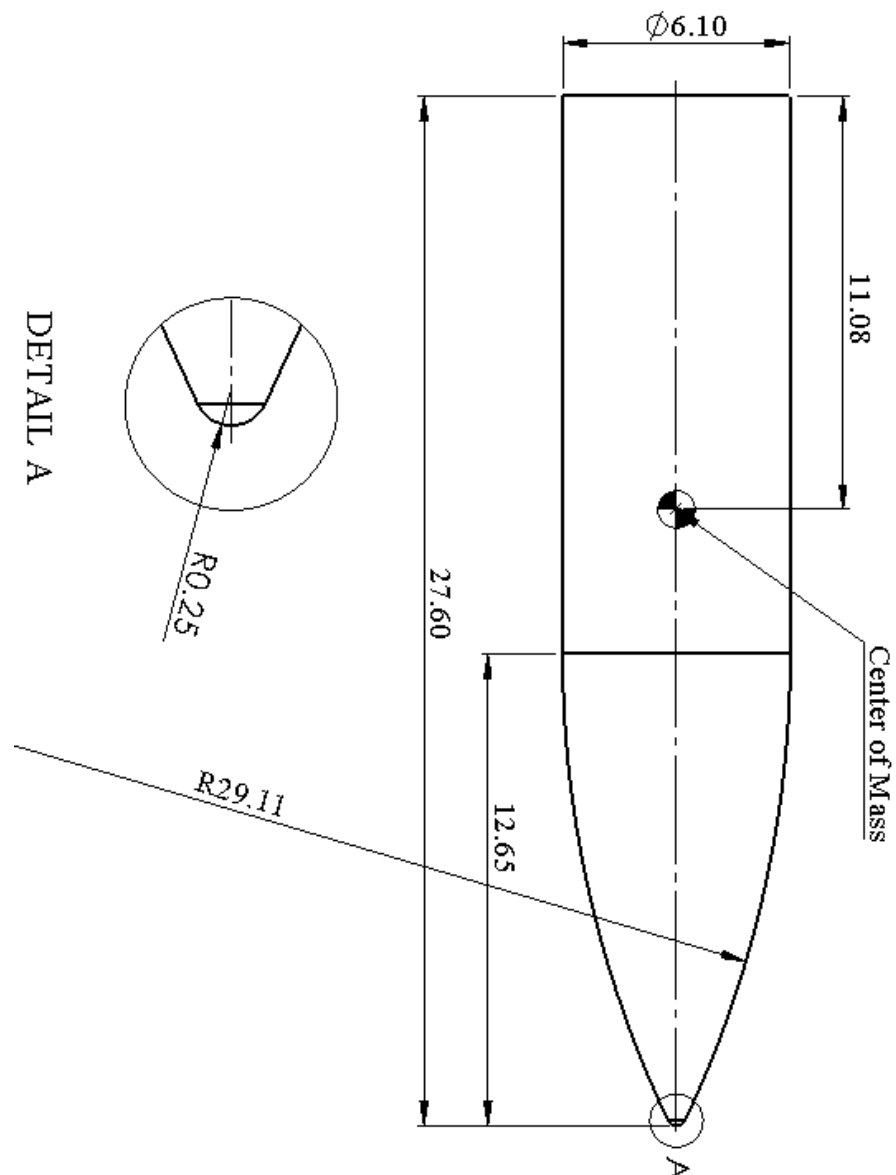**DETAILED DRAWING OF 7.62 mm AP BULLET CORE**

Figure 90 Dimensional Details of a 7.62 mm AP Bullet Core

APPENDIX B

DIFFERENT MESHING STRATEGY

The number of elements in the numerical model significantly affects the computation time. However, it is not the only parameter for computational cost. One another parameter is the smallest element size [118]. In an effort to reduce the computational time, the author of this thesis tried different meshing strategies by decreasing the total number of elements. This thesis is constructed on the meshing strategy (Strategy1) explained in section 5.4.1. Mesh Convergence Study with the Figure 51. A similar meshing strategy (Strategy2) is utilized to have a lower computational cost. The difference between the two meshes are farther distances from the impact zone element sizes are increased to 4 mm, and mesh transition from 0.2 mm to 4 mm is done with tetrahedral elements (C3D10R). The mesh transition is presented in Figure 91.
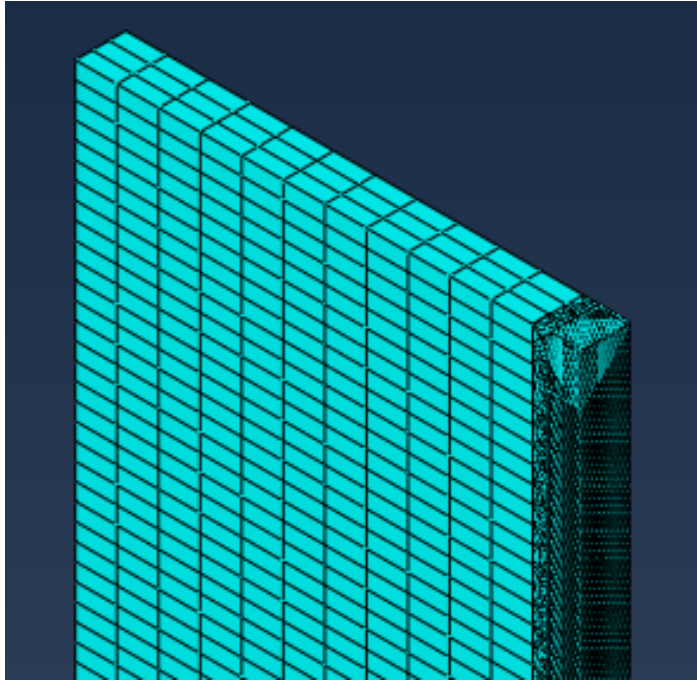
Figure 91 A Different Meshing Strategy

A 5-mm thick plate is impact with two different meshing strategies, and computational details are presented in Table 19.

Table 19 Comparison of Computational Costs of Two Different Meshing Strategy

	Number of Elements		Total No. of Elements	CPU Time [s]	No. of Increments
	C3D8R	C3D10R			
Strategy1	425000	-	425000	210.6	4915
Strategy2	97914	41818	139372	473	17190